580
5/24/84

②

DR-0088-4

DOE/JPL/955688-82/10
(DE84008241)

Energy

SOLAR

DEVELOPMENT OF AN ALL-METAL THICK FILM COST EFFECTIVE METALLIZATION SYSTEM FOR SOLAR CELLS

Final Report for May 1980—January 1983

By
Bernd Ross
Joseph Parker

December 1983

Work Performed Under Contract No. NAS-7-100-955688

Bernd Ross Associates
San Diego, California

Technical Information Center
Office of Scientific and Technical Information
United States Department of Energy

DISCLAIMER

DISCLAIMER

This report was prepared as an account of work sponsored by an agency of the United States Government. Neither the United States Government nor any agency thereof, nor any of their employees, makes any warranty, express or implied, or assumes any legal liability or responsibility for the accuracy, completeness, or usefulness of any information, apparatus, product, or process disclosed, or represents that its use would not infringe privately owned rights. Reference herein to any specific commercial product, process, or service by trade name, trademark, manufacturer, or otherwise does not necessarily constitute or imply its endorsement, recommendation, or favoring by the United States Government or any agency thereof. The views and opinions of authors expressed herein do not necessarily state or reflect those of the United States Government or any agency thereof.

This report has been reproduced directly from the best available copy.

Available from the National Technical Information Service, U. S. Department of Commerce, Springfield, Virginia 22161.

Price: Printed Copy A07
Microfiche A01

Codes are used for pricing all publications. The code is determined by the number of pages in the publication. Information pertaining to the pricing codes can be found in the current issues of the following publications, which are generally available in most libraries: *Energy Research Abstracts (ERA); Government Reports Announcements* and Index (*GRA* and I); *Scientific and Technical Abstract Reports (STAR);* and publication NTIS-PR-360 available from NTIS at the above address.

DOE/JPL/955688-82/10
(DE84008241)
Distribution Category UC-63b

DEVELOPMENT OF AN ALL-METAL THICK FILM COST EFFECTIVE METALLIZATION SYSTEM FOR SOLAR CELLS

BERND ROSS
JOSEPH PARKER

BERND ROSS ASSOCIATES
2154 Blackmore Ct.
San Diego, CA 92109

May 1980 - January 1983

December 1983

FINAL REPORT

Contractual Acknowledgement

The JPL Low-Cost Silicon Solar Array Project is sponsored by the U.S. Department of Energy and forms part of the Solar Photovoltaic Conversion Program to initiate a major effort toward the development of low-cost solar arrays. This work was performed for the Jet Propulsion Laboratory, California Institute of Technology by agreement between NASA and DOE.

TABLE OF CONTENTS

Page

TABLE OF CONTENTS i & ii

LIST OF FIGURES iii, iv, v, vi

LIST OF TABLES vii

1.0 SUMMARY 1

2.0 INTRODUCTION 4

3.0 WORK WITH EARLIER COPPER SYSTEMS 5

3.1 Attempts To Reproduce S071, S079, S080 Pastes 5
3.2 Results of Analysis 7

4.0 SILVER FLUORIDE-CONTAINING COPPER PASTES 11

4.1 Paste and Contact Experiments. 11
4.2 Solar Cell Experiments 18
4.3 Results of Analysis 32

5.0 FLUOROCARBON-CONTAINING COPPER PASTES 40

5.1 Paste, Contact and Analysis 40
5.2 Solar Cell Experiments 47

6.0 CONTACT CONSIDERATIONS 49

6.1 Theory 49
6.2 Experiments 56

7.0 THEORETICAL CONSIDERATIONS OF REACTIONS 60

8.0 HYDROGEN CONCENTRATION PROFILING 75

9.0 FIRING EXPERIMENTS 80

9.1 Furnace Calibration 80
9.2 Gas Ambients 80
9.3 Electrode Firing Experiments 84
9.4 Solar Cell Firing Experiments 89

10.0 COST ANALYSIS 104

11.0 CONCLUSIONS AND PROBLEMS 108

12.0 RECOMMENDATIONS 110

13.0 APPENDICES 111

13.1 Table XI Paste Compositions 111
13.2 Paper presented at the 4th E.C. Photovoltaic Energy Conference, Stresa, Italy 112

14.0 REFERENCES 122

LIST OF ILLUSTRATIONS

Figure	Caption	Page
1	SEM micrograph of an unfired S071A18 print	8
2	SEM micrograph of S071 print fired at 550°C, 850X	8
3	SEM micrograph of S071 print fired at 550°C, 4250X	8
4	Optical micrograph of S079 print fired at 500°C, 200X	9
5	Optical micrograph of S071 print fired at 500°C, 200X	9
6	Optical micrograph of S071 print edge, fired at 500°C, 200X	10
7	Optical micrograph of S071 print center, fired at 500°C, 200X	10
8	Optical micrograph of S071 print fired at at 575°C, 200X	10
9	Photographs of 3 paste electrodes with Scotch tape test above	13
10	SEM micrograph of S032 silver electrode at 1800x	14
11	SEM micrograph of S032 silver electrode at 9000x	14
12	SEM micrograph of F12 copper-silver fluoride, nitrogen fired print at 1800x	16
13	SEM micrograph of F12 copper-silver fluoride, nitrogen fired print at 9000x	16
14	SEM micrograph of F15 flake copper electrode print at 1800x	17
15	SEM micrograph of F15 flake copper electrode print at 9000x	17
16	IV curves of cells with back electrode screened with F-31 copper paste fired in CO at 550°C (after edge grind)	20
17	IV curves of cells with back electrode screened with F-31 copper paste fired in CO at 650°C (after edge grind)	21

Figure	Caption	Page
18	IV curves of cells with back electrode screened with F-32 copper paste fired in carbon monoxide at 600°C (after edge grind)	22
19	IV curves of cells with back electrode screened with F-31 copper paste fired in nitrogen at 550°C	23
20	Fill factor versus amount of Al-Si eutectic a addition to screened back electrode copper paste	24
21	IV curve of control cell with Ti-Pd-Ag front and back	29
22	IV curve of cell with Ti-Pd-Ag front and F-26 copper back	30
23	IV curve of cell with F-39 600°C front and F-26 copper back	31
24	Optical micrograph composite of S080 successful and S079 unsuccessful pastes	33
25	SEM optical micrograph composite of S080 unsuccessful substrate and electrode	36
26	SEM optical micrograph composite of S080 successful substrate and electrode	37
27	X-ray dispersive spectrum of successful S080 electrode	38
28	X-ray dispersive spectrum of successful S080 substrate	39
29	SEM micrograph of F7 copper fluorocarbon electrode at 1800x	41
30	SEM micrograph of F7 copper fluorocarbon electrode at 9000x	41
31	SEM micrograph of F13 copper fluorocarbon electrode at 1800x	46
32	SEM micrograph of F13 copper fluorocarbon electrode at 9000x	46
33	SEM micrograph of substrate under F13 electrode at 1800x	46
34	SEM micrograph of substrate under F13 electrode at 9000x	46

Figure	Caption	Page
35	IV curve of solar cell with F16 copper-fluorocarbon back contact	48
36	Contact tunneling resistance versus depletion width	52
37	Energy level diagram of front contact	54
38	Energy level diagram of back contact	55
39	Photograph of test pattern	59
40	Relation between heat of reaction and activation energy	64
41	Heats of formation versus n for alkane series $C_n H_{2n+2}$	73
42	Hydrogen profiling by resonant nuclear reaction with nitrogen	76
43	Preliminary results of hydrogen profiling	78
44	Tube furnace profile	81
45	Modified firing profile	86
46	F-20 copper electrode sintered at 615°C taken at 2000X	87
47	F-20 copper electrode sintered at 615°C taken at 10,000X	87
48	Edge-on view of F-20 copper electrode sintered at 614°C at 675X magnification	88
49	IV curve of cell with back electrode screened with F-30 copper paste fired at 650°C	90
50	IV curve of cell with back electrode screened with F-20 copper paste fired at 600°C	91
51	IV curve of cell with back electrode screened with F-27 copper paste fired at 600°C	93
52	F-27 silver fluoride-activated copper paste fired at 600°C, with modified two step process A. Magnification 2000X B. Magnification 10,000X	94

Figure	Caption	Page
53	Comparison of copper paste hydrogen and carbon monoxide firing cycles A. F-27, 650°C, hydrogen, Magnification 2000X B. F-30, 584°C, CO fired, Magnification 2600X	95
54	F-30, 584°C, carbon monoxide [CO] fired A. Magnification 1000X B. Edgeview, Magnification 2300X	96
55	F-30, 584°C, Carbon monoxide fired with a diamond scribed scratch at 1000X magnification	98
56	IV curve of cell with back electrode screened with F-19 fired at 615°C	100
57	IV curve of cell with back electrode screened with F-20 copper paste fired at 615°C	101
58	Circuit-Simulated IV Curves	103

LIST OF TABLES

Table	Caption	Page
I	Solar Cell Experiment	19
II	Front Contact Paste Compositions	26
III	Front and Back Contact Solar Cell Experiment (Means, Usually 3 Samples)	28
IV	Composition of Paste F-13	44
V	Two Step Firing Process	45
VI	Selected Heats of Formation	65
VII	Metal Oxidation/Reduction Data	71
VIII	Copper Paste Compositions	89
IX	Copper Pastes F-19 and F-20	99
X	Cost of Material	105
XI	Paste Compositions (Appendix)	111

1.0 SUMMARY

Properties of copper pastes, initially formulated under this contract, did not reproduce earlier results in rheology and metallurgy. Electrodes made with pastes produced under the previous contract were analyzed and raw material characteristics were compared. A needle-like structure was observed on the earlier electroded solar cells, and was identified as eutectic copper-silicon by electron probe Xray spectroscopy. Experiments were conducted with variations in paste parameters, firing conditions, including gas ambients, furnace furniture, silicon surface and others to improve performance characteristics. A liquid medium, intended to provide transport during the carbon fluoride decomposition was incorporated in the paste with promising results, resulting in better adhesion and surviving preliminary environmental tests. 2 x 2 cm solar cells made with fluorocarbon activated copper electrodes and gave 7% AMI efficiency (without AR coating).

Improved adhesion with copper pastes containing silver fluoride, as well as those containing fluorocarbon powder, was obtained. TGA and DTA experiments and analyses pointed to a recommended reduction in the amount of etching component (AgF or fluorocarbon). The introduction of hydrogen at lower temperatures during firing was also helpful in retaining adhesion, although this led to a reduction of the degree of sintering.

Front contact experiments were done with silver fluoride activated pastes on bare silicon, silicon oxide and silicon nitride coated silicon wafers. Adhesion of pastes with AgF on silicon nitride coated wafers was good, but indications were that all cells were shunted and the conclusion was that these systems were unsuitable for front contacts.

Experiments with aluminum back surfaces and screened contacts to that surface were begun. A special low thermal mass quartz boat was designed and constructed. Solar cells were fabricated with screened copper back electrodes with efficiencies up to 11.3%. Low temperature firing tended to result in S shaped IV curves. This was attributed to a barrier formed at the silicon-copper interface. An electrical analogue consisting of a germanium junction binding the cell, gave a similarly S shaped curve.

A cooperative experiment was initiated with W.A. Lanford of S.U.N.Y. Albany on the effect of heat-treatments in various atmospheres on the hydrogen profile of silicon surfaces.

Contact theory was explored to determine the role of various parameters on tunneling and contact resistance. A poster paper was presented at the 4th E.C. Photovoltaic Solar Energy Conference in Stresa, Italy, May 1982. Several solar cell experiments were carried out with the assistance of the Process Research Laboratory of JPL. Data confirm that the presence of eutectic Al-Si additions are beneficial for low contact resistance and fill factors in back contacts. In a further experiment copper pastes with different silver fluoride additions were utilized as front contacts at two temperatures. Data shows various degrees of shunting, making this process/material unlikely for front contacts. Screened fritted and all metal silver showed promise as contacts to aluminum back electrode solar cells.

Finally, an experiment was run with carbon monoxide gas used as the reducing ambient during firing. Excellent adhesion, sintering and good coppery appearance were obtained.

2.0 INTRODUCTION

The purpose of this study is to provide economical, improved thick film solar cell contacts for the high-volume production of low-cost silicon solar array modules for the LSA Project. This work is based upon the concept of an all metal screeenable electrode ink, investigated in Contract #955164. It was first found that silver powder with lead acting as a liquid sintering medium and with silver fluoride acting as an oxide scavenger, continuous adherent electrode layers result on silicon. During the final phase of the antecedent contract it was shown that base metals such as copper can likewise be sintered to provide an ohmic contact on silicon when appropriately doped. The most successful screened solar cell contacts were achieved using germanium-aluminum and silicon-aluminum eutectics as additions to the pastes for back contacts.

The objectives of the investigation are to provide all metal screenable pastes using economical base metals, suitable for application to low-to-high conductivity silicon of either conductivity type.

3.0 WORK WITH EARLIER COPPER SYSTEMS

3.1 Attempts to Reproduce Earlier AgF-Containing Pastes

Because different batches of silver fluoride used in the paste formulations varied in appearance and form it was believed that this material might be contributing to poor reproducibility of the performance of the formulations. Pastes were prepared using silver fluoride obtained from several sources in order to determine which material would provide optimum adhesion of fired prints and reproduce other desirable results obtained earlier. Silver fluoride sources included: Alfa Chemical Co., Apache Chemical, and Hudson Labs. (the original source). The compositions of the earlier pastes studied are tabulated below.

Solids Composition

Paste Designation	Cu %	AgF %	Pb %	Dopant %	Eutectic Type
SO71	90.0	5.0	5.0	-	-
SO79	86.4	4.8	4.8	4.0	Al/Si
SO80	86.4	4.8	4.8	4.0	Al/Ge

Fifteen different batches of S071 paste were tried. Although the results varied, none achieved the performance of the original materials.

It was found that copper pastes prepared with silver fluoride exhibited a marked change in surface color as a function of time, independent of storage conditions. The surface changed from a reddish-brown color to dark brown and in extreme cases becoming almost black in appearance. Stirring, immediately restored the original color. Pastes containing all ingredients except silver fluoride did not exhibit a color change. While the effect of light upon silver halides is well known, this is not expected to be a factor, since pastes were kept in opaque glass containers. This phenomenon had not been observed with pastes prepared under the previous contract.

It was observed that control of such firing parameters as atmosphere composition and local furnace temperatures was sometimes difficult to maintain.

The firing process was examined, and firing experiments were carried out in three different facilities: (1) AVX Materials Division (forming gas consisting of 90% nitrogen and 10% hydrogen) in a belt furnace, (2) Bernd Ross Associates, two step firing process (5 minutes nitrogen followed by 8 minutes of hydrogen) in a quartz tube furnace and (3) Applied Solar Energy Corporation, two step firing process in a quartz tube furnace.

3.2 Results of Analysis

Figure 1 shows an SEM micrograph of paste SO71 in the dried, green (unfired) condition taken at 850X. Figure 2 shows the same ink printed on silicon and fired by the two step process at 550°C, at the same magnification. Figure 3 is the same electrode at 4250X, both micrographs indicating good sintering action.

Optical micrography was also used as an analytical tool. Figure 4 shows an optical micrograph of SO79 Al,Si eutectic fired at 500°C (two-step) at approximately 200X magnification. Figure 5 shows SO71 fired at 550°C at the same magnification. Despite the higher temperature SO71 appears to be more fine-grained (less sintered). This may be due to the absence of the eutectic phase (aluminum-silicon) which lowers the system melting point of SO79. Figure 6 shows the edge of a screened print of SO71 fired at 550°C (two step) same magnification, and Figure 7 is similarly taken at the center of the electrode. Figure 8 shows a print under the same conditions except fired at a slightly higher temperature 575°C. Since the magnifications are identical on all these micrographs, it is obvious that the 25°C temperature differential in the isochronal sintering experiment leads to significantly greater grain growth.

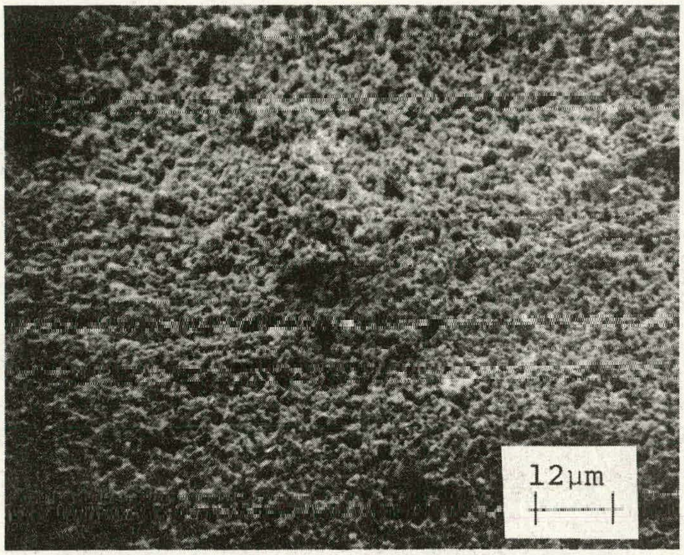

Fig. 1 SEM Micrograph of an unfired S071-A18 print, dried at 900°C, 850X.

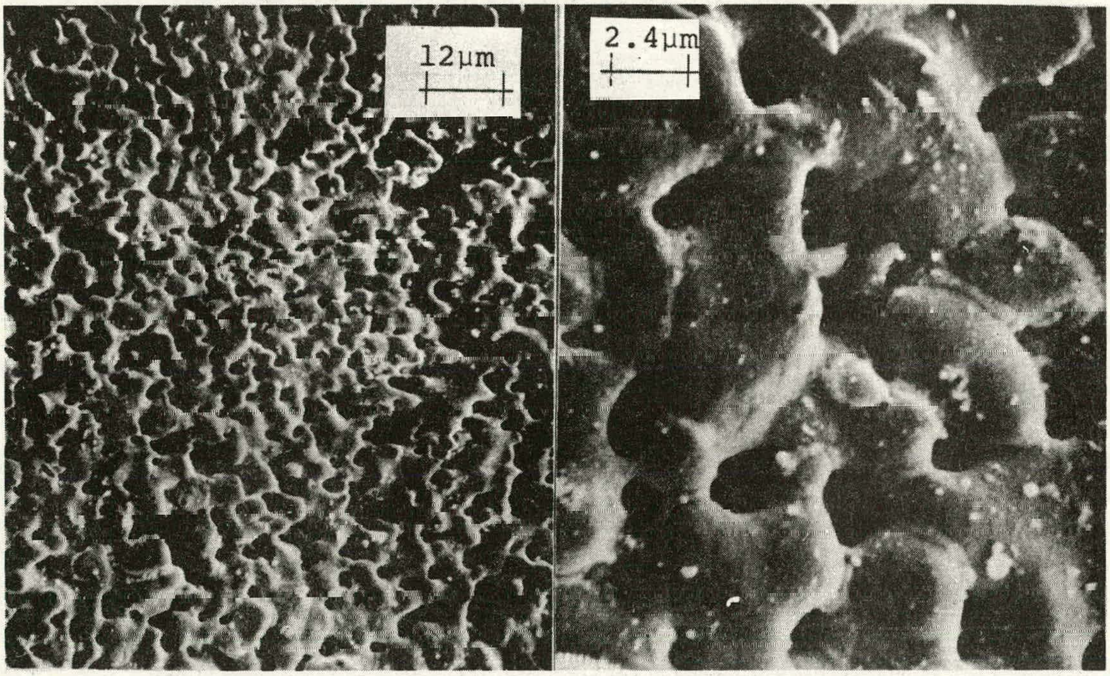

Fig. 2 Mag. 850X Fig. 3 Mag. 4250

SEM Micrograph of S071 print fired at 550°C by the nitrogen-hydrogen two step process.

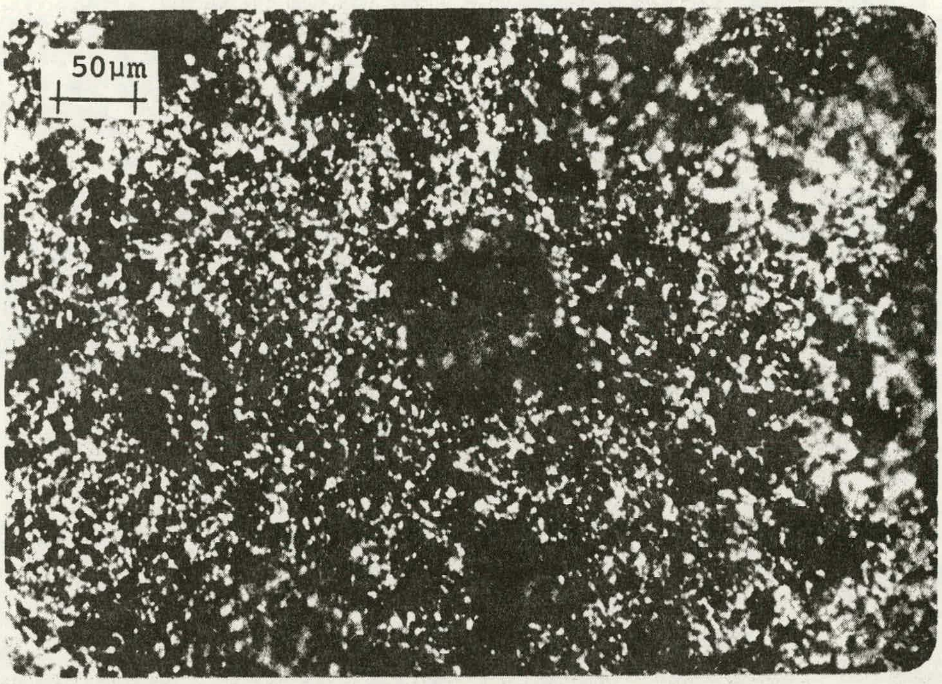

Fig. 4 Optical micrograph of S079A3 print (with eutectic dopant), fired at 500°C (two step) at 200X.

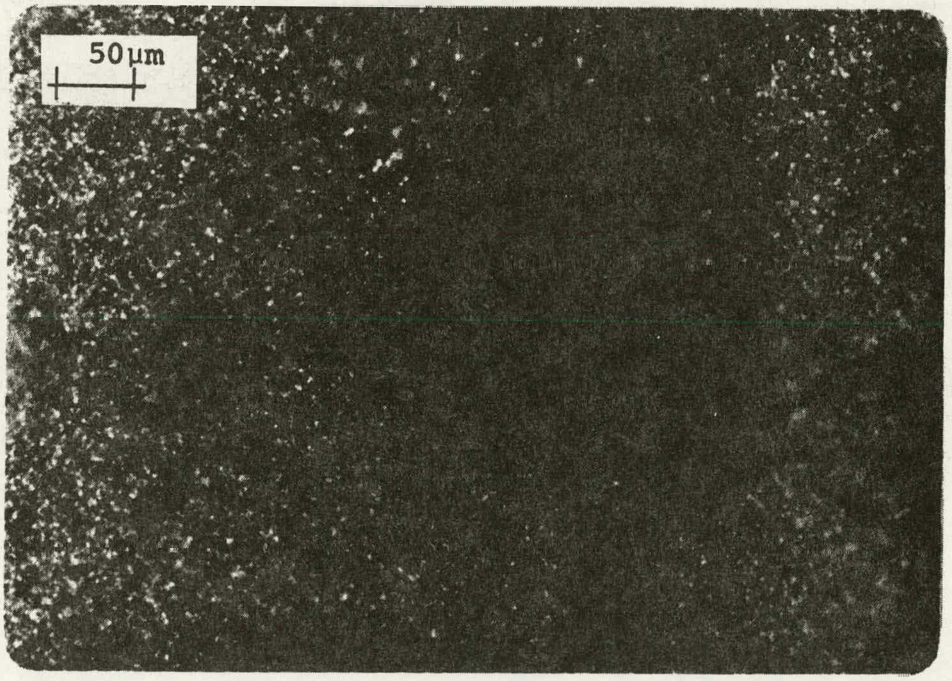

Fig. 5 Optical micrograph of S071A10 print (undoped) fired at 550°C (two step) at 200X.

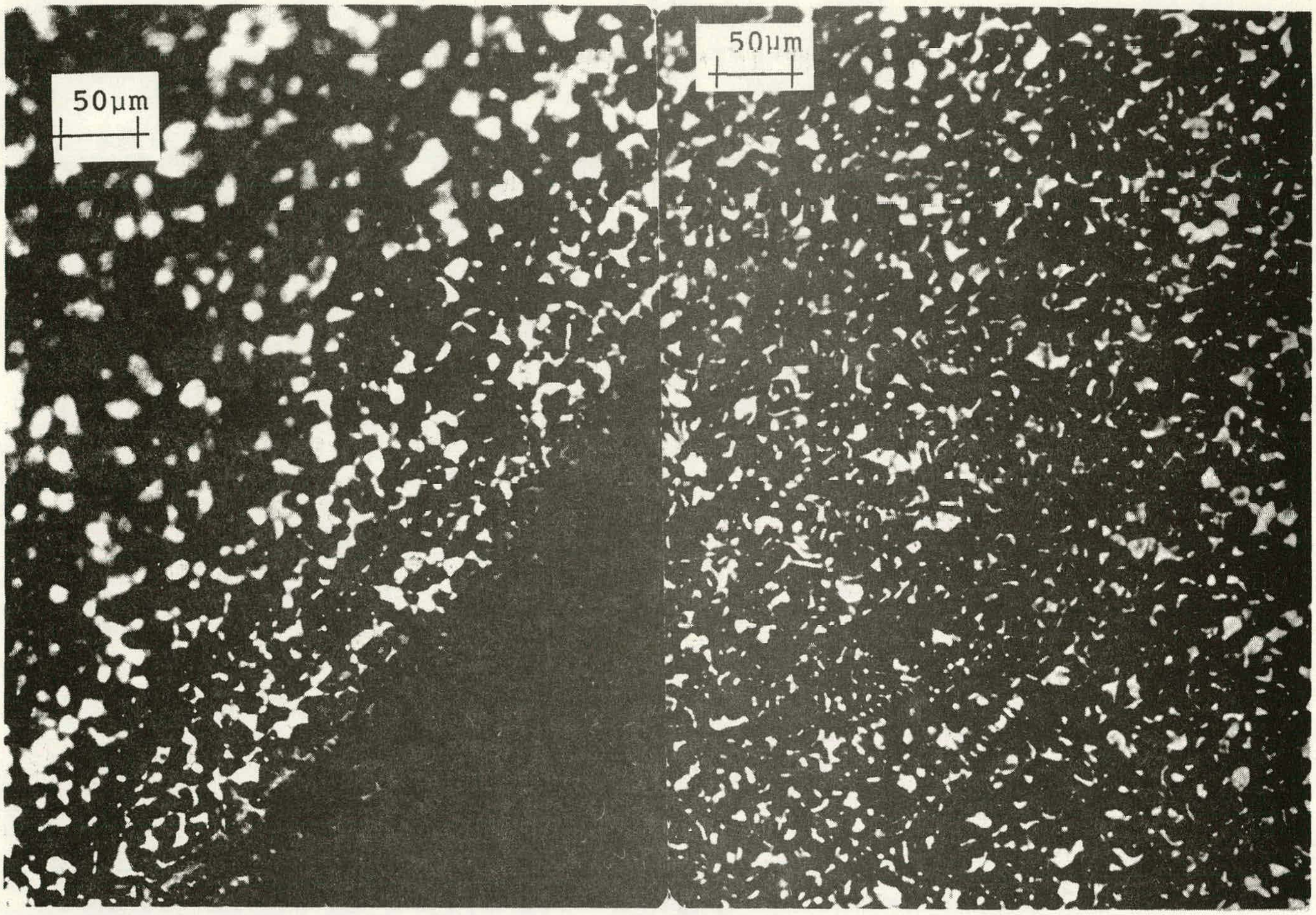

Fig. 6 Edge of print Fig. 7 Center of print
Optical micrograph of S071A9 fired at 550°C. Magnification 200X

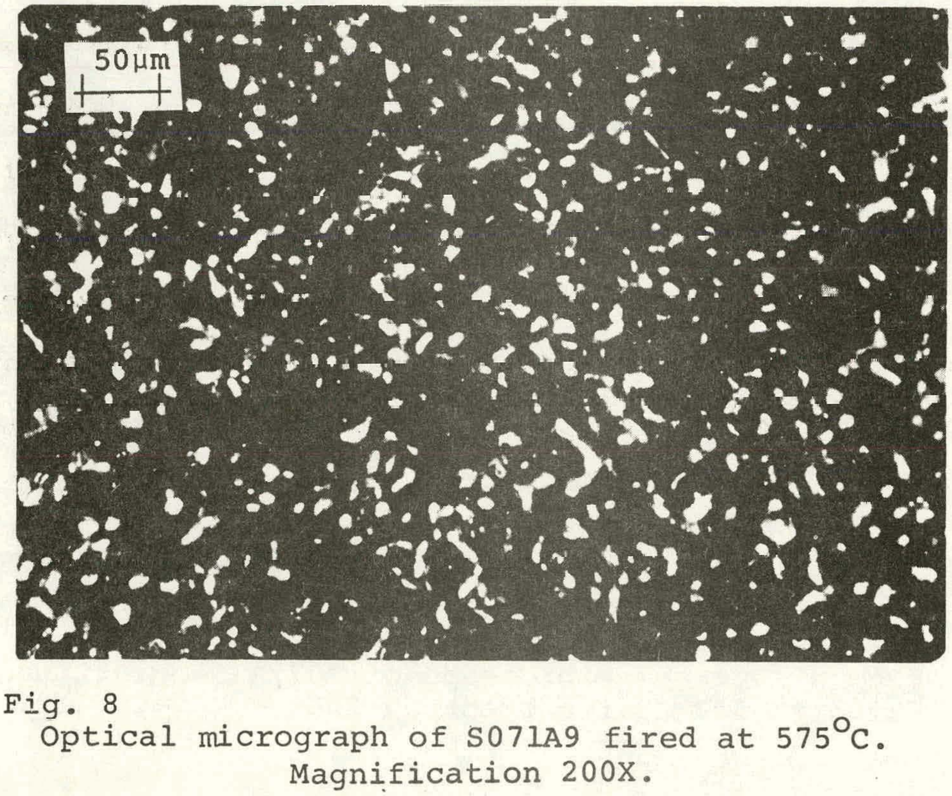

Fig. 8
Optical micrograph of S071A9 fired at 575°C.
Magnification 200X.

4.0 SILVER FLUORIDE-CONTAINING COPPER PASTES

4.1 Paste and Contact Experimentation Silver Fluoride

Most of the initial copper pastes of the present group (F series) gave poor results, with powdery surfaces indicating inadequate sintering and insufficient adhesion. Figure 9 shows a microphotograph of number of test pieces of early electrode paste samples. The Scotch tape strip for the adhesion test is displayed above each sample. Pastes are; from top to bottom, F-5 (AgF), F-6 (AgF) and F-7 (fluorocarbon) and the firing temperatures are, from left to right, 525°C, 550°C, 575°C, 600°C, and 625°C. In some cases the entire electrode lifted from the substrate.

Since adhesion of the copper/silver fluoride pastes was so poor, it was decided to try some of the silver pastes of the previous group (SO series) containing 2% silver fluoride and which had given acceptable adhesion and scratch resistance. Silicon wafers were screened with silver ink SO32 and fired at 550°C in air and by the two-step process. Excellent adhesion was obtained in the case of air-fired silver electrodes. Silver electrodes fired in hydrogen separated from the substrates spontaneously. The silver electrodes removed from the substrates had good sheet integrity and strength.

The structure of the silver electrode sheets is shown in Figures 10 and 11 at 1800x and 9000x respectively. The structure is so well interlocked as to appear oversintered. The smaller circular dots are believed to be a segregated metallic lead phase.

Previously we suspected interference of the hydrogen with the etching action of the fluorine component. The bonds at the silicon surface may be more attractive to hydrogen than other atomic species, based upon the silicon-hydrogen bond strength (71.3 Kcal/mole),[10], Silver fluoride content of the copper pastes ranged from 1.1 wt% to 3.7 wt%. Smaller quantities of silver fluoride were used after an analysis by Dr. Joseph Parker, which pointed to spoiler reactions resulting from the presence of silver fluoride (Section 7.0).

The paste containing the smallest amount of silver fluoride gave the best results to date. One test sample fired in nitrogen at 550°C passed the Scotch tape test (F12). Figures 12 and 13 show SEM micrographs of electrodes resulting from this experiment (shown at 1800x and 9000x, respectively) while the sintering action appears to be moderately good, the surface texture, suggests an oxide coating (particularly at the higher magnification).

One further variation utilized copper flake for the major constituent in paste F15. Electrodes fired at 550°C by the two-step process are shown as SEM micrographs in Figures 14 and 15. Magnifications are 1800x and 9000x, respectively. The electrodes resulting from this had good metallic sheen,

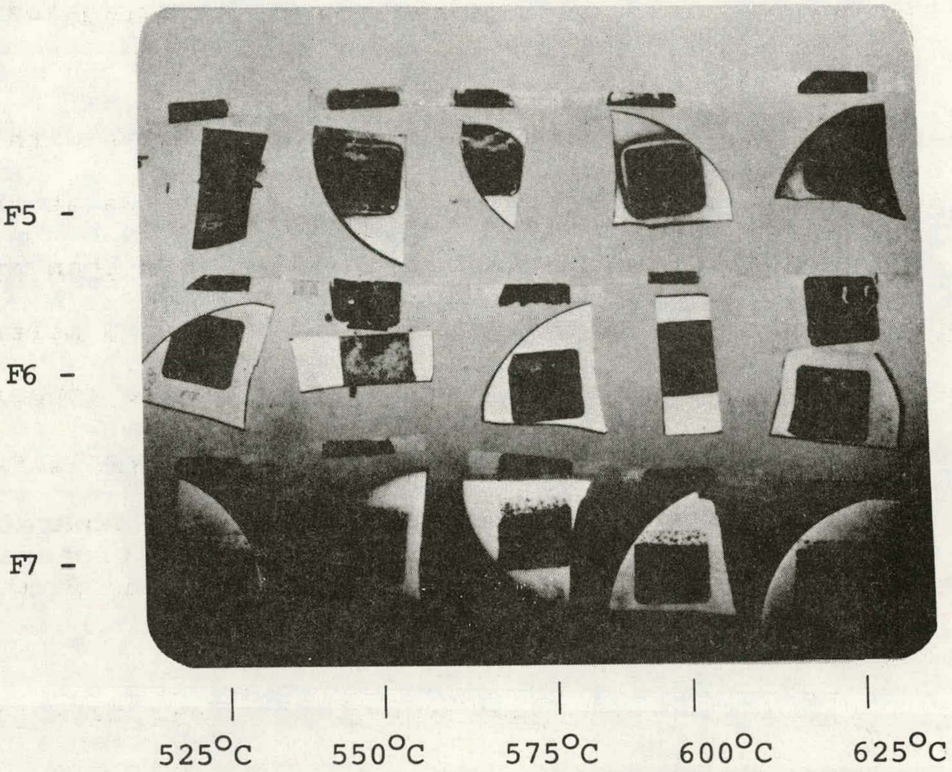

Figure 9. Photograph of 3 pastes with Scotch tape test strips above.

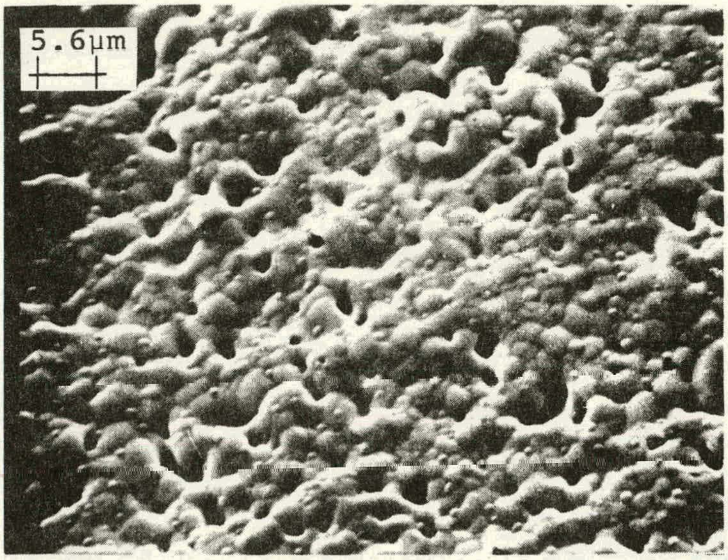

Figure 10 SEM micrograph of S032 silver electrode separated from silicon substrate, fired at 550^{o}C by two step process at 1800x.

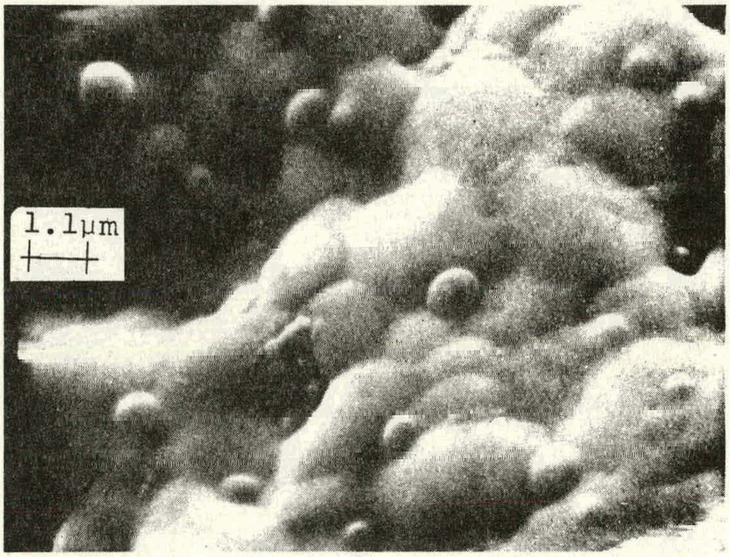

Figure 11 SEM micrograph of S032 silver electrode separated from silicon substrate, fired at 550^{o}C by two step process at 9000x.

presumably due to the orientation of the major flake plane, but poor adhesion and cohesion. In addition, the flakes tended to coat the screen wire mesh. SO80 electrodes fabricated during a solar cell experiment under the previous contract[3] were reexamined. A fragment of a solar cell which originally had a copper contact applied with initially good adhesion, was found to have the contact partially separated. The electrode metal was curved away from the silicon substrate, indicative of strain, in the sense of contraction relative to the silicon. This is as would be expected from the thermal behavior of copper relative to silicon. The thermal expansion coefficients of copper, lead and silicon are, respectively:

$$\text{Copper}\quad \frac{1}{L}\,\frac{\partial L}{\partial T} = 17.71\cdot 10^{-6}\ (^\circ C)^{-1}$$

$$\text{Lead}\quad \frac{1}{L}\,\frac{\partial L}{\partial T} = 28.9\cdot 10^{-5}\ (^\circ C)^{-1}$$

$$\text{Silicon}\quad \frac{1}{L}\,\frac{\partial L}{\partial T} = 2.56\cdot 10^{-6}\ (^\circ C)^{-1}$$

If appropriately sintered, a copper grain matrix exists at the end of the sintering step, which took place at 550°C in the subject device. The amount of strain resulting from the mismatch is 0.05 cm. Assuming the diameter of the solar cell to be 2.25 inches or 5.72 cm and the copper grain matrix to cool through 520°C without relaxation, the calculated radius of curvature of the electrode is 45.5 cm.

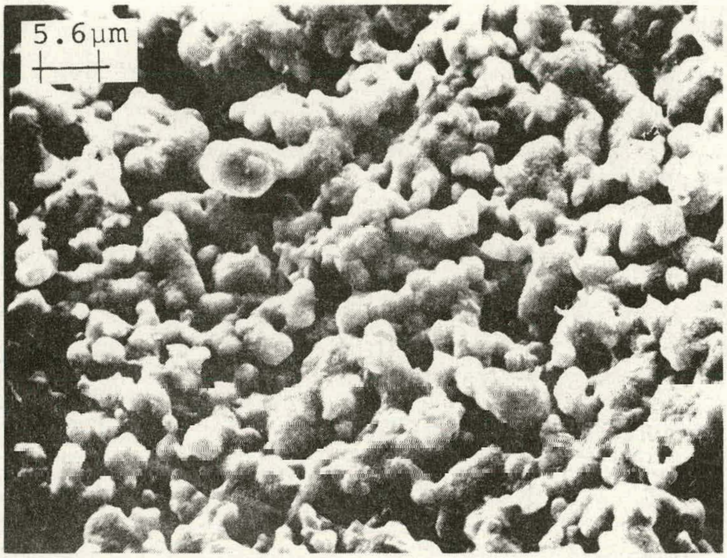

Figure 12 SEM micrograph of F12 electrode fired in nitrogen at 550^{o}C, at 1800x.

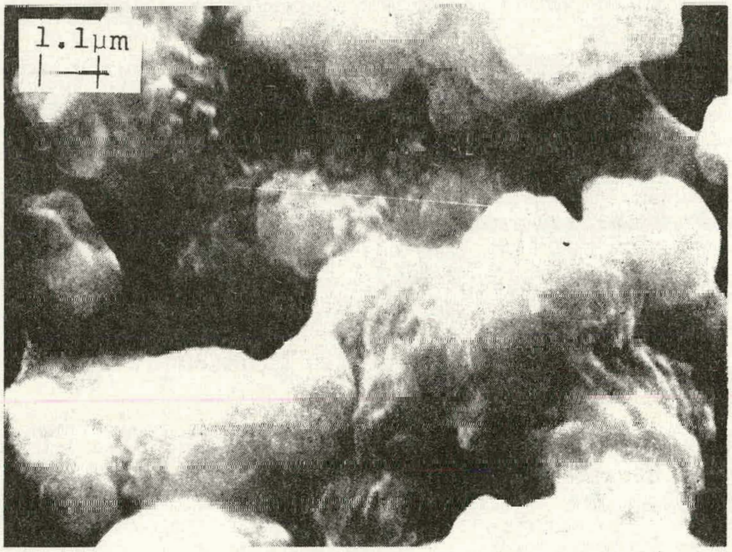

Figure 13 SEM micrograph of F12 electrode fired in nitrogen at 550^{o}C, at 9000x.

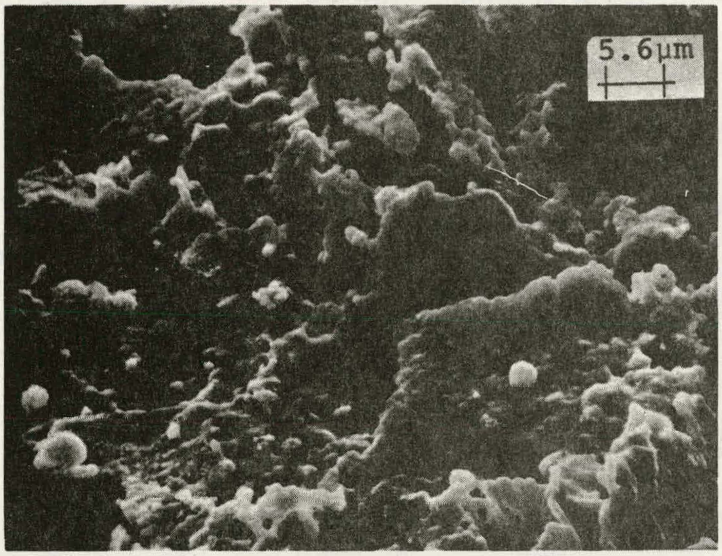

Figure 14 SEM micrograph of F15 copper paste with flake copper and silver fluoride, fired by the two step process at 550°C, at 1800x.

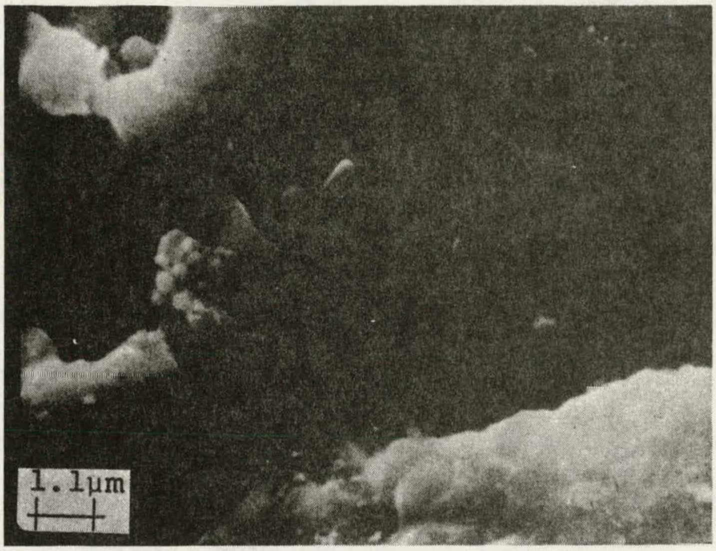

Figure 15 SEM micrograph of F15 copper paste with flake copper and silver fluoride, fired by the two step process at 550°C, at 9000x.

While the initial adhesion of S080 paste was excellent it appears that longterm storage (approximately 18 months) caused catastrophic spalling of the copper electrode. While the causes for this are not known, it may be that the relatively thick and densely sintered electrode could not withstand ambient thermal excursions.

4.2 Solar Cell Experiments

The solar cell experiments were done with pastes S071 and S093 involving the front contact. The first of these utilized wafers with various junction depths and silicon oxide coatings. The experimental parameters were described in detail in reference 4. Due to poor adhesion no electrical data could be obtained.

In a second experiment, paste F20 was utilized on cells with a junction depth of approximately 0.5 μm and an SiO_2 anti-reflection coating. As in the first experiment the contact was screened on the AR coating with the intent of firing through. The contact adhesion problem was again sufficient to prevent the taking of solar cell measurement data.

A solar cell experiment was carried out utilizing F-31 and F-32 copper pastes. Details of this experiment are given in Table I and Figures 16 through 19. The major factor in this experiment was the comparison of electrodes containing 0 wt. % (F-31) and 5 wt. % (F-32) Al/Si eutectic. The nitrogen fired cell IV curve shows the characteristic typical of a Schottky barrier in series with the PN junction.

TABLE I

SOLAR CELL EXPERIMENT

F31 copper paste with 0.1 wt % AgF, 10 wt % Pb and 0 wt % Al-Si eutectic

F32 copper paste with 0.1 wt % AgF, 10% Pb and 5 wt % Al-Si eutectic

Paste	Firing Temperatures (°C)	Qty	Ambient Gas	Average Uncoated Efficiency AMI %	Average Fill Factor
F31	550	3	N_2	5.9	0.476
F31	550	3	CO	7.7	0.637
F31	600	3	CO	6.5	0.551
F31	650	3	CO	8.1	0.676
F32	550	3	CO	7.1	0.660
F32	600	3	CO	8.0	0.722
F32	650	3	CO	7.5	0.739

Figure 20 shows a distribution of points on a fillfactor plot. The dots on this plot were collected from previous experiments. The crosses represent data from the present experiment. The plot shows that it is possible to get relatively high (0.74) fillfactors even without eutectic additions, however, the data scatter is quite significant. In the case of the 5 wt. % Al-Si eutectic addition, the point grouping is considerably tighter. The data in Table I also

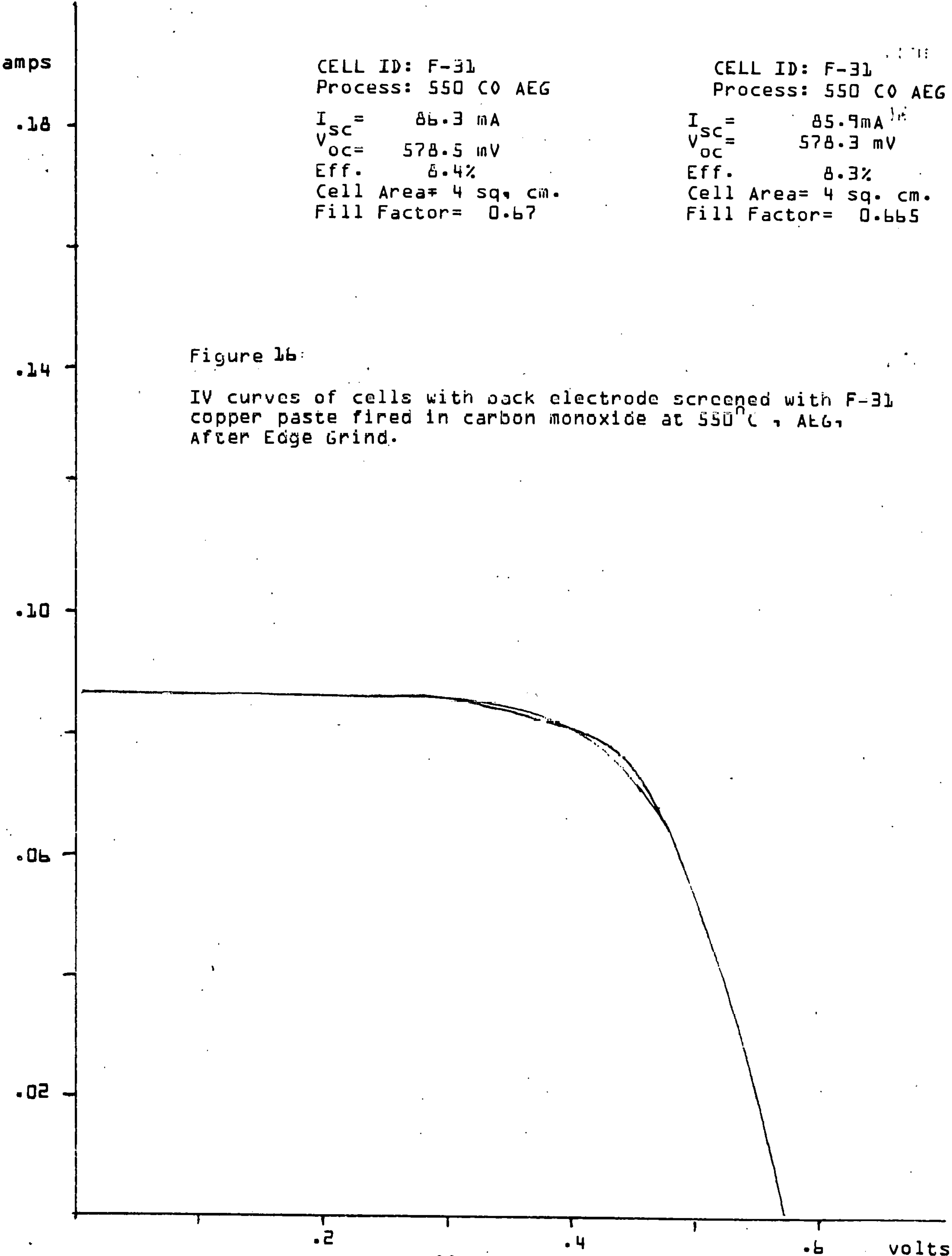

CELL ID: F-31
Process: 550 CO AEG
I_{sc}= 86.3 mA
V_{oc}= 578.5 mV
Eff. 8.4%
Cell Area= 4 sq. cm.
Fill Factor= 0.67

CELL ID: F-31
Process: 550 CO AEG
I_{sc}= 85.9mA
V_{oc}= 578.3 mV
Eff. 8.3%
Cell Area= 4 sq. cm.
Fill Factor= 0.665

Figure 16

IV curves of cells with back electrode screened with F-31 copper paste fired in carbon monoxide at 550°C , AEG, After Edge Grind.

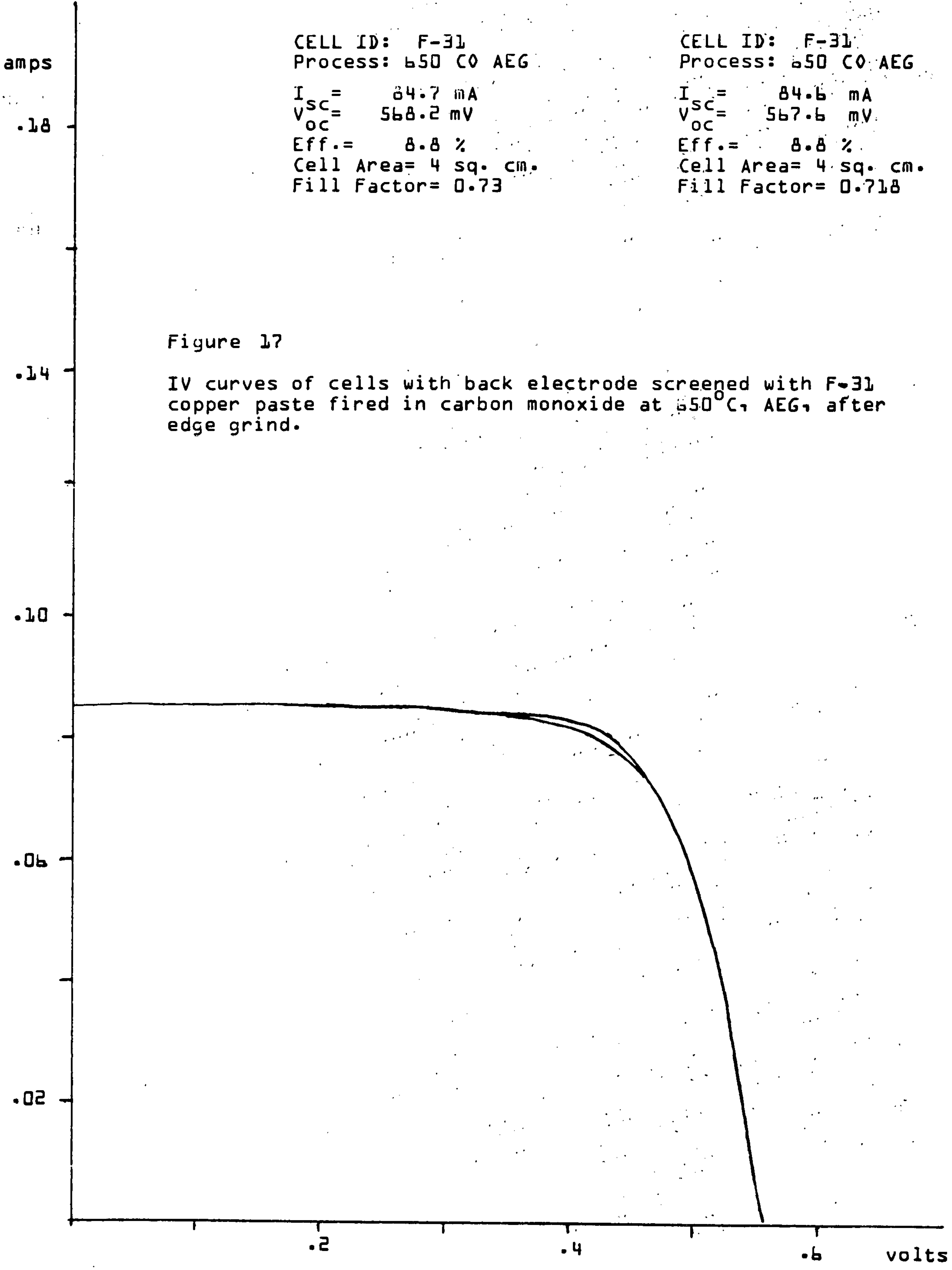

CELL ID: F-31
Process: 650 CO AEG
I_{sc}= 84.7 mA
V_{oc}= 568.2 mV
Eff.= 8.8 %
Cell Area= 4 sq. cm.
Fill Factor= 0.73

CELL ID: F-31
Process: 650 CO AEG
I_{sc}= 84.6 mA
V_{oc}= 567.6 mV
Eff.= 8.8 %
Cell Area= 4 sq. cm.
Fill Factor= 0.718

Figure 17

IV curves of cells with back electrode screened with F-31 copper paste fired in carbon monoxide at 650°C, AEG, after edge grind.

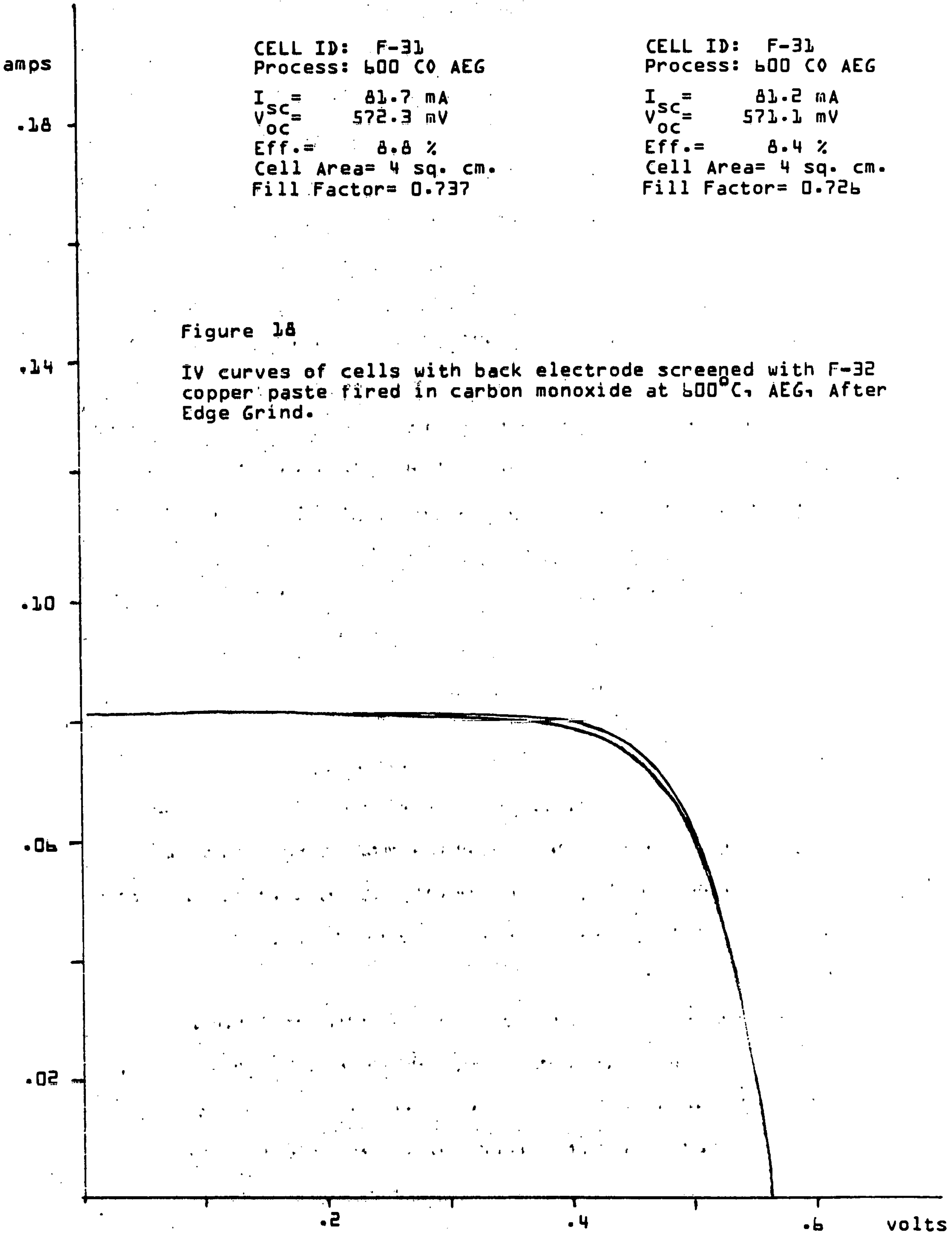

CELL ID: F-31
Process: 600 CO AEG
I_{sc}= 81.7 mA
V_{oc}= 572.3 mV
Eff.= 8.8 %
Cell Area= 4 sq. cm.
Fill Factor= 0.737

CELL ID: F-31
Process: 600 CO AEG
I_{sc}= 81.2 mA
V_{oc}= 571.1 mV
Eff.= 8.4 %
Cell Area= 4 sq. cm.
Fill Factor= 0.726

Figure 18

IV curves of cells with back electrode screened with F-32 copper paste fired in carbon monoxide at 600°C, AEG, After Edge Grind.

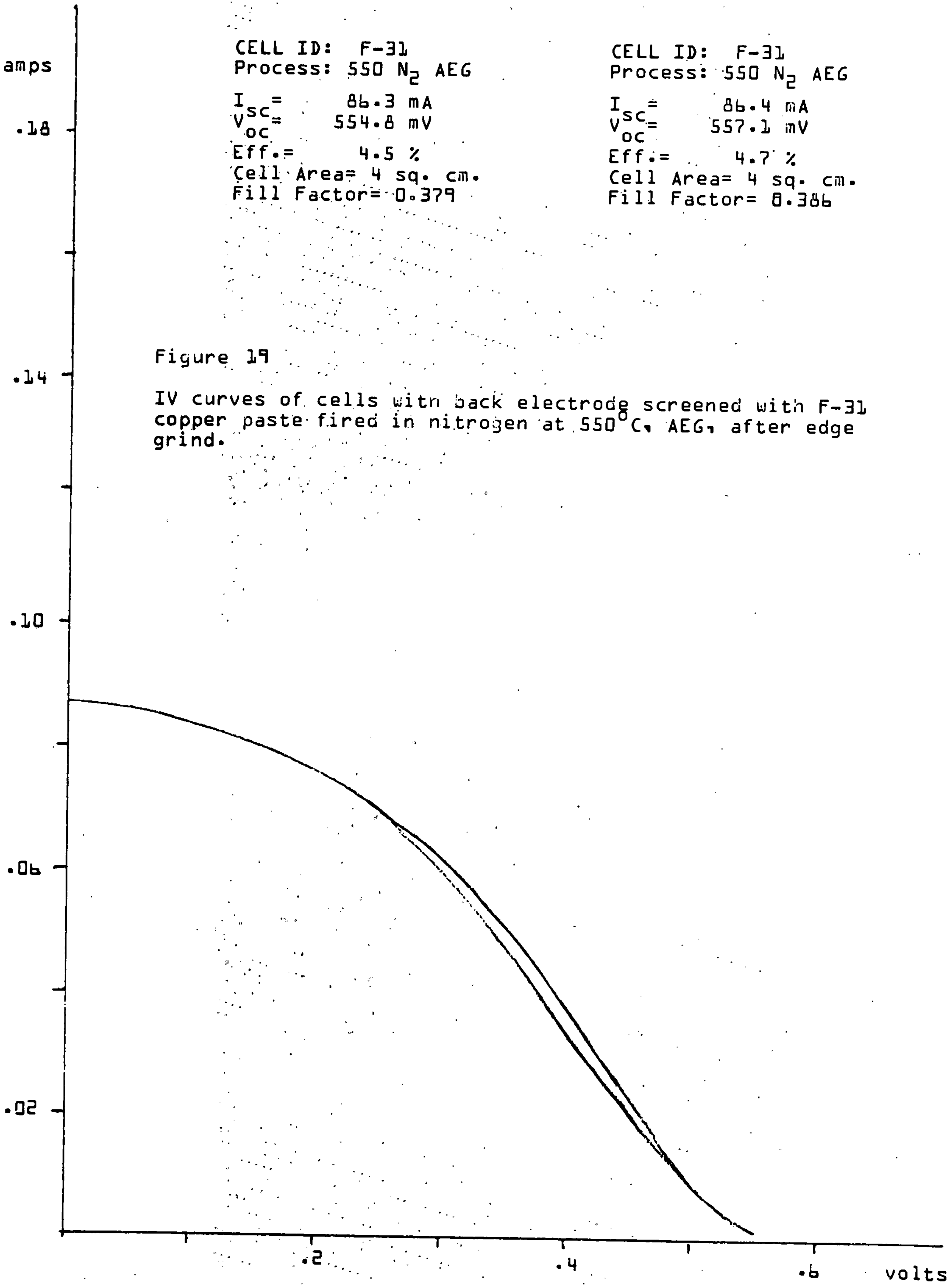

Figure 19

IV curves of cells with back electrode screened with F-31 copper paste fired in nitrogen at 550°C, AEG, after edge grind.

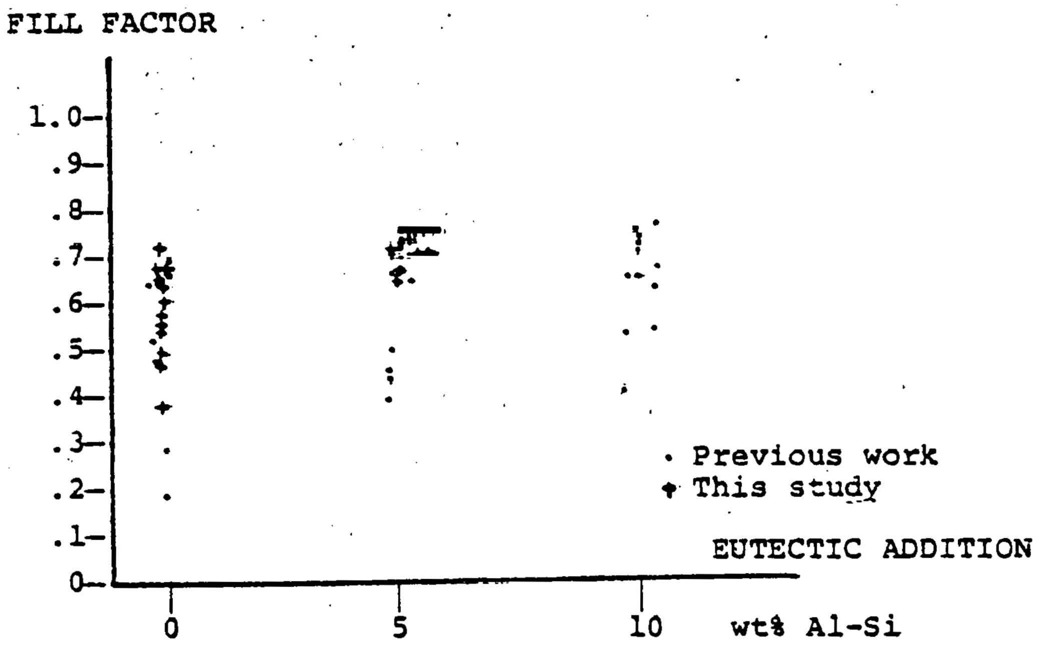

Figure 20 Fill factor versus amount of Al-Si eutectic addition to screened back electrode copper paste

indicates that the higher temperatures give generally better contacts and fillfactors.

SEM studies on F32 and F31 fired copper pastes suggested poor sintering on the aluminum-silicon containing paste F32. While the Al-Cu phase diagram is complex, there is no indication of an intermetallic compound formation. F31 showed normal sintering behavior.

Silver fluoride from two sources was utilized. Type "H" silver fluoride, packed in a plastic bottle appeared quite wet, with visible liquid moisture in evidence. Melting occurred at approximately 300°C (melting point for dry material is approximately 435°C) for "H" material, accompanied by bubbling and after reaction to metallic silver a glassy residue was in evidence. Type "A" silver fluoride, packed in a plastic bag within a glass jar, showed considerably less moisture, however, grain agglomeration indicated a moisture problem still exists. Type "A" material melted closer to the published melting point, and no macroscopic amounts of residue were seen. SEM micrography showed evidence of the existence of small amounts of glassy material for type A silver fluoride also.

One may conclude that the use of silver fluoride in pastes requires careful evaluation of source material, for initial moisture content. Further, extreme care must be exercised to maintain the silver-fluoride powder in a dry state, by maintaining the material in a desiccated atmosphere and allowing minimum exposure to ambient atmospheres during handling operations.

Once the material has been added to a paste-containing vehicle, these procedures may be relaxed, as the vehicle coating provides some protection.

A solar cell experiment was begun with 100 diffused 2x2cm wafers furnished by the JPL Process Research Laboratory (PRL).

The experimental protocol was as follows: Front contact phase, Four pastes were prepared and screened as front contacts. Paste compositions are given in Table II.

TABLE II

FRONT CONTACT PASTE COMPOSITIONS

PASTE CODE	VEHICLE TYPE	VEHICLE WT%	COPPER WT%	SILVER FLUORIDE WT%	LEAD WT%
F 38	V19	25	71.25	0.0	3.75
F 39	V19	25	70.58	0.7	3.72
F 42	V19	25	69.82	1.5	3.68
F 43	V19	25	68.4	3.0	3.60

Three cells each were prepared for firing at 550°C and 600°C.

Back contact phase cells were screened with F26 paste backs. F26 is similar to F31 28 wt. % vehicle 64.8 wt. % Cu 6.5 wt. % Pb and 0 wt. % AgF, except for a vehicle rheology adjustment. A group of cells was provided with screened backs, fired, and then equipped with screened copper front contacts. A group of cells was provided with screened copper front contacts only, to be metallized with titaninum-palladium-silver (Ti-Pd-Ag) backs by JPL PRL. A group of cells with an oxide layer of approximately 1000Å was provided with screened copper front contacts only, to be metallized with Ti-Pd-Ag backs by JPL PRL.

A group of cells was provided with screened copper back contacts only, to be metallized with Ti-Pd-Ag by JPL PRL.

A group of wafers was returned ty JPL PRL for front and back Ti-Pd-Ag metallization as control cells.

During and after firing it was noticed that adhesion was still a problem, particularly on front contacts providing a reduced number of cells for further processing and final testing.

Results of testing and analysis of the front and back contact solar cell experiment are reproduced in Table III. These data are based on bare cells without AR coating. Where categories are left blank, cells were not testable.

Since the silver fluoride increases with rising paste number (see Table III, F38 0 wt. % AgF, F43 3 wt. % AgF), one might look for increasing leakage (or decreased shunt resistance) in this direction. However, while all the copper paste front contacts had poor shunt resistance, no trend can be seen. Similarly, it was expected that the oxide would help protect the diffused layer, but this cannot be supported by the data. The open circuit voltages of the four categories having screened copper contacts on bare silicon diffused layers are surprisingly high, equalling the value of the control cells

(507 mV).

Typical IV curves for each category are shown in Figures 21 through 23.

TABLE III

FRONT AND BACK CONTACT SOLAR CELL EXPERIMENT (MEANS, USUALLY 3 SAMPLES)

CONTROLS	OPEN CIRCUIT VOLTAGE (mV)	EFFICIENCY(%) (no AR)	FILL-FACTOR	SERIES RESIST. (ohms)	SHUNT RESIST. (ohms)
Front & Back Ti-Pd-Ag	507	8.2	0.73	0.43	356
Front Ti-Pd-Ag	521	6.1	0.55	2	248
Back F26 600°C Front F38 550°C	504	1.5	0.22	-	11
Front F38 600°C	507	1.3	0.21	23	11
Front F39 550°C	512	0.8	0.30	31	37
Front F39 600°C	506	1.8	0.23	18	10
Front Ox F42 550°C	430	0.2	0.35	66	158
Front Ox F42 600°C	196	0.7	0.24	3.9	3.6
Front Ox F43 550°C	-	-	-	-	-
Front Ox F43 600°C	285	1.1	0.27	9	9
Back Ti-Pd-Ag Front F38 550°C	-	-	-	-	-
Front F38 600°C	-	-	-	-	
Front F39 550°C	-	-	-	-	-
Front F39 600°C	-	-	-	-	-

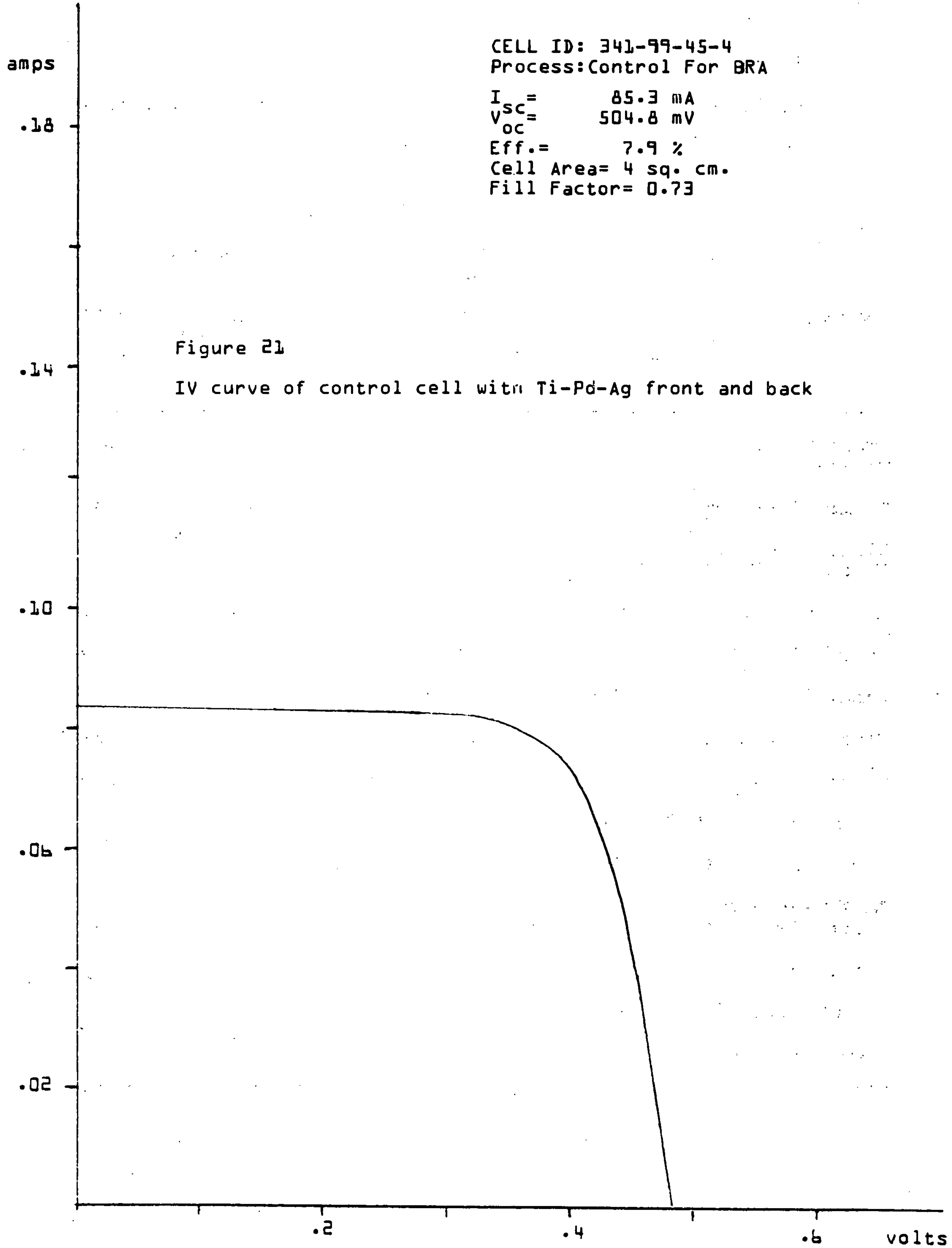

CELL ID: 341-99-45-4
Process:Control For BRA
I_{sc}= 85.3 mA
V_{oc}= 504.8 mV
Eff.= 7.9 %
Cell Area= 4 sq. cm.
Fill Factor= 0.73

Figure 21

IV curve of control cell with Ti-Pd-Ag front and back

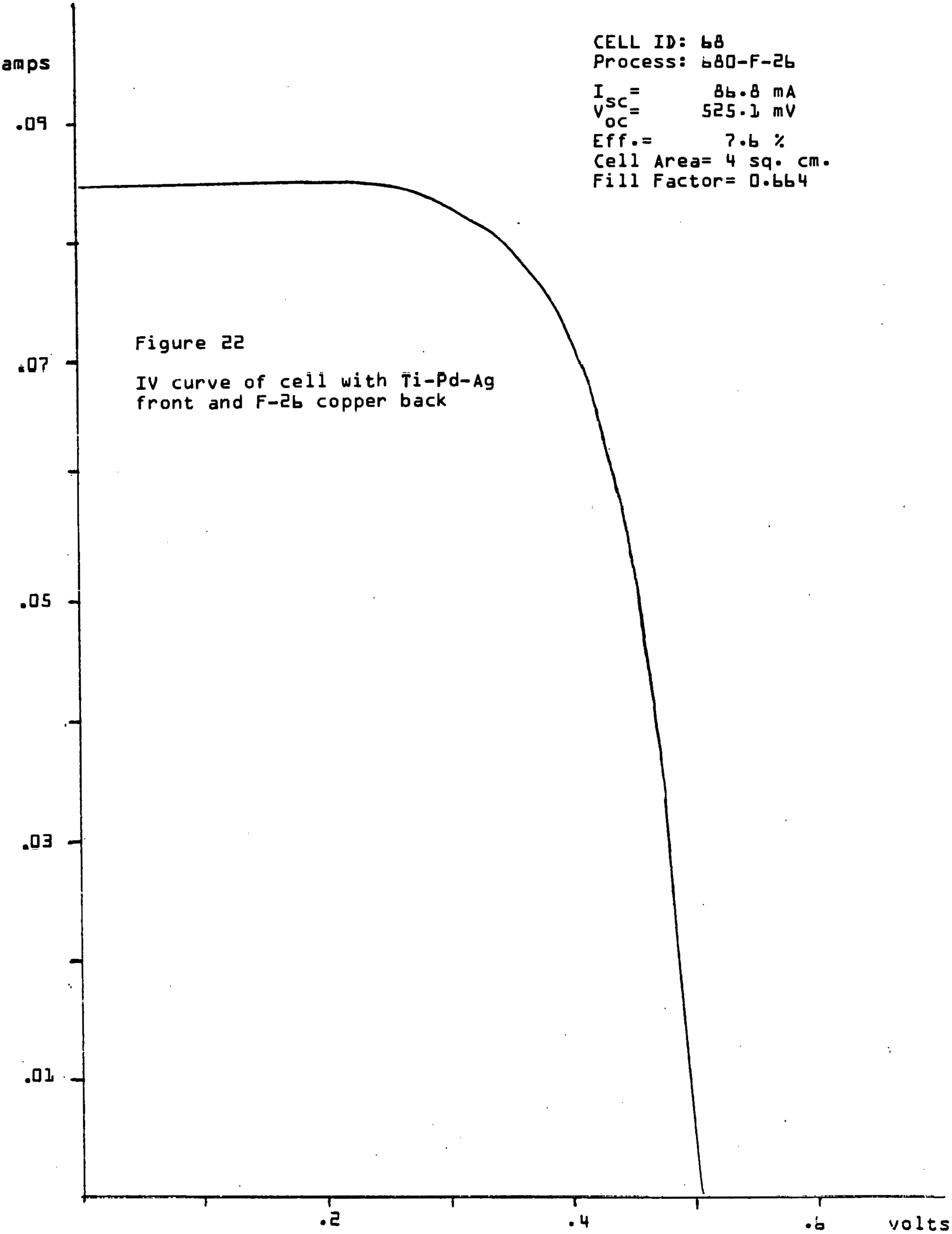

CELL ID: 68
Process: 680-F-26
I_{sc}= 86.8 mA
V_{oc}= 525.1 mV
Eff.= 7.6 %
Cell Area= 4 sq. cm.
Fill Factor= 0.664

Figure 22

IV curve of cell with Ti-Pd-Ag front and F-26 copper back

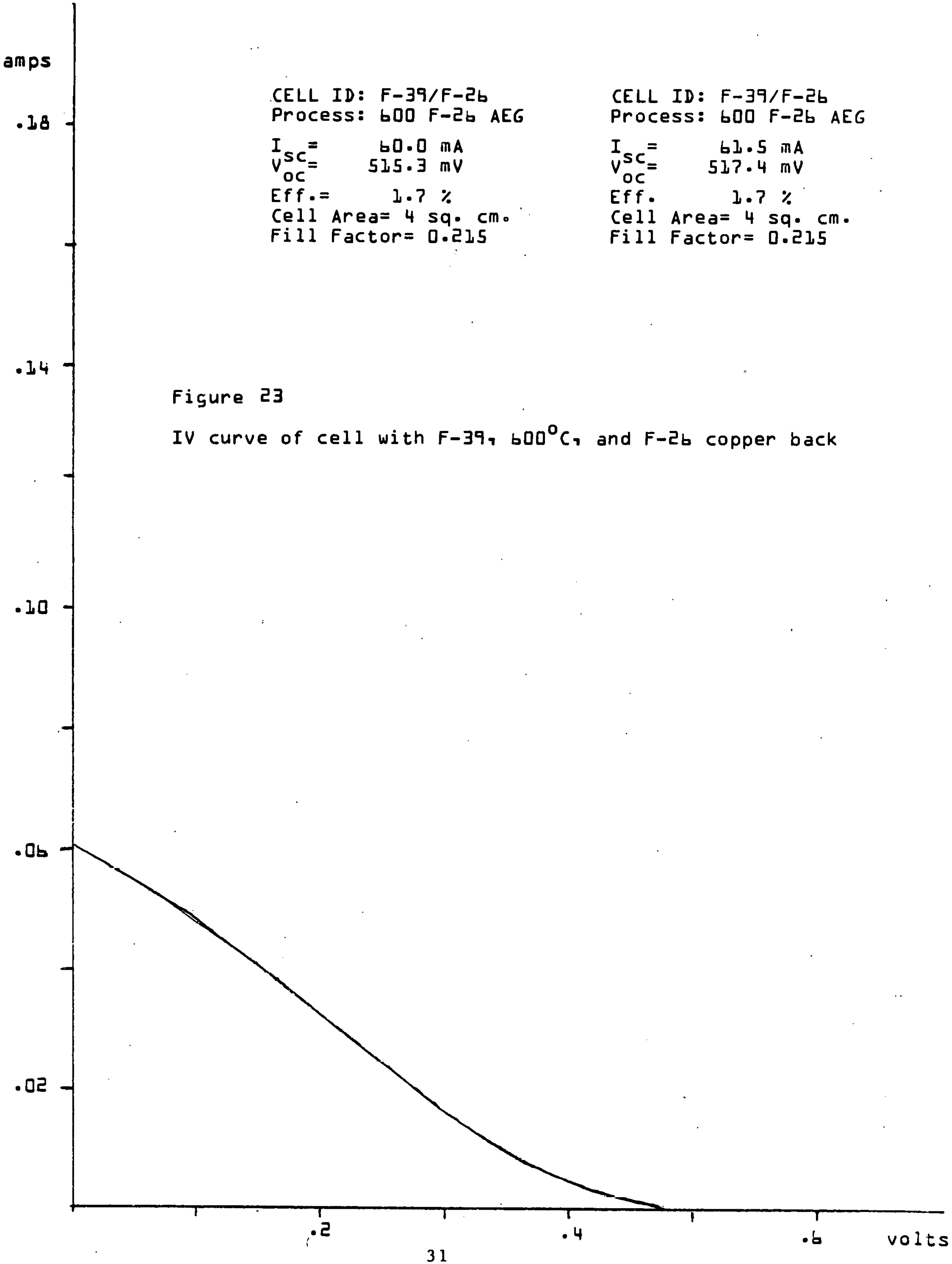

CELL ID: F-39/F-26
Process: 600 F-26 AEG
I_{sc}= 60.0 mA
V_{oc}= 515.3 mV
Eff.= 1.7 %
Cell Area= 4 sq. cm.
Fill Factor= 0.215

CELL ID: F-39/F-26
Process: 600 F-26 AEG
I_{sc}= 61.5 mA
V_{oc}= 517.4 mV
Eff. 1.7 %
Cell Area= 4 sq. cm.
Fill Factor= 0.215

Figure 23

IV curve of cell with F-39, 600°C, and F-26 copper back

4.3 Results of Analysis

A simple Scotch^{r} tape adherence test was devised to allow crude, instant evaluation of the results of electrode tests. Likewise a scratch test, that allows comparative analysis of the electrode strength, was initiated.

During the present reporting period a number of pastes manufactured previously with varying parameters were analyzed. The manual screening was improved to allow reproducible registration and constant snapoff distance (.012"). The tube furnace was profiled again with the standard platinum - platinum plus 13% rhodium thermocouple and a digital microvoltmeter. An error was found on the furnace chromel-alumel thermocouple. Spot checks with platinum reference thermocouple were made routine on all firings. Some variation in firing was found, leading to some suspicion of potential downstream sample contamination from contaminated furnace tube, gas or exudant from upstream samples.

Problems with electrode prints were:

1) Lack of adhesion, possibly due to inadequate reduction of oxide, (silicon surface and powder grain surfaces) or tying up of dangling surface bonds by hydrogen atoms.
2) Poor sintering due to inadequate liquid transport (discussed in Section 5.1).

Samples of characterization attempts of successful and unsuccessful pastes are shown in the following figures. Figure 24 depicts four optical photomicrographs of successful S080 sub-

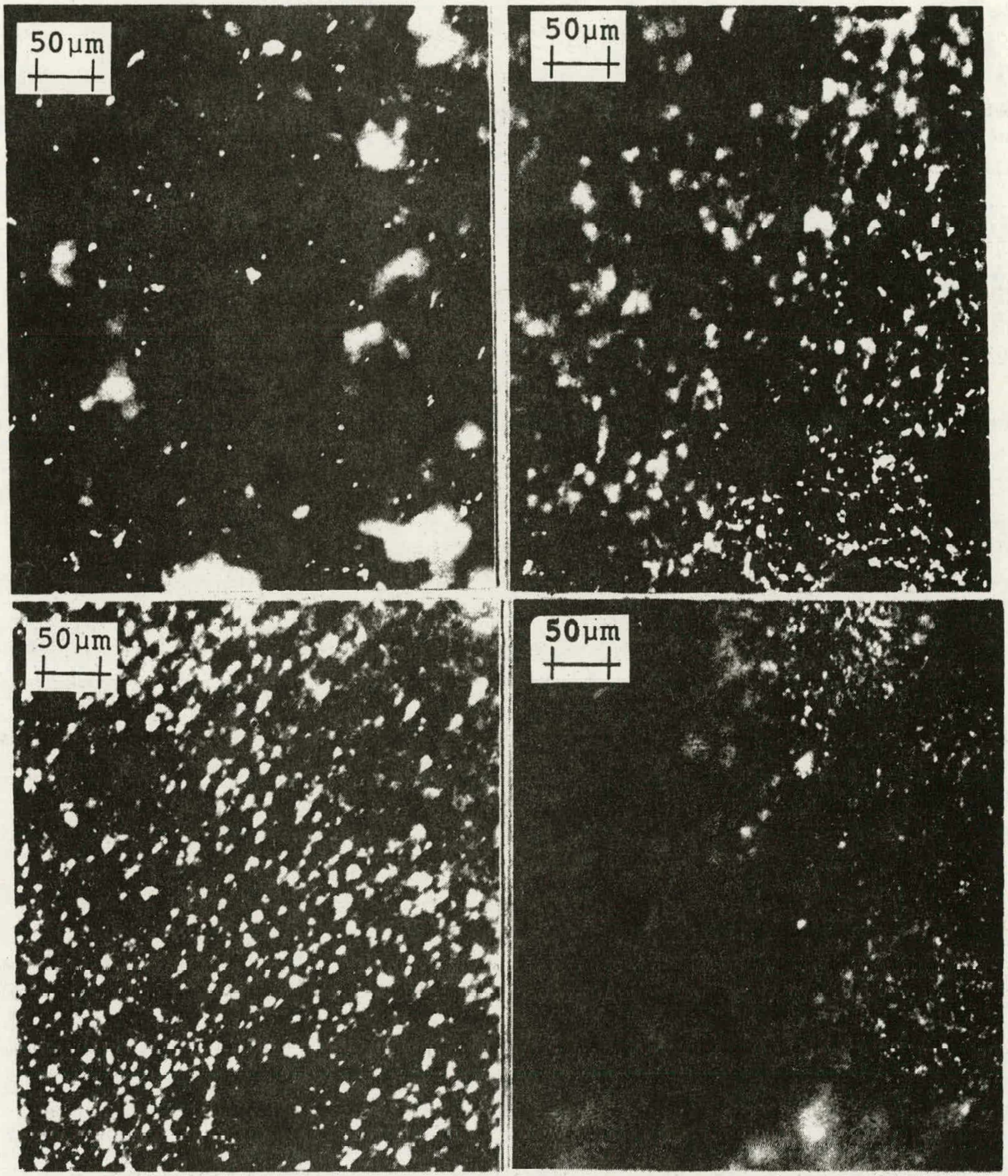

Figure 24 Optical micrographs of S080 successful and S079 unsuccessful screened prints with experimental copper pastes.
LEFT SIDE, TOP: Silicon substrate under good S080 print (electrode removed by acid etch).
BOTTOM: Silicon substrate of S079 print (electrode peeled spontaneously).
RIGHT SIDE, TOP: S080 successful electrode print.
BOTTOM: S079 unsuccessful electrode print.
Magnification 200X

strates (upper left) and SO80 print (upper right) and unsuccessful SO79 substrate (lower left) and SO79 print (lower right). In the case of the substrates the SO80 electrode was removed by etching with concentrated nitric acid, and the SO79 electrode print peeled spontaneously. The difference between SO80 and SO79 is the use of germanium-silicon eutectic at 5wt.% in the former and aluminum- silicon eutectic in the latter.

The major observable difference in the micrographs is the larger grain size and coarser faceting in the case of the successful SO80 paste.

Figure 25 shows a composite of SEM micrographs depicting an unsuccessful SO80 electroding experiment. The substrate is shown on the left side and the electrode on the right, both at 1800x and at 4500x. The firing of this paste at 550°C by the two step process resulted in a small degree of sintering, making the micrograph resemble that of a powder. By contrast, Figure 26 shows a successful print of the SO80 paste taken on a Cambridge SEM at roughly two magnifications 1800 - 1900x, and 4500 - 4700x. The striking appearance of the copper silicon eutectic needle structure dominates the pictures of the silicon substrate. On the right the electrode can be seen.

Figures 27 and 28 show black and white reproductions of the color readout of Xray dispersive spectra of successuful SO80 electrodes and the silicon substrate, respectively. The spectra allow reading of the lines of copper (Cu), Aluminum

(Al), lead (Pb) silicon (Si) and silver (Ag) in Figure 27 and silicon, aluminum silver, copper and the tin (Sn) in Figure 28. The figures are shown only as illustrative of the method, as no clues for the differences in performance could be obtained from the spectra.

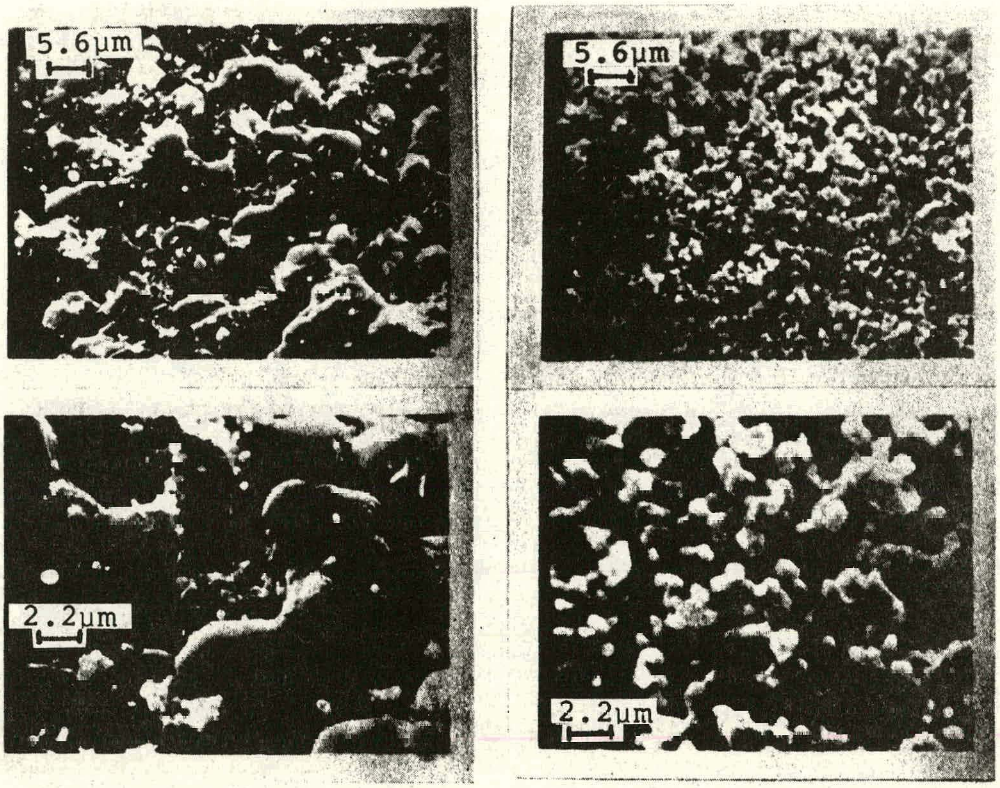

Figure 25 Composite of SEM micrographs of S080 unsuccessful electroding experiment.
Left Side: Substrate.
Right Side: Electrode.

Figure 26 Composite of SEM micrographs of S080 successful screen print.
Left Side: Silicon substrate.
Right Side: Electrode.

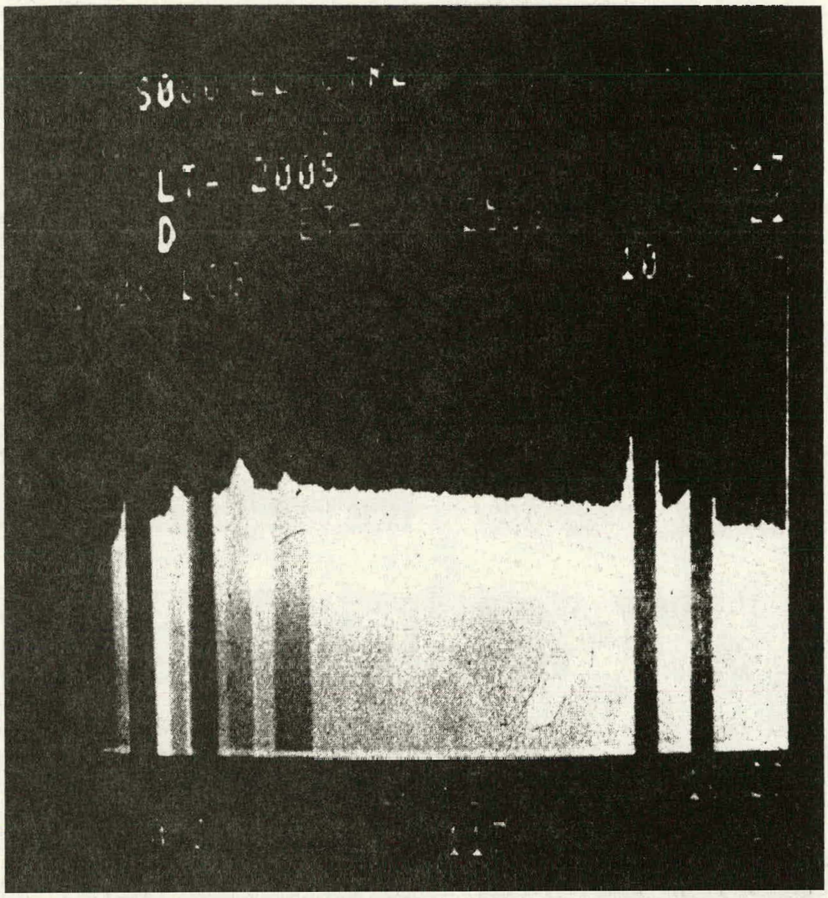

Figure 27 Black and white reproduction of color coded Xray dispersive spectrum of successful S080 electrode.

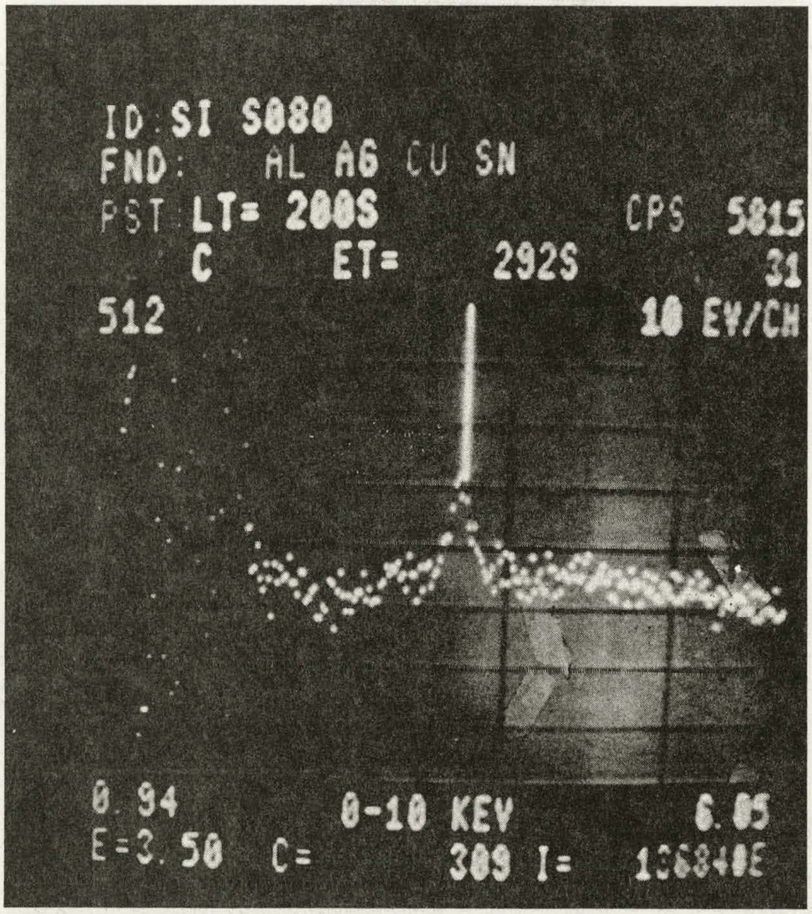

Figure 28 Black and white reproduction of color coded Xray dispersive spectrum of successful S080 electrode.

5.0 FLUOROCARBON CONTAINING COPPER PASTES

5.1 Paste, Contact Experiments and Analysis

During the present contract, paste formulation was transferred to a new subcontract facility. The purpose of this change was to allow more intimate control of material and process by direct contract personnel.

Initial experiments with fluorocarbon pastes gave unsatisfactory results, both from an adhesive and a sintering standpoint. Figures 29 and 30 show an example of an electrode which exemplifies the problem. Microscopic examination of the lead raw material showed that a high percentage of the grains were quite large (∿ 50 μm), resulting both in poor distribution of the liquid sintering medium, as well as the possibility of the printing screen acting as a sieve. This would hold back a portion of the lead component, upsetting the intended compositional ratios, and could explain the problem of undersintering.

This problem was eliminated by sifting the available powder through a #400 stainless steel screen. Some improvement in sintering resulted from this procedure, however the adhesion problem remained. In addition to problems with excessive particle size in lead, copper powder from suppliers other than Colonial Metal Corporation also had too large a particle size distribution (large particle diameters). However, one batch of copper received from Colonial Metals Corporation was below specifications for particle size and gave problems with

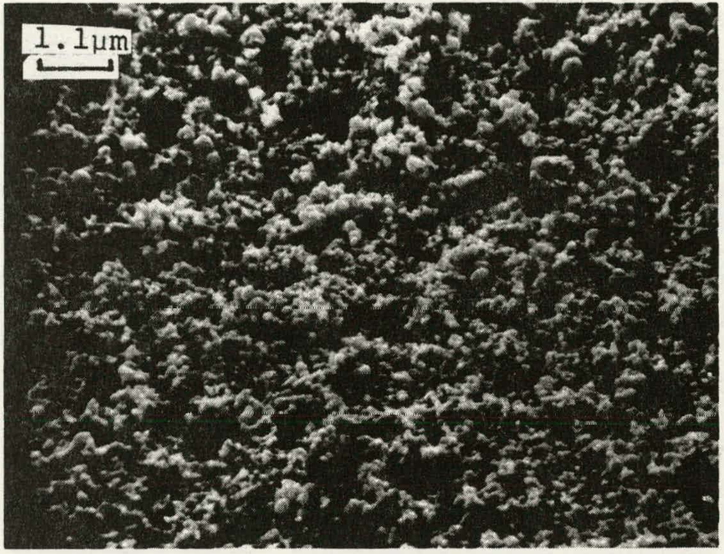

Figure 29 SEM micrograph at 1800x of F7 copper fluorocarbon paste fired at 600^{O}C by the two step process.

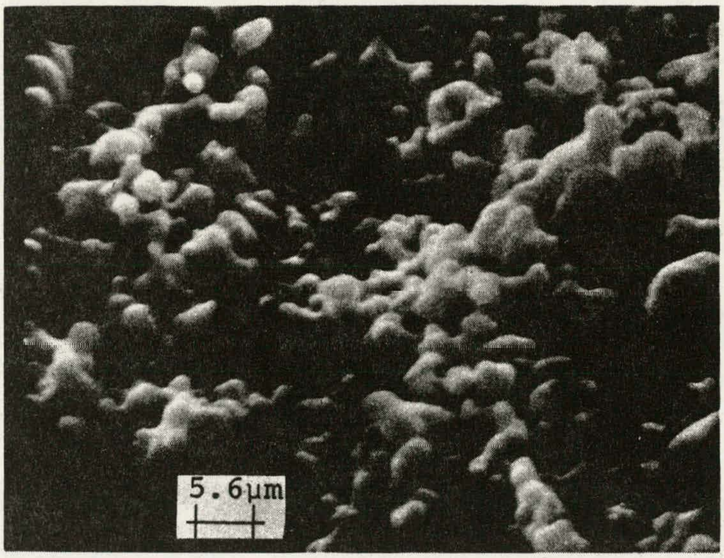

Figure 30 Same as above except 9000x. Note lack of sintering as shown by small particle size and absence of contiguous grain aggregates.

a) the amount of powder that could be accommodated by a given quantity of vehicle (metal content) and b) the apparent "fluffiness" of the metal powder. Both a) and b) are attributable to smaller than usual particle diameters. A total of 99 different paste formulations were manufactured by the previous subcontractor including many attempts to reproduce S071, S079 and S080 which represented the best solar cell electrodes made to date (previous contract #955164)[6]. It was deemed appropriate to start a new numbering system for pastes manufactured by the new subcontractor, beginning with F1 (which would have been S100 under the old scheme). The first fluorocarbon ink in this series was F4 utilizing 0.7 wt% fluorocarbon powder with the results described above. Pastes were produced with various copper powders including copper flake (see Section 4.1), without a marked improvement. Fluorocarbon content was varied from 0.7 wt% (F4) to 2.1 wt% (F11) with the medium range (1.0 to 1.2 wt%) yielding the best results.

An extensive analysis was undertaken by Dr. Joseph Parker, of the possible chemical reactions of the paste constituents throughout the thermal history of the screened electrodes. A set of simple equations was written and the thermochemical analysis was done, based upon heats of reaction from published or derived heats of formation, for the various compounds. The numerical value and algebraic signs of the heats of formation indicate the likelihood that certain reactions should be emphasized or reduced in extent. This suggests a change in composition. Subsequently it was desirable to verify these clues by direct experimentation and further physical analysis with differential thermal analysis (DTA) and thermal gravimetric analysis (TGA) (see Section 7.0).

The above analysis showed that it would be desirable to provide an additional liquid medium, whose function was to promote contact between the copper powder grains and the freshly exposed silicon surface, during the scavenging activity of the fluorine from the fluorocarbon source. Earlier work with silver fluoride had shown that the fluorine scavenging activity takes place very rapidly ($\sim$ 1 sec), while the silver fluoride salt is in a liquid form. The reaction products, solid silver metal and gaseous silicon tetrafluoride, as well as water, drive the reversible reaction on one direction through the mass action law, and the contact between silver and silicon is a consequence of the reaction site. Contact between the copper grains and the silver fluoride is promoted by the liquid lead (liquid phase sintering medium), during the longer term of the sintering step. In the case of the fluorocarbon decomposition the reaction proceeds without the presence of sufficient liquid phase, making the contact between copper and freshly exposed silicon less probable. This is because the amount of fluorocarbon has to be kept low due to other potential spoiler reactions and due to the low density of fluorocarbon making it a nonideal transport medium. An additional liquid medium, lead acetate, melting point 280°C, was therefore chosen to transport copper grains to freshly exposed silicon sites. Liquid sintering of the copper matrix is still thought to be a solution growth phenomenon accomplished by the liquid metal lead.

The first paste containing lead acetate and fluorocarbon powder was F13 copper paste. The composition of this paste is given in Table IV below.

TABLE IV

COMPOSITION OF PASTE F13

Material	Source	Amount (wt%)
Vehicle	Dupont	34.1
Fluorocarbon	Dupont	1.1
Aluminum-Silicon eutectic	Alfa-Ventron	1.1
Lead Acetate	Baker	2.3
Lead Metal	MCB	4.6
Copper metal	Colonial	56.9

The paste was screened as a test pattern as well as solid electrode. During firing at a temperature of 556°C several variations of gas ambients were tried. The normal nitrogen-hydrogen two step firing gave reasonably good adherence, although some pulloff was observed in the Scotch tape test. The two step firing process was described previously[7], but will be repeated in Table V for the sake of completeness.

TABLE V
TWO STEP FIRING PROCESS

Time (minutes)	Gas	Wafer Temperature and Location
10	Nitrogen	∿25°C (Room temperature) outside furnace
3	Nitrogen	80°C - 150°C(dry) at furnace entrance
5	Nitrogen	at temperature (∿550°C) in furnace
8	Hydrogen	at temperature (∿550°C) in furnace
2	Hydrogen	550°C → 25°C(slow cool) to furnace exit
5	Hydrogen	Cool outside furnace
5	Nitrogen	Cool outside furnace

Best results were obtained in a run in which the sintering took place in nitrogen and hydrogen was used only during the cooling phase. A Scotch tape test (See Section 4.3) performed on the electrode from this run gave good results with virtually no pulloff.

Figure 24 and 25 show SEM micrographs of F13 electrodes fired at 550°C by the hydrogen cool process, with indicated magnifications. It can be seen that the degree of sintering is inadequate, and there is some evidence of oxidation in Figure 25. The two conditions may be related in that the lack of sintering may be due to lack of wetting by the liquid phase sintering medium (lead), since hydrogen is introduced only during cool-down. Figures 33 and 34 show SEM micrographs taken of substrates under F13 electrodes (525°C) after electrodes were removed mechanically. The white beads covering

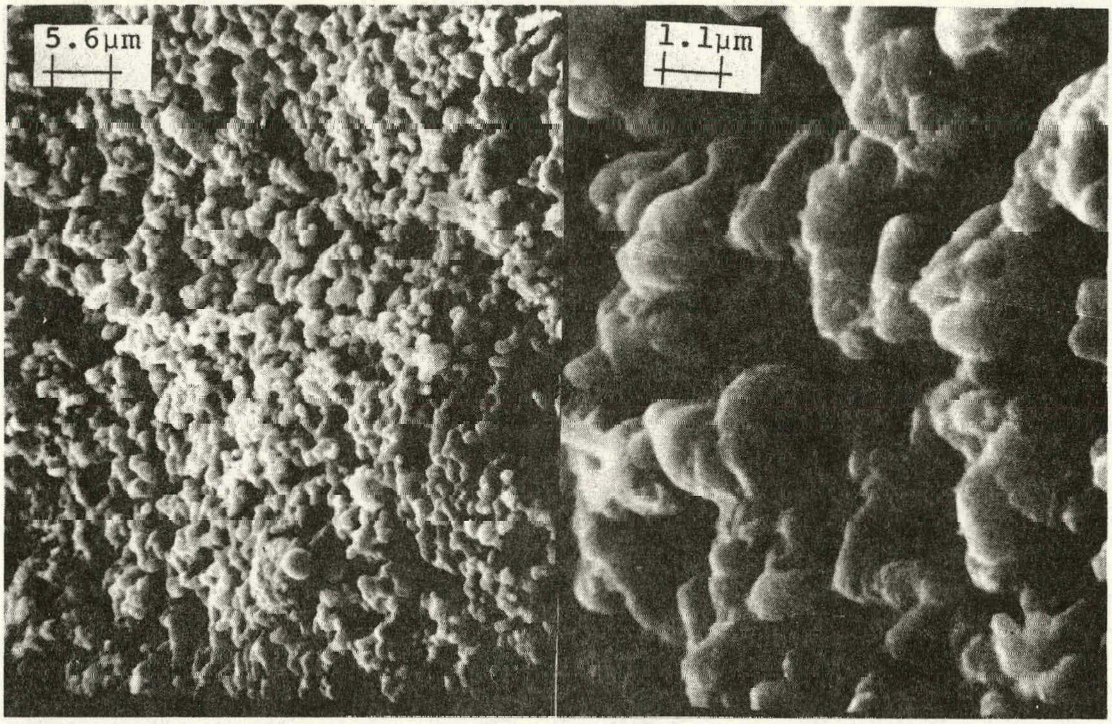

Figure 31 1800x Figure 32 9000x
SEM micrographs of F13, copper fluorocarbon electrode.

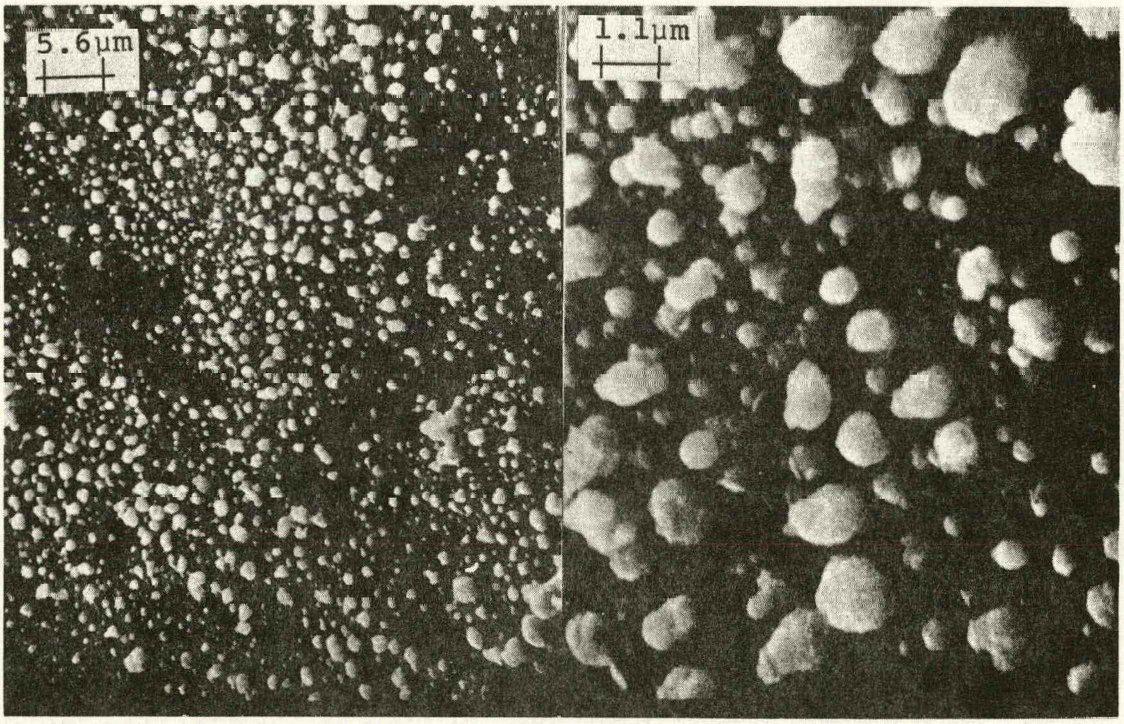

Figure 33 1800x Figure 34 9000x
SEM micrographs of substrates under above electrodes.

the surface appear to be dielectric in nature judging from the presumed charging effects of Figure 34. Therefore we believe the material to have resulted from the lead acetate and expect it to be lead oxide.

5.2 Solar Cell Experiments

Screening experiment with F13, 16, 17 and F20 paste was made on 2 X 2 cm phosphorus diffused, laser scribed and broken solar cell material. The back contact only was provided with a screened electrode of the above pastes. The specimens were fired by the normal two step procedure at 575°C and 625°C. The results were variable with most specimens failing the Scotch tape test. One device (not tape tested) was transmitted to the Jet Propulsion Lab for application of front contacts (Ti-Pd-Ag) and measurement.

The IV curve is shown in Figure 35. The curve is characteristic of poor series and shunt resistance. An attempt to etch the cell edge to increase shunt resistance resulted in some improvement in open circuit voltage but simultaneously increased the series resistance, presumably as the cell mask (tape) was removed. While the device electrode (F16 screened paste) is far from optimized, it is an indication that the fluorocarbon containing paste is viable for solar cell electrodes. The uncoated solar cell had efficiency of 7.0% initially (corresponding to 9.6% AM1 with AR coating).

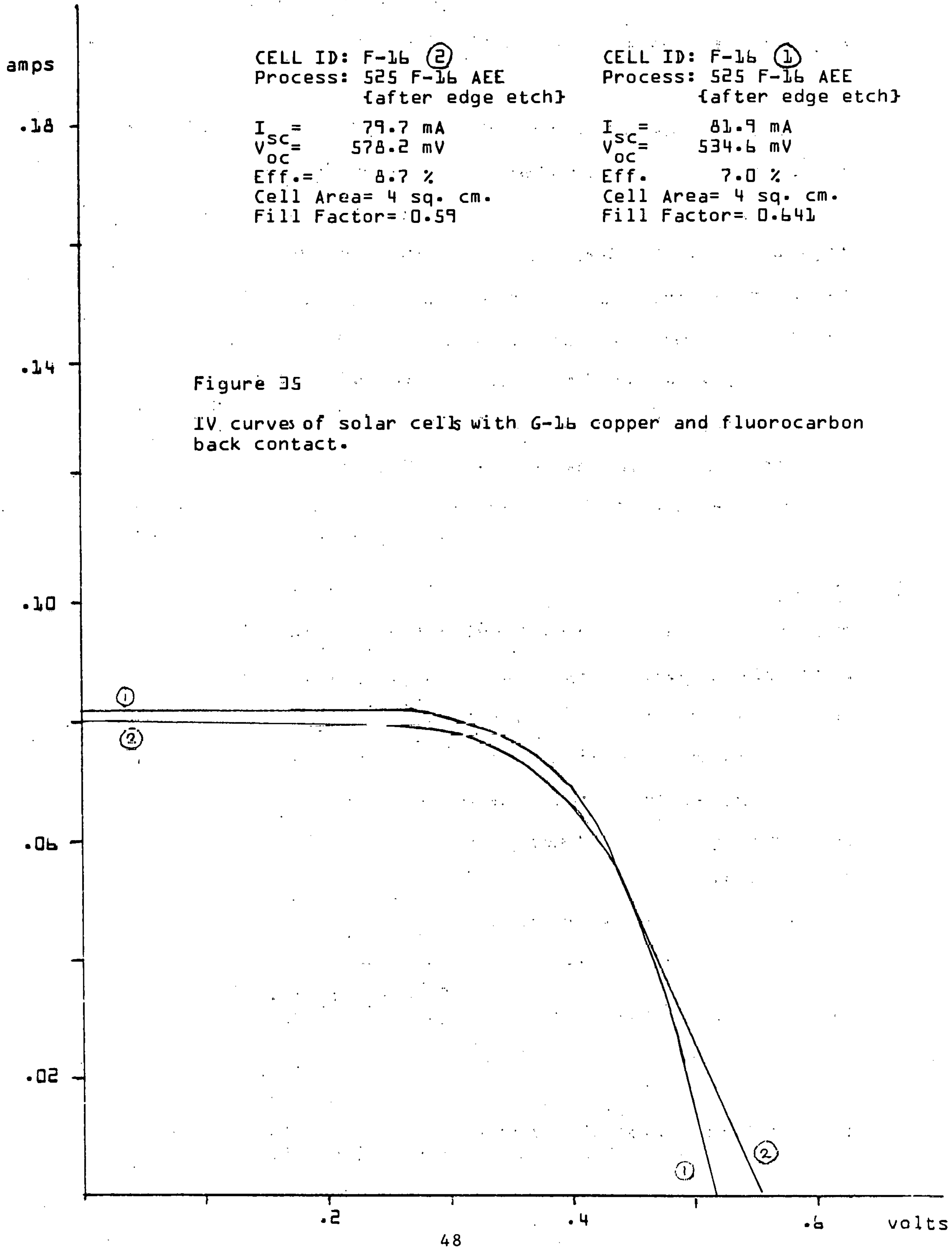

CELL ID: F-16 ②
Process: 525 F-16 AEE
{after edge etch}
I_{sc}= 79.7 mA
V_{oc}= 578.2 mV
Eff.= 8.7 %
Cell Area= 4 sq. cm.
Fill Factor= 0.59

CELL ID: F-16 ①
Process: 525 F-16 AEE
{after edge etch}
I_{sc}= 81.9 mA
V_{oc}= 534.6 mV
Eff. 7.0 %
Cell Area= 4 sq. cm.
Fill Factor= 0.641

Figure 35

IV curves of solar cells with G-16 copper and fluorocarbon back contact.

6.0 FRONT CONTACT CONSIDERATIONS

The theory of ohmic contacts was reviewed particularly with regard to the metal semiconductor contact parameters and tunneling equations. Some errors were discovered in the literature (see Appendix Ref. #6) which were corrected on the basis of the original references (for example, Ref. #18, ibid). A paper was prepared including the findings. This was presented at the 4th E.C. Photovoltaic Solar Energy Conference, May 1982 in Stresa, Italy by courtesy of Dr. William Callaghan, since the author was unable to attend for health reasons. A copy of the paper is attached in the appendix.

6.1 Theory

The front contact of modern solar cells is applied to nearly degenerate n type semiconductor surfaces with impurity concentrations from 10^{19} atoms/cm^{-3} to 10^{21} atoms/cm^{-3} with phosphorous being the donor conventionally in use. Due to the high surface concentration and resulting high conductivity in accordance with

(1) $\sigma = Nq\mu$

where σ = conductivity $(\Omega \text{ cm})^{-1}$

N = carrier concentration, cm^{-3}

q = electronic charge, coulombs

mobility, cm^2/V - sec

it is relatively simple to provide a good ohmic contact to the front surface of solar cells. This results from the fact that the electron tunneling probability is a function of the carrier concentration on both sides of the interface. When a metal coats the surface of a semiconductor, the depletion width within the semiconductor shrinks as a function of carrier concentration, thereby enhancing the tunneling probability. An enhanced tunneling probability provides for ready carrier flow through the barrier constituted by the contact potential between contact metal and semiconductor surface.

The depletion width, W, can be calculated from

(2) $$W = \sqrt{\frac{2\varepsilon_s (V_R + V_D - \frac{kT}{q})}{qN_{D.A}}} \text{ cm}$$ Ref 7

where ε_s = permittivity of the semiconductor $1.06 \cdot 10^{-12}$ F/cm

q = electronic charge, $1.6 \cdot 10^{-19}$ Coulomb

N_D = donor concentrations, $1 \cdot 10^{20}$ cm^{-3}

N_A = acceptor concentration, $5 \cdot 10^{19}$ cm^{-3}

V_R = applied bias voltage, $V_R = 0$

(3) V_D = $\phi_B - \phi_n$ = contact potential

ϕ_{BN} = copper - semiconductor barrier = 0.69eV Ref 8

ϕ_{BP} = 0.46eV Ref 8

(4) ϕ_n = $Ec - E_F$ = 0.0326eV

ϕ_p = $E_F - E_V$ = 0.0452eV

(5) E_c = Conduction band edge potential, eV

E_F = Fermi energy, eV

k = Boltzmann constant J/°K

T = Absolute Temperature °K

The depletion width of the front contact is

$$W = 29.5\ \text{Å}$$

in the silicon.
The maximum field $_m$ is given by

$$(6)\quad \varepsilon_m = \sqrt{\frac{2qN_{D,A}}{\varepsilon_s}\left(V_R + V_D - \frac{kT}{q}\right)} = 4.38\cdot 10^6\ \text{V/cm} \qquad \text{Ref 7}$$

The contact resistance can be calculated from the tunneling conductance

$$(7)\quad R_c = G_o^{-1} = \frac{W}{\sqrt{2m^*\phi}}\left(\frac{h}{q}\right)^2 \exp \frac{4\pi W}{h}\sqrt{2m^*\phi} \qquad \text{Ref 9}$$

$$(8)\quad = 3.16\cdot 10^{-11}\ \frac{\text{Å}}{\sqrt{m^*/m\,\phi}} \exp 1.035 W_{\text{Å}} \sqrt{m^*/m\,\phi}$$

where h = Planck's constant
$(m^*/m)_e$ = 0.1905 the effective electronic mass in the <100> direction

(9) $(m^*/m)_h$ = 0.16 the effective hole mass in the <100> direction
ϕ = $Eg - \phi B$ = 0.42eV
E_g = Energy gap of silicon = 1.1leV
Germanium = 0.65eV
$W_{\text{Å}}$ = Depletion width in Angstroms

The calculated front contact tunneling resistance is

$$R_c = 1.69\ 10^{-5}\ \Omega\text{cm}^2$$

Since the barrier voltage values vary among workers, and their magnitude affects the argument of the exponent in equations 7, & 8, the calculated contact resistance is subject to wide variations.

Similiarly, the carrier concentration at specific depths and at the front surface is difficult to obtain precisely. The uncertainties in barrier voltage can result in depletion widths varying by a factor of two or more, giving tunneling resistances differing by three orders of magnitude. Figure 36 shows the variation of tunneling resistance as a function of barrier (or depletion) thickness.

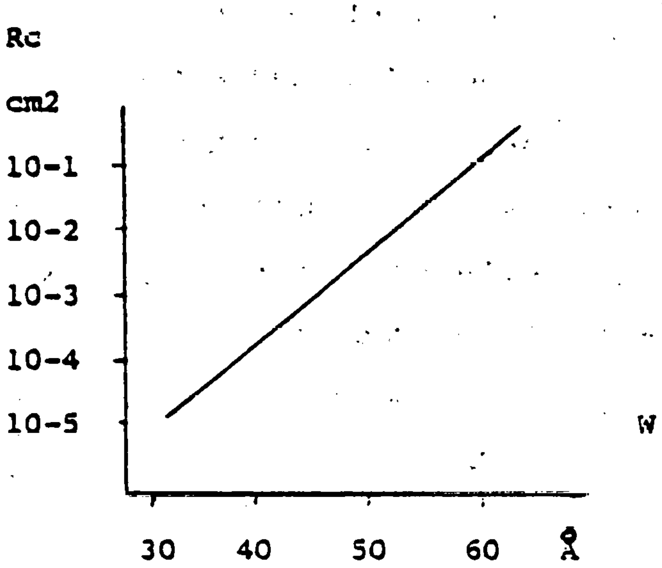

FIG 36 Contact tunneling resistance versus depletion width W

The depletion width for a copper contact to a backsurface field cell ($N_A = 5\cdot10^{19}$ Al/cm^3) is 105 Ångstroms, yielding a calculated tunneling contact resistance of 1.14 $\cdot$ 10^7 Ωcm^2.

The energy band relationships for a copper contact on a silicon front surface doped with $1 \cdot 10^{20}$ phosphorus atoms/cm^3 are shown in Figure 37 using the values calculated above. For the sake of completeness an energy band diagram is included in Figure 38 depicting the back contact relationships for a BSF cell, or a copper contact containing eutectic aluminum-germanium (S080) a hetero epitaxial situation exists, leading to a smaller band gap on the semiconductor side of the contact (E_G (germanium) = 0.65eV).

For the case of a germanium-aluminum contact alloy on the cell backsurface, the redeposition of aluminum doped germanium on the silicon leads to a narrower depletion width of 23.2 Ångstroms due to a higher carrier concentration (N_A = $1.3 \cdot 10^{20}$ Al.cm^3) and smaller barrier height of 0.42 eV. The effective mass of the hole is also considerably smaller in germanium ($\frac{m^*}{m}$ = 0.042). This leads to a tunneling resistance of $7.5 \cdot 10^{-8}$ ohm-cm.

When the semiconductor surface has a higher resistivity, it may be necessary to make special provisions in applying the ohmic contact by utilizing a technique to dope the surface of the semiconductor under the electrode metal. When firing temperatures are sufficiently high($\gtrsim$ 800°C) this may be done by including an elemental donor impurity in the metal and allowing it to diffuse into the semiconductor during the firing step, by solid state diffusion. Since only the surface needs to be doped, the donor atom must become a substitutional impurity in the silicon lattice within a few

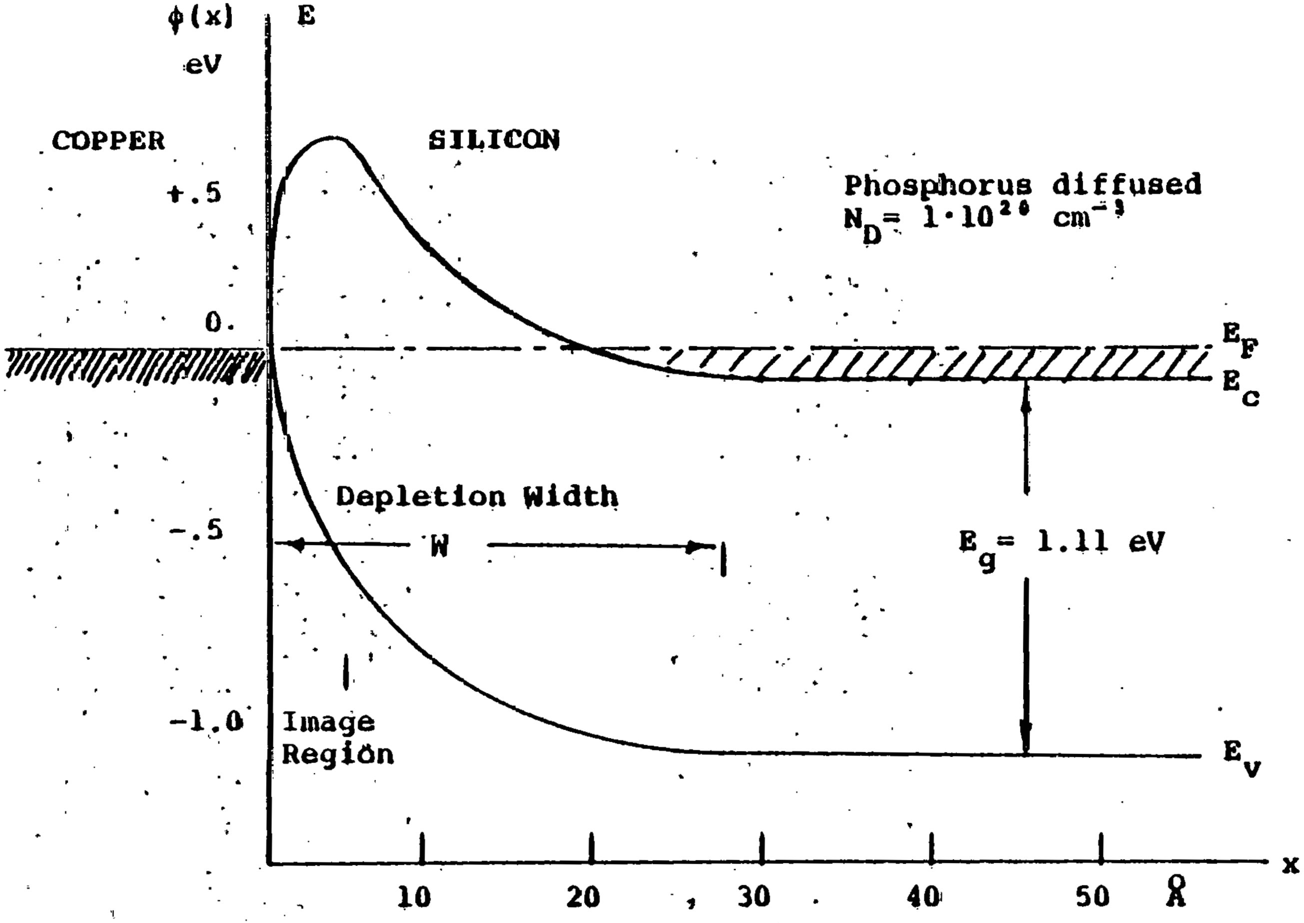

Figure 37 Energy level diagram of copper contact to front of silicon solar cell.

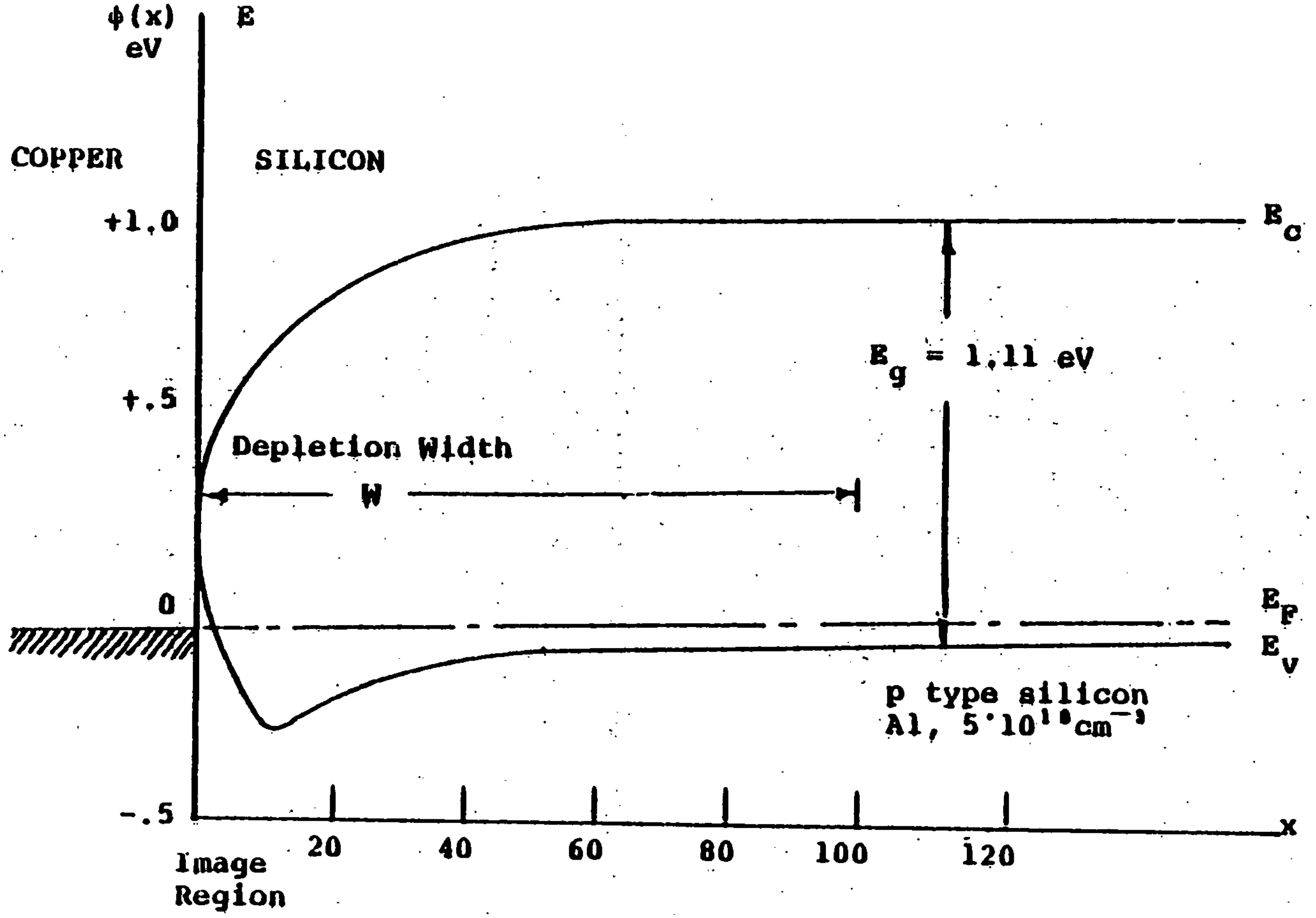

Figure 36 Energy level diagram of aluminum alloy regrowth back contact to solar cell.

lattice spaces of the surface. A brief firing period will usually suffice.

At very low temperature ($\tilde{<}$ 600°C) it may be difficult to obtain a sufficient surface concentration of dopant atoms by diffusion and therefore a different technique is employed. A eutectic alloy of dopant and semiconductor material is made a part of the electrode paste with the object of getting some of the eutectic to bridge semiconductor and metal. During the firing step the eutectic melts, dissolving more silicon. As the temperature is lowered again the dissolved silicon precipitates on the surface, retaining donor solid solubility concentrations, and thereby facilitating ohmic contact. Since the solid solubility of some elements in silicon is small, the use of this method is beneficial only when the front surface donor concentration is less than the donor solid solubility.

6.2 Experiments

Two pastes were prepared for the front contact experiment. S071 is an undoped copper paste, which should provide the desired contact on phosphorus diffused solar cells, by virtue of the above arguments. A paste was also prepared to address the second possibility, providing an epitaxial crystalline layer, doped with antimony. This paste was fabricated by producing an eutectic alloy of antimony-germanium, reducing the resulting ingot to powder, and adding the material to the paste (5 wt.%).

A number of contact resistance measurements were made utilizing copper paste F31 (composition copper 64.82 wt.% lead 6.48 wt.% silver fluoride 0.70 wt.% without eutectic addition) and F32 (similar to F31 plus 3.1 wt.% aluminum-silicon eutectic). Prints were made with the linear contact resistance array previously reported, fired in carbon monoxide at 550°C, 600°C. 650°C. While there was some data scatter, F32 with eutectic additions gave the lowest contact resistance at the higher temperatures ($5 \cdot 10^{-3}$ ohm cm^2 at 650°C).

A measurement on a 700Å silicon nitride coated phosphorus diffused wafer gave a contact resistance of $1 \cdot 10^{-2}$ ohm cm^2, utilizing F25, a copper paste with 5 wt.% AgF for $Si_3 N_4$ layer penetration. Subsequent analysis showed that the use of the linear array without limiting the lateral current flux excursions can lead to measurement errors. This can be avoided by cutting a bar of width equal to the outer current electrodes.

Additional measurements carried out by Dr. William Taylor, Photowatt, Intl., suggested that the PN junctions of these wafers were perforated, or shunted by the F25 electroding process. New screens were designed and fabricated in order to allow utilization of convenient and economical 2cm x 2cm solar cell blanks. A design was made for a universal test pattern and solar cell front and back electrodes. These could be used both for basic ink parameter measurements and solar cell contact experimentation. The test pattern allows measurement of contact resistance, line resistance substrate resistivity, optical line resolution and electrical line resolution and is shown in Figure 39. The linear pattern at the top facilitates a measurement allowing the calculation of contact resistance (in Ωcm^2), simultaneously giving the resistivity of the silicon substrate. The large squares (2.5mm x 2.5mm), at the extremes of the linear array, provide the current electrodes in the measurement, while the small series of rectangles provide the voltage sources in the array. This portion of the design had been used previously[5]. A long line at the periphery of the pattern was used for measurement of the electrode resistance, from which the resistivity can be derived by.

$$(1) \qquad \rho = R \frac{tw}{\ell} \Omega cm$$

where $\rho \equiv$ electrode resistivity Ωcm
$R \equiv$ measured resistance,
$t \equiv$ electrode thickness, Ωcm
$w \equiv$ electrode width, cm
$\ell \equiv$ electrode length, cm

The interwoven pattern under the contact resistance array serves to determine line definition and the degree of measurable crossover or bridging, based upon a resistance measurement. It will be noted that two sets of line pairs are provided, one that is coarse (.009 inches line width and spacing) and one that is fine, .004 inches line width and spacing (See Figure 21, lower and upper portion, respectively). It has been noted that screening in a direction perpendicular to a line tends to reduce line resolution.

Based upon these designs, frames were ordered both for #325 mesh screens and #230 mesh screens. The #325 mesh screens were chosen initially to allow ultimate resolution, but proved to be too fine to allow sufficiently thick deposits. The #230 mesh screens were adequate.

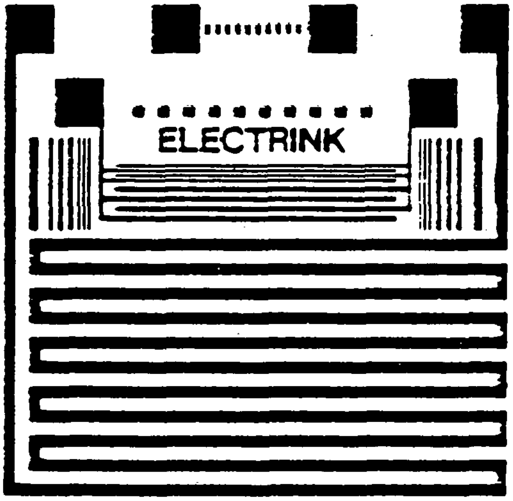

3X Actual Size

Figure 39 Photograph of screen pattern, with contact resistance, line resistance optical and electrical resolution test.

7.0 THEORETICAL CONSIDERATIONS OF REACTIONS

The firing process involves the heating in special atmospheres, and at elevated temperatures, of a multi-component metal powder ink. These conditions favor the occurrence of numerous chemical reactions.

Such reactions are thought to be the cause of observed poor reproducibility of some performance characteristics of the ink despite care taken to control known parameters. One means for gaining an insight to the possible reactions is the analysis of reasonable combinations or disintegrations of materials present and using principles of chemical thermodynamics and kinetics, to evaluate (even if only qualitatively) the probability that such reactions actually take place.

The heat of a reaction is a readily obtained measure of the tendency of a reaction to proceed. Reactions which produce a great deal of heat are much more likely to occur than those which require the absorption of much heat. The development of the enthalpy change of reaction heat arises from the definition of the enthalpy change of a process viz.

$$\Delta H = \Delta E + \Delta(pV),$$

and the first law of thermodynamics,

$$\Delta E = Q - W = \Delta H - \Delta(pV).$$

In these equations p is the pressure, V is the volume, and ΔE is the total energy change for a system change in which an amount of heat, Q, is added to the system and an amount of work W, is removed from the system. In the case of the reactions of interest the process is one which takes place at constant pressure and involves only volume change work. This leads to:

$$\Delta H_r = Q_p - W + \Delta(pV) = Q_p$$

Which is the enthalpy change or "heat of reaction" for a constant pressure process.

Let us now consider the constant pressure combustion of methane where

$$CH_4 + 2O_2 \rightleftarrows CO_2 + 2H_2O$$

The enthalpy change for this reaction is:

$$\Delta H_r = (H_{CO_2} + 2H_{H_2O}) - (H_{CH_4} + 2H_{O_2})$$

Where the subscripted values are the enthalpies of the indicated molecules. This is simply the difference between the initial and final system enthalpies. The above relation may also be written as the enthalpy equation,

$$H_{CH_4} + 2H_{O_2} = H_{CO_2} + 2H_{H_2O} - \Delta H_r$$

Conservation of matter concepts allow us to use molecular heats of formation for the subscripted enthalpies because elemental enthalpies cancel (and are given a value of zero when they appear in a reaction) when enthalpy changes are computed. Tables of heats of formation are readily found (Refs. 10, 11 & 12) and this fact makes the rough calculation of heats of reaction a fairly simple matter in most cases. The heats of formation for the gaseous molecules of this example are:

$$\Delta H_{CH_4} = -17.4, \ \Delta H_{O_2} = 0.0, \ \Delta H_{CO_2} = -94.1, \ \Delta H_{H_2O} = -57.8$$

These values are for the 25°C formation at one atmosphere of the gaseous molecules (from elements) expressed in kilocalories per gram mole. The reaction heat for the combustion of one mole of methane under these conditions is therefore;

$\Delta H_r = -94.1 + 2(-57.8)-(-17.9)-2(0.0)= -91.8$ kcal/mole

The reaction represented here is exothermic since Q_p $(=\Delta H_r)$, the heat put into the system, is negative. The corresponding enthalpy equation is:

$$CH_4 + 2O_2 = CO_2 + 2H_2O + 91.8 \text{ kcal/mole}$$

Here the molecular formulas are used to represent the heats of formation to simplify the notation.

The enthalpy change shown is due to the reaction when carried out at room termperature. Since the state of a system is independent of the process path used to reach it, we may derive a correction expression for enthalpy change in a reaction which takes place at a temperature, T_1 other than at room temperature, T_0.

The room temperature enthalpy of reaction plus the heat needed to bring the products to temperature T_1 is:

$$\Delta H_a = H_r^{T_0} + \int_{T_0}^{T_1} C_p^P \, dT$$

Where C_p^P represents the heat capacity (at constant pressure) of the products. This corrected enthalpy value, ΔH_a, must be the same as the sum of the heat required to bring the reactants to temperature, T_1, and the heat of reaction at T_1, which is:

$$\Delta H_b = H_r^{T_1} + \int_{T_0}^{T_1} C_p^R \, dT$$

Where C_p^P represents the heat capacity of the reactants. When these are equated ($H_a = H_b$) the desired value for the enthalpy of reaction at T_1 is obtained by rearrangement and combination of terms. Thus,

$$\Delta H_r^T = \Delta H_r^T + \int_{T_0}^{T_1} (C_p^P - C_p^R)$$

The correction term in the above equation involves heat capacities at constant pressure which are, in general, functions of temperature.

It was implied earlier that the larger the exothermic heat, the greater the tendency for the reaction, as written, to proceed from left to right. We may infer from the discussion of the heat of reaction that strongly endothermic reactions tend to proceed from right to left.

Two factors which may modify or even override the above considerations are: 1. Reaction activation energy and 2. Mass action effects. Values for the former are obtained from investigations of the kinetics of the reaction. These will not be detailed here. The latter are based on the general observation that reaction rates increase with an increase in the amount or concentration of reactants. When a reaction produces a gas and a condensed molecule so that the gas tends to separate from the other products, the reverse or right-to-left reaction is inhibited by the loss of the gas. This represents a net increase in the left-to-right reaction.

Because activation energy is often an influential factor in the observed vigor of a particular reaction scheme, available indications of actual reaction or non-reaction take precedence over other considerations. The relation between the heat of reaction, ΔH_r and the activation energy, ΔE_a, is shown in Figure 40.

The materials and firing conditions for the current ink formulations suggest the following four categories of reactions:

I Fluorocarbon formulation, Nitrogen atmosphere
II Fluorocarbon formulation, Hydrogen atmosphere
III Silver fluoride, Nitrogen atmosphere
IV Silver fluoride, Hydrogen atmosphere

In addition to those already indicated, materials of interest are; copper, lead, silicon, silver, and their hydrides, oxides, fluorides, and nitrides. Heats of formation for some of these materials are listed in Table VI.

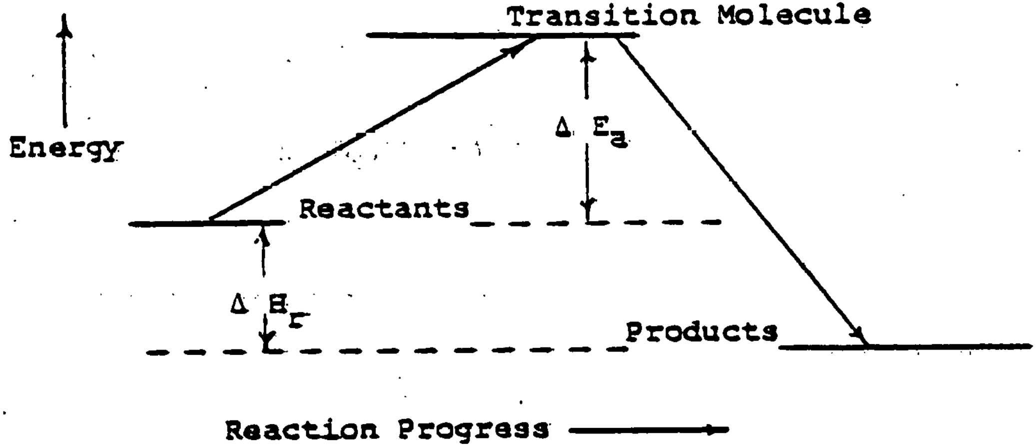

ΔH_r = Heat of Reaction
ΔE_a = Activation Energy

Figure 40 The Relation Between Heat of Reaction and Reaction Activation Energy

TABLE VI

SELECTED HEATS OF FORMATION

Molecule or Atom	State	ΔH_f 25°C Kcal/mole	Molecule or Atom	State	ΔH_f 25°C Kcal/mole
Si	s	0.0	O_2	g	0.0
SiO_2	s	-205.4	O	g	59.2
SiF_4	g	-370.0	CO	g	-26.4
Si_3N_4	s	-179.3	CO_2	g	-94.1
SiH_4	g	-14.8	CH	g	-17.9
SiC	s	-26.7	C_2F_4	g	-173.8
			C_2H_4F	g	-309.9
Ag	s	0.0			
AgF	s	-48.5	Cu	s	0.0
			CuO	s	-37.1
F	g	0.0	CuF_2	s	-136.9
F_2	g	18.3	$CuAc_2$	s	-213.2
F_2O	g	5.5			
			Pb	s	0.0
N_2	g	0.0	PbO	s	-52.2
N	g	85.6	PbO_2	s	-66.1
NF_3	g	-11.0	PbF_3	s	-158.5
NH_4F	s	-111.6	PbF_4	s	-222.3
			$PbAc_2$	s	-230.5
H_2	g	0.0	$PbAc_2 \cdot 3H_2O$	s	-443.1
H	g				
H_2O	g	-57.8	AlF_3	s	311.0
HF	g	-64.2			

Enthalpy equations for selected category I reactions are:

1. C_2F_4 (g)+SiO_2 (s)=SiF_4 (g)+2CO(g) + 43.6
2. $3C_2F_4$(g)+Si_3N_4(s)=$3SiF_4$(g)+6C(s)+2N (g)+ 136.4
3. C_2F_4(g)+3Si(s)=SiF_4(g)=2SiC(s)+ 249.6
4. C_2F_4(g)+Si(s)=SiF_4(g)+2C(s)+ 196.2
5. C_2F_4(g)+2PbO(s)=$2PbF_2$(s)+2CO(g)+ 91.6
6. C_2F_4(g)+2CuO(s)=$2CuF_2$(s)+2CO(g)+ 58.6
7. $2N_2$ (g)+3Si(s)=Si_3N_4(s)+ 179.3

This selection of "reasonable combinations" is a first pass rather than a complete list. Further analysis should eliminate some listed equations and add some new ones.
It should be noted that the specification of the state of a molecule is important in the choice of a value for its heat of formation. In these (and following) equations, the state, s=solid, g=gas, parenthetically follows the molecular symbol. The above reaction heats (except for the nitrogen-silicon reaction) are for one mole of tetrafluoroethylene.
Although the reaction postulated for the formation of SiC (#3) seems highly favored by a large exotherm and by mass action, it is not observed and therefore equation #3 must be discounted. On the other hand, it is observed that Si is quite likely to react with strongly electronegative atoms so equations #4 and #7 seem reasonable in view of their appreciable exothermic heats.

The rejection of equation #3 is more readily seen when it is viewed as the sum of two equations, namely, equation #4 and (two times) equation #8 below.

8. $Si(s)+C(s)=SiC(s)+26.7$

This reaction has neither a large exotherm nor mass action to favor it.

Reaction #1, which removes SiO_2 from the substrate surface is the intended purpose of the fluorocarbon powder in the ink formulation. The occurrence of this reaction is supported by some experimental work [12].

None of the other reactions indicated above is particularly beneficial to the ink firing process. Equation #7 suggests the possibility of reaction between nitrogen and fresh silicon surfaces and thereby implies that air-exposed silicon surfaces might be at least partly covered by nitride molecules.

Equations #2 and #4 are strongly favored and specify carbon deposition at the silicon surface due to fluorocarbon reactions. Relatively poor conductivity and adhesion are expected at such sites so reducing the amount of fluorocarbon in formulations should improve ink results.

There are relatively large amounts of copper in these ink formulations so a small amount of copper fluoride formation from equation #6 should cause little trouble but there are only small amounts of formulation lead so equation #5 which converts lead to its fluoride might substantially reduce the proportion of metallic lead and this would suppress the leaddependent process of liquid phase sintering. Poor sintering had been noted in fired inks so new formulations appeared to provide improved sintering and adhesion.

It is known that there were air leaks into the kiln during earlier experimental ink firings. Some of the likely oxygen reactions are:

9. $Si(s)+O_2(g)=SiO_2(s)+ 205.4$

10. $Cu(s)= 1/2O_2(g)=CuO(s)+ 37.1$

11. $Pb(s)+ 1/2O_2(g)=PbO(s)+ 52.2$

Depending upon where in the process such reactions occurred, the oxides formed could cause poor sintering, poor adhesion, and poor solderability of the fired inks. Appropriate improvements have been made in the process and equipment so that problems due to oxide formation have been all but eliminated.

In the case of category III reactions, where silver fluoride is a constituent of the ink formulation and nitrogen is the firing atmosphere, the equations for selected reactions are:

12. $AgF(s)=Ag(s)+ F_2(g)- 48.5$

13. $SiO_2(s)+4AgF(s)=SiF_4(g)+4Ag(s)+O_2(g)- 29.4$

14. $Si(s)+4AgF(s)=SiF_4(g)+4Ag(s)+ 176.0$

15. $Si_3N_4(s)+12AgF(s)=3SiF_4(g)+12Ag(s)+2N_2(g)+ 348.7$

16. $Cu(s)+2AgF(s)=CuF_2(s)+2Ag(s)+ 29.9$

17. $Pb(s)+1AgF(s)=PbF_2(s)+Ag(s)+ 61.5$

18. $CuO(s)+2AgF(s)=CuF_2(s)+ 1/2O_2(g)+2Ag(s)- 7.2$

19. $PbO(s)+2AgF(s)=PbF_2(s)+2Ag(s)+ 1/2O_2(g)+ 9.3$

Equations #12 and #13 have been previously proposed[13].

Both are endothermic but are aided by mass action. Observation indicates that #12 does not take place to any extent in our firing range of 550°C to 650°C [11], however, equation #13 has been shown to proceed [12]. Equation #14 has been observed to take place at an extremely rapid rate [5,6]. Equation #15 appears to be a promising answer to problems arising from silicon nitride formation due to equation #7 since it is strongly favored by exotherm and mass action, and deposits metallic silver rather than carbon which is the residue of fluorocarbon action on silicon nitride (eq. #2). As in the case of the fluorocarbon reactions, reactions #16 through #19, which produce fluorides of lead and copper are not beneficial to the electrode process. Indeed, the loss of metallic lead through fluoride formation might be quite detrimental. Reductions of silver fluoride content in ink formulations seem to have resulted in improved adhesion and sintering.

Equations for some reactions which might occur during the hydrogen atmosphere portion of the firing, i.e. categories II and IV, are as follows:

20. $CuO(s)+H_2(g)=Cu(s)+H_2O+ 20.7$
21. $PbO(s)+H_2(g)=Pb(s)+H_2O(g)+ 5.6$
22. $CuF_2(s)+H_2(g)=Cu(s)+2HF(g)+ 1.5$
23. $PbF_2(s)+H_2(g)=Pb(s)+2HF(g)- 30.1$
24. $SiO_2(s)+4H_2(g)+SiH_4(g)+2H_2O(g)- 75.0$
25. $O_2(g)+2H_2(g)=2H_2O(g)+ 115.6$
26. $Si(s)+2H_2(g)=SiH_4(g)+ 14.8$

27. $C(s)+2H_2(g)=CH_4(g)+ 17.9$

28. $C_2F_4(g)+H_2(g)=C_2H_2F_4(g)+ 136.1$

29. $AgF(s)+ 1/2H_2(g)=Ag(s)+HF(g)+ 15.7$

The reaction heats here are in kilocalories for one gram mole of the first molecule in the equation.

Equations #20 through #23 represent the restoration (by reduction) or metallic copper and lead from their oxides and fluorides which formed during the earlier nitrogen atmosphere portion of the firing cycle. Equation #20 is observed (by color change) to take place under conditions of hydrogen firing, but the endothermic reaction of equation #23 probably does not take place, to any appreciable extent, despite its mass action assist.

The above reductions and their reverses (oxidations) could be verified by Thermogravimetric Analysis (TGA) methods. Table VII summarizes the expected TGA results. In these experiments the reverse fluoride reactions would be done in N_2 with excess fluorocarbon polymer powder mixed with the metal powder since the fluorocarbon has been found to convert completely to gaseous products above 550°C or so.

TABLE VII

DATA FOR METALS OXIDATION AND REDUCTION STUDIES

Compound	Color	MW	Metal MW	React. #	Oxide. % Wt. Gain	Redu. % Wt Loss
CuO	Black	79.5	63.6	20	25.0	20.0
PbO	yellow	223.2	207.2	21	7.7	7.2
CuF	white	101.5	63.6	22	59.6	37.3
PbF	colorless	245.2	207.2	23	18.3	15.5

The indirect evidence that reductions of fluoride in ink formulations bring improved bonding and sintering supports the idea that equation #23 does not proceed and that once lead fluoride is formed, it remains in the fired ink.

It is well known that the endothermic reaction of eq. #24 does not take place even at the elevated temperatures of ink firing. Equation #25 has been observed (by moisture condensation) at firing temperatures, but the extent of the equation #26 reaction may be limited because of the instability of many of the silanes.

Equation #26 may be more accurately stated by:

$$nSi+(n+1)H_2 \rightleftarrows Si_nH_{2n+2}$$

Similarly, the reaction of equation #27 could be written,

$$nC+(n+1)H_2 \rightleftarrows C_nH_{2n+2}$$

The heats of formation per mole of carbon (or silicon) hydrides decrease asymptotically with increasing n, as shown in Figure 41.

This indicates that the n=1 compounds would strongly predominate in the composition of a reaction mix.

The classic procedure for the production of silanes using magnesium silicide in H_2 and HCl[16]. results in 40% SiH, 30% Si_2H_6, 15% Si_3H_8, 10% Si_4H_{10} and 5% higher silanes[17]. Non-volatile silicon hydride polymers which include an unsaturated bond have also been prepared[17]. These may arise from,

$$nSi + nH_2 \rightleftarrows (SiH_2)_n$$

Condensed hydride polymers or homologues of silicon (silanes) or carbon (alkanes) deposited on the silicon substrate would be expected to affect adversely the physical and electrical properties of fired inks.

On examination of the reaction enthalpies and mass action effects it appears likely that hydrogen does react, during firing, with residual tetrafluoroethylene (eq. #28) in category II or with silver fluoride (eq. #29) in category IV. The hydrogen atmosphere phase of firing has been associated with frequent random incidents of very poor ink adhesion using inks which previously gave excellent bonding. In some cases, ink samples which were well bonded (but somewhat oxidized) during the nitrogen firing showed no bonding after hydrogen firing. One possible explanation is that bonding sites on the silicon substrate are chemically attacked by the HF generated according to equations #22 and #29 in hydrogen firing.

A reduction of the temperature of the ink sample during hydrogen firing gives an improvement in ink bonding, which

Figure 41 Heats of Formation Versus n for the Alkane Series C_nH_{2n+2}

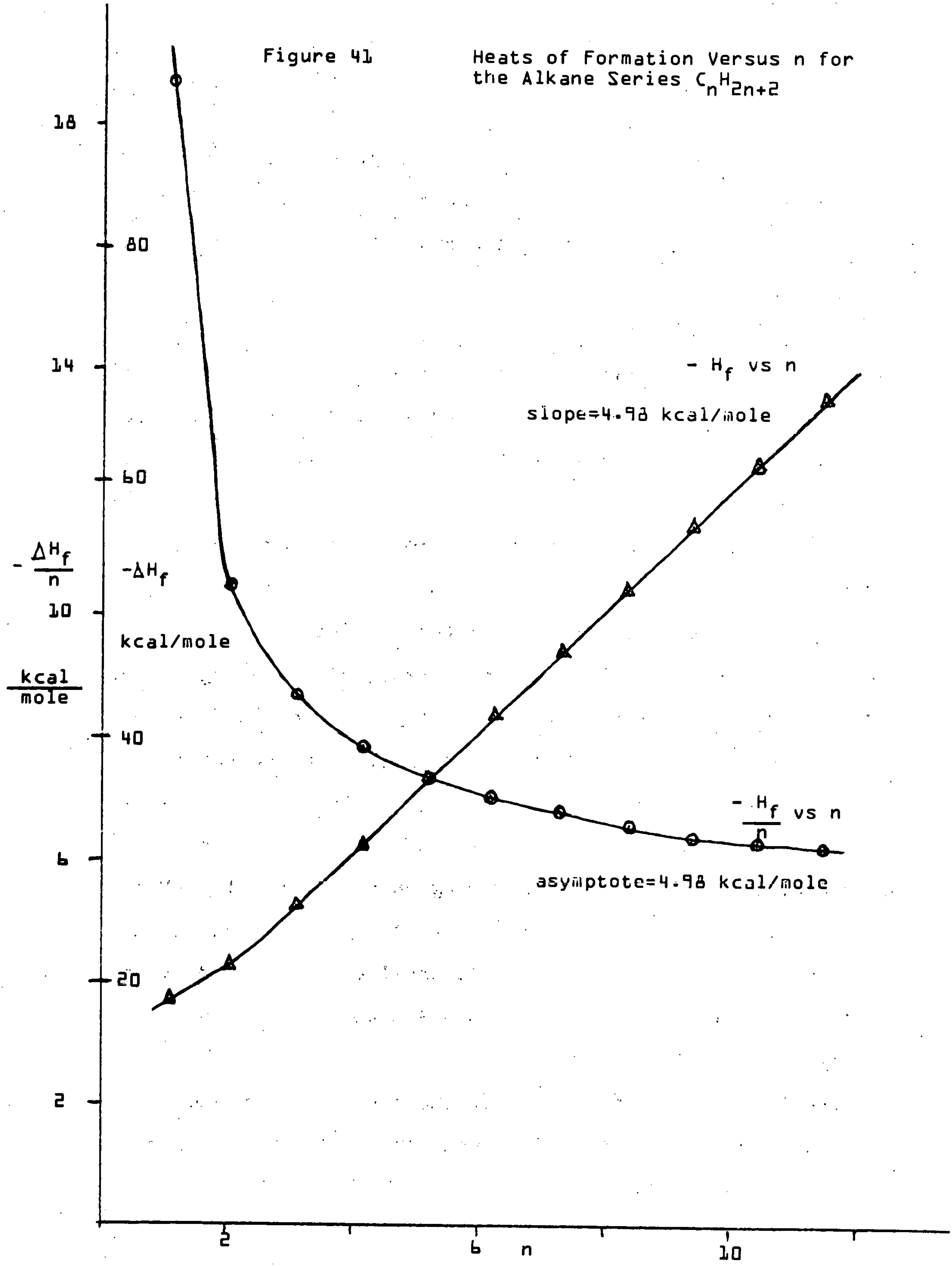

could be attributed to a reduction in the extent of equations #22 and #29.

Another hypothesis is the occupation of dangling electron bonds on silicon surfaces by hydrogen or possibly the displacement of metal atoms by hydrogen (section 8.0). These preliminary applications of simple chemical ideas have pointed to some fruitful directions for experimental work aimed at improvement of ink materials and processes. In particular, progressive fluoride reductions and milder hydrogen treatments, which were suggested by thermochemical and mass action considerations, proved quite beneficial to the mechanical properties of the ink system.

Inconsistency of results still plagues the ink formulations containing fluorocarbon powder, and early studies of ink electrical performance indicate a need for increased knowledge of the chemistry of these ink systems.

To this end, the work of this report should be expanded to include literature searches to unearth more possible reactions and provide needed heat capacities and activation energies. Experimental work making use of TGA and differential thermal analysis (DTA) should be increased and in addition, the simple theoretical tools of chemical kinetics and chemical equilibrium should be applied to the determination of the likely extent of candidate reactions.

8.0 HYDROGEN CONCENTRATION PROFILING

Earlier experiences with hydrogen firing have shown that both silver and copper lose their adhesion to silicon surfaces in hydrogen ambients above a temperature of approximately 380°C. In order to investigate this phenomenon a procedure was sought which would allow determining the hydrogen concentration profile in close proximity to the silicon surface. Professor W.A. Lanford S.U.N.Y., Albany, N.Y., kindly consented to examine a set of "unknown" samples produced in our laboratory utilizing the technique of resonant nuclear reaction profiling. Figure 42 illustrates the method. The equation for the nuclear reaction is shown in the line near the top of the figure. The subscript on the left of the elemental symbol denotes the atomic number of the element, the superscript on the right of the symbol signifies the atomic weights. When a nitrogen nucleus of precisely the correct energy 6.385 Mev is incident upon a hydrogen nucleus, the described reaction takes place. The reaction products, carbon and helium, recoil energetically after the reaction in addition to a 4.45 Mev gamma quantum.

The rate of energy loss$(\frac{dE}{dX})$ of the energetic N^{15} nucleus in silicon has been established at 1.5 Mev/µm. This allows an accurate calibration of the depth of the reaction when the incident beam energy is known. The reaction is a resonance reaction when the incident beam energy is known. The reaction is a resonance reaction since the cross-section, σ,

Figure 42 Hydrogen profiling by resonant nuclear reaction with nitrogen

$${}_1H^1 + {}_7N^{15} \rightarrow {}_2He^4 + {}_6C^{12} + 4.45\gamma \quad E_R = 6.385\text{Mev}$$

$\sigma_{H-N} = 200$ mb $\qquad \sigma_{E \neq E_R} = 10^{-3}\ \sigma_R$
6.385Mev

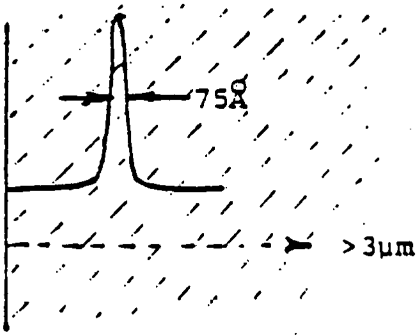

Detection Window ±0.005 Mev

Background ≈ $5 \cdot 10^{19}$ cm^{-3}

Depth Resolution 50 – 100 Å

Hydrogen Concentration:

$$H_{cm^{-3}} = 0.75 \cdot 10^{19} \frac{dE}{dx} \frac{\text{Mev}}{\mu m} \cdot \frac{\#\ \text{counts}}{2\mu\text{coul}} \quad (N^{15++})$$

Exptl const. $\left(1.5 \frac{\text{Mev}}{\mu m}\right)$
(Detector η, σ,
Geometry etc.)

Example of Method: Hydrogen Implant

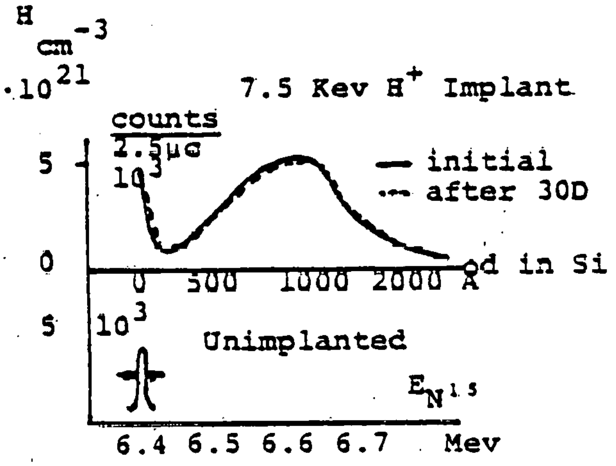

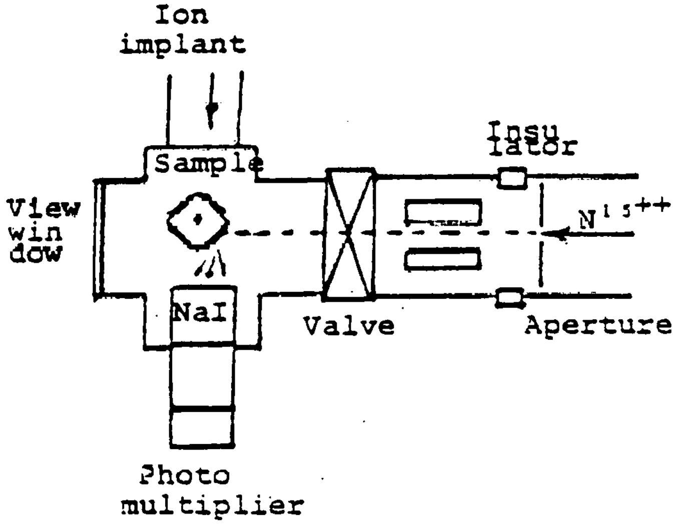

After W. A. Lanford, S.U.N.Y., Albany, N.Y.

at the reaction energy E_R is quite large, 200 millibarns, whereas it falls to σ=0.2mb off energy resonance (outside the reaction window). The right hand side of Figure 42 indicates the silicon thickness equivalent of the reaction window is 75A, Which specifies the resolution of the method. The empirical relation between hydrogen concenration, number of counts and silicon thickness is shown on the middle of the page in figure 42.

The diagram in the lower right of the figure shows an application to a hydrogen ion implantation experiment. The hydrogen ion implantation beam enters the apparatus from above, impinges on he sample on the rotatable cubic sample holder. A 90° rotation allows the sample to be struck by the N^{15+} beam. As the reactions proceed gamma quanta are collected by the NaI crystal of the scintillation counter. The curves on the left illustrate the experimental results, including the insignificant shift in hydrogen concentration after a 30 day dwell time.

The initial experiment utilized solar cell wafers with a series of heat treatments as follows:

Samples 1 and 2	Controls (no treatment)
3 and 4	600°C 10 minutes, N_2, flow
5 and 6	600°C 10 minutes, CO flow
7 and 8	600°C 10 minutes, H_2 flow
9 and 10	600°C 10 minutes, F31 Cu, CO flow
11 and 12	600°C 10 minutes, F31 Cu, H_2 flow

Figure 43 Preliminary results of hydrogen profiling

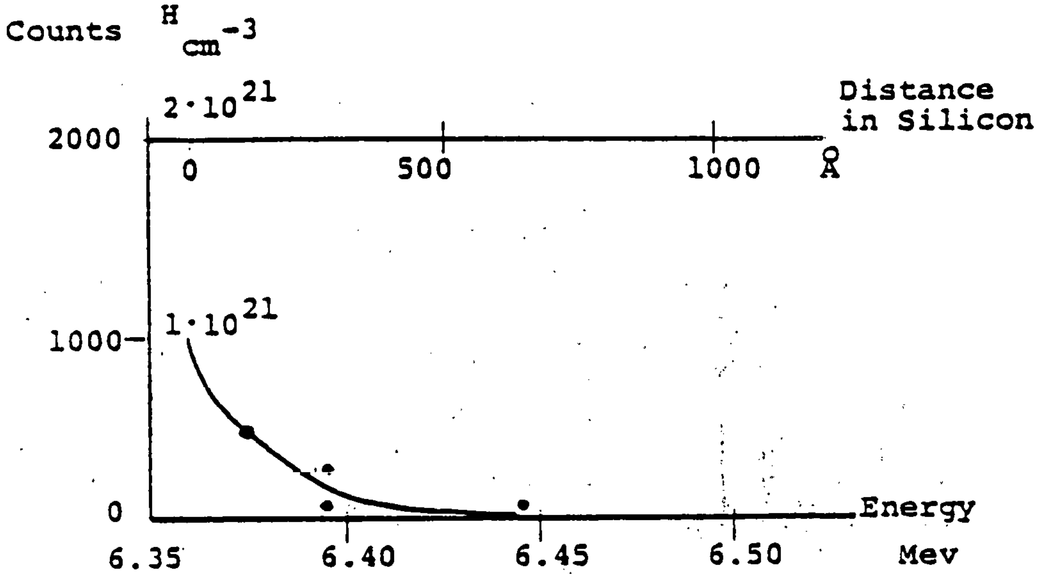

Control sample (untreated)

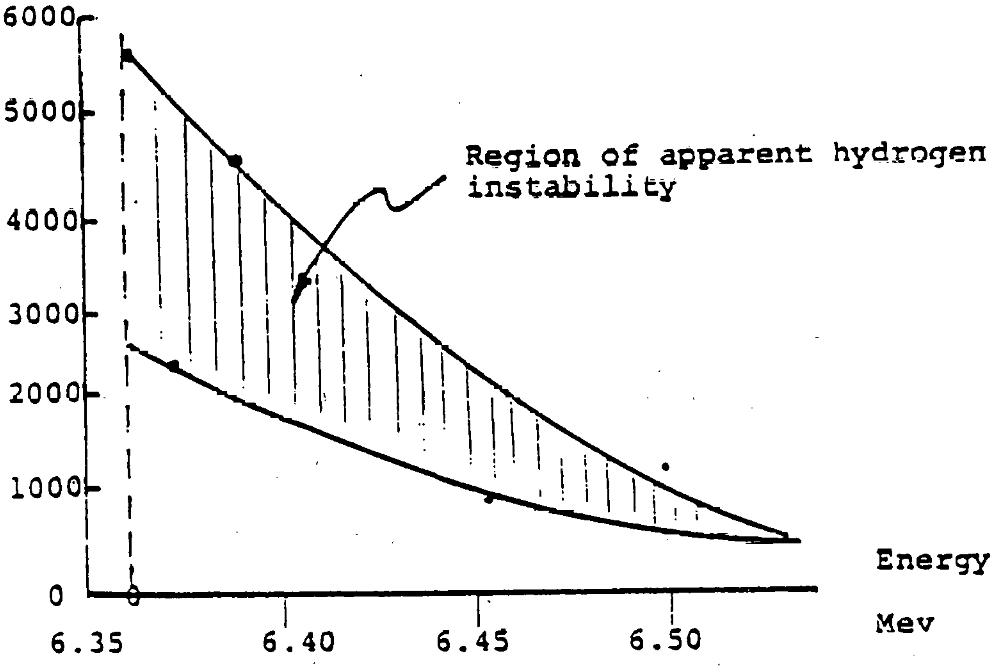

Sample #10, Carbon monoxide fired at 600°C with F31 copper print (removed by scraping)

The samples 9 and 10, screened with F31, were subsequently scraped with a razor blade. The copper electrode was removable with some difficulty. Samples 11 and 12 were also subjected to scraping, but the electrode could easily be removed with a tongue depressor shaped wooden stick. While the copper layers appeared well sintered, none could pass the Scotch tape test.

Since the nitrogen beam incident upon the sample is approximately 1 cm diameter, an attempt was made to cleave wafers into 4 1x1 cm squares prior to shipment. Since wafers were cut off axis, scribe and break was unsuccessful, resulting in oddshaped undersized specimens.

Figure 43 shows two data plots from initial results. The control sample plot is provided with coordinate axes marked with practical units. This sample is well behaved. The other plot is anomalous showing a possible hydrogen instability. Further work is needed with larger samples to clarify the initial results.

9.0 FIRING EXPERIMENTS

9.1 Furnace Calibration

Evidence of drifting of the temperature control chromel-Alumel thermocouple led to a recalibration of the furnace. The profile shown in Figure 44 resulted from probing the furnace tube with a Pt - Pt + 13% Rh thermocouple connected to a digital microvolt meter. Only the exit portion of the profile extending beyond the center of the furnace is shown, as it is the region of major interest in our experimentation. It has been made a part of the experimental protocol to get temperature readings at least at the beginning and end of each run with the platinum thermocouple and digital meter.

9.2 Gas Ambients

During firing tests it was found that:

a) nitrogen firing resulted in severely oxidized copper grains

b) the position of silicon wafers (standing in slotted boat or lying flat) had a bearing on the results

c) the duration of the second step (hydrogen flow) in the two step firing was a factor in the adherence of the electrode to the silicon substrate.

Several explanations are possible for this behavior. Contamination of the source flow gases was ruled out, since it was verified that all nitrogen procured, since firing first commenced, was oil pumped (vs. water pumped), and no other

FIGURE 44 TUBE FURNACE PROFILE

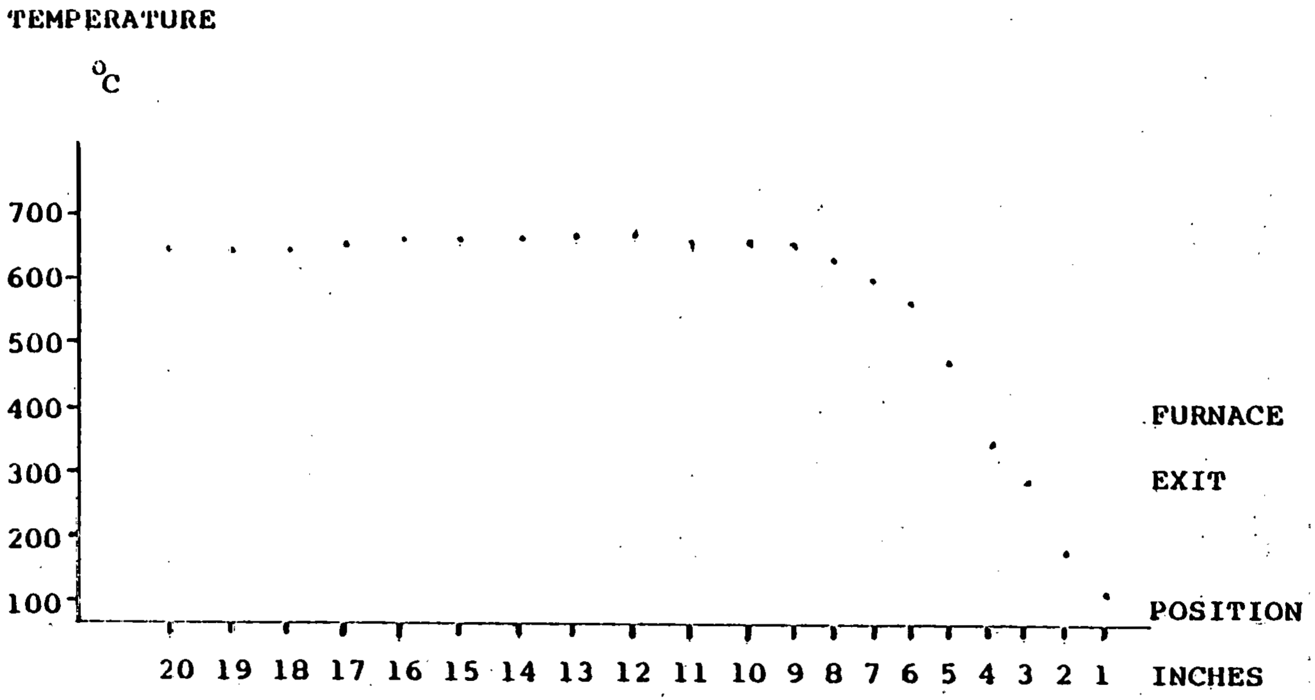

evidence pointed in that direction. However, back streaming, convective flow and therefore air contamination of furnace atmosphere in the open exit quartz tube was considered likely. Further, contamination of furnace quartz furniture was a possibility and was therefore assumed. The following steps were taken to counter the reported problems.

1) Convection and backstreaming were reduced by insertion of an alumna "wool" plug into the quartz tube exit during firing. This plug restricts the exit diameter, breaks up the gas stream into a number of small filamentary streams and increases the velocity of the streams markedly, thereby reducing backdiffusion.
2) All quartz furniture was taken to a professional glass shop for cleaning.

It was found that the higher the temperature of the hydrogen treatment, the more likely electrode separation would occur. At temperatures below 380°C, the effect of hydrogen upon adhesion appeared to be minimal. For this reason a firing profile was devised as shown in Figure 35. While there was some concern that initial oxidation might impair the frit metal wetting process of the copper grains, this proved to be a less significant factor for the following reason: During the initial firing process a reducing atmosphere is produced in the furnace by the organic constituants of the paste vehicle and binder. This material is removed and transported away from the firing site. Only then does the coppergrain matrix as well as the lead frit metal become succeptible to oxidation due to contamination, backstreaming and back-diffusion of oxygen. While this can be reduced, as discussed in the next section, the use of hydrogen during the cooling phase of the firing cycle is helpful in maintaining metallic surface properties and appearance.

The following cleaning procedure was used:

1) Bakeout at 570°C in air (burnout of organic chemicals, convert metals to oxide, remove strains in quartz)
2) Soak in 30% hydrofluoric acid
3) Scrub with cheesecloth (in hydrofluoric acid)
4) Rinse in deionized water and dry

This cleaning procedure is routinely used by General Atomics Corporation, San Diego.

A number of firing experiments were done after the furnace quartz ware was returned to service. The exit baffle diffuser plug allowed making pure nitrogen flow firing without showing visible oxidation. However, neither sintering activity nor adherence were significantly improved. Further, the reproducibility of results with specific pastes either in separate firings or one firing experiments is poor. Because firings are done in a semi-closed system, it was felt that relocation of the equipment might be beneficial. The location of the firing equipment until June 1981, approxiamtely two miles from the Pacific Ocean coast, is within marine layer weather influence. Of particular concern is the possible major contamination with aerosol salt powders. Some evidence of this was seen in the sodium yellow flicker of the hydrogen effluent of the exit flame curtain. It was therefore decided to relocate the firing facility to the Electrink plant approximately 9 miles from the Pacific coast and more under desert weather influence.

9.3 Copper Paste Electrode Firing Experiments

Based upon theoretical analyses and TGA/DTA experiments the silver fluoride content of copper pastes was sharply reduced. Previous silver fluoride additives to copper pastes were approximately 5 weight percent. Copper paste F20 was compounded with 0.7 wt.% silver fluoride.

Firing experiments were carried out with this paste on eleven silicon substrates with surfaces ranging from lightly etched to as lapped (#600 mesh silicon carbide). The prints were dried on a hot plate at 130°C for 5 minutes. During firing the temperature was increased moderately in a number of steps, in a nitrogen flow, up to the peak temperature. The firing temperature was then reduced by transporting the wafers to cooler portions of the furnace. The temperature was reduced to 340°C before hydrogen was added to the nitrogen stream (approximately 50% hydrogen). This resulted in adherent electrodes, passing the Scotch tape test, but showing a somewhat undersintered structure.

Three views are shown of this electrode structure (F20). Figure 46 is an SEM photomicrograph at 2000X giving an average grain size of approximately 0.5 μm. Well sintered structures will give grain diameters of the order of 3-4 m. Also the amount of open area in the grain matrix and lack of continuous paths (lack of coherence) is an indication of undersintering. This can be seen better in Figure 47 and 48 with a magnification of 10,000X and 6,750X respectively. Figure 48 is an edge-on view of a cleaved substrate with electrode. The copper-silicon eutectic phase characterized by large broad based spikes, discussed previously[18] is not apparent on this view. Based on various experiments and reports in the literature, it appears that hydrogen tends to form a strong bond with silicon, displacing metal atoms at the surface. This caused us to change the gas flow sequence during firing so that hydrogen is introduced later, at a time when the specimen temperature is less than 380°C. This modified firing procedure is shown in Figure 45. The purpose of the hydrogen is to reduce any copper or lead oxides that may have formed in previous processing. The disadvantage of this procedure is as follows: Preexisting oxides on the copper grain surfaces and on the lead grains may discourage or prevent the liquid lead from wetting the copper grains. This will in turn reduce the extent of the sintering process and result in a smaller grain size and a less coherent structure. This is believed to be the explanation for the observed microstructure in the above figures. Some mitigation of this problem should occur because of the reducing effect of the organic vehicle of the inks.

While the affinity for dangling electron bonds on silicon

Figure 45 MODIFIED FIRING PROFILE

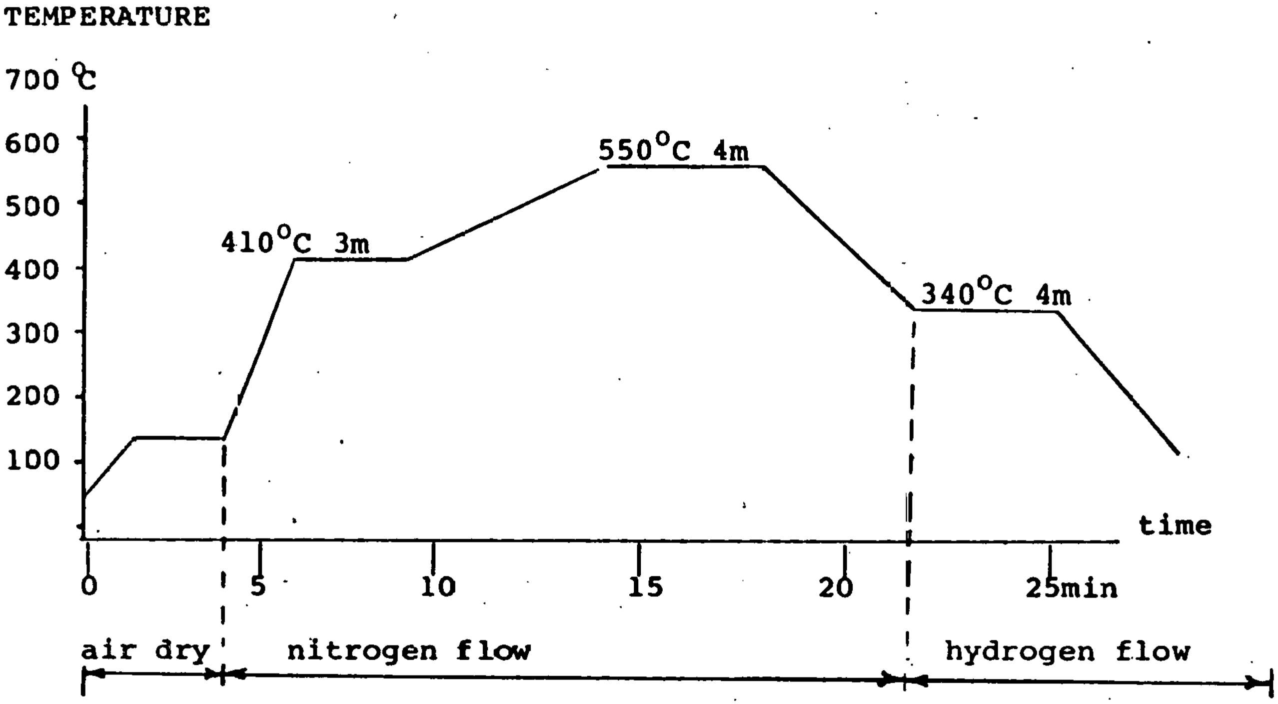

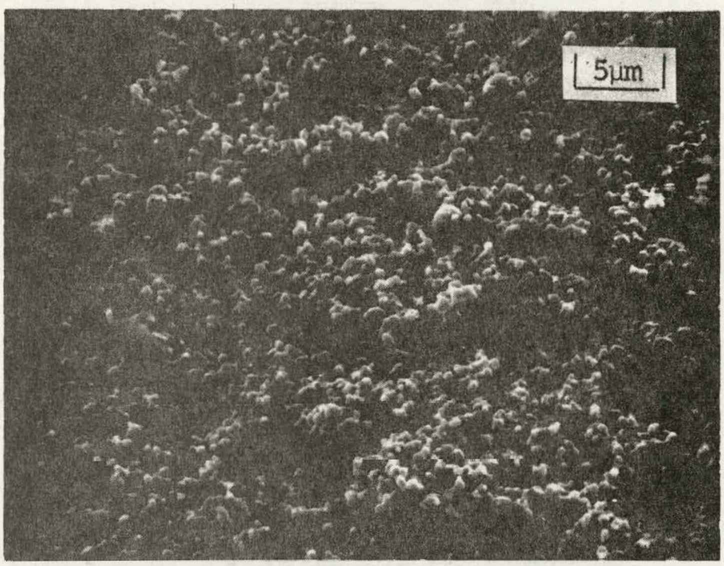

Figure 46. F 20 copper electrode sintered at 615°C taken at 2000X

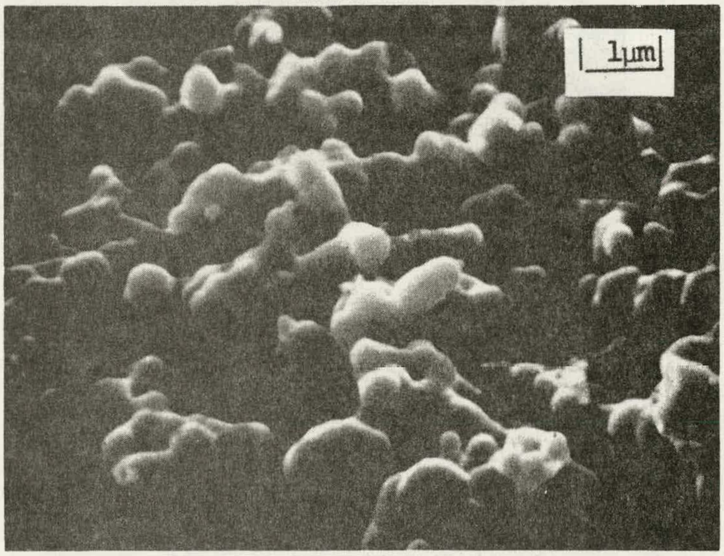

Figure 47. Same as above at 10,000X

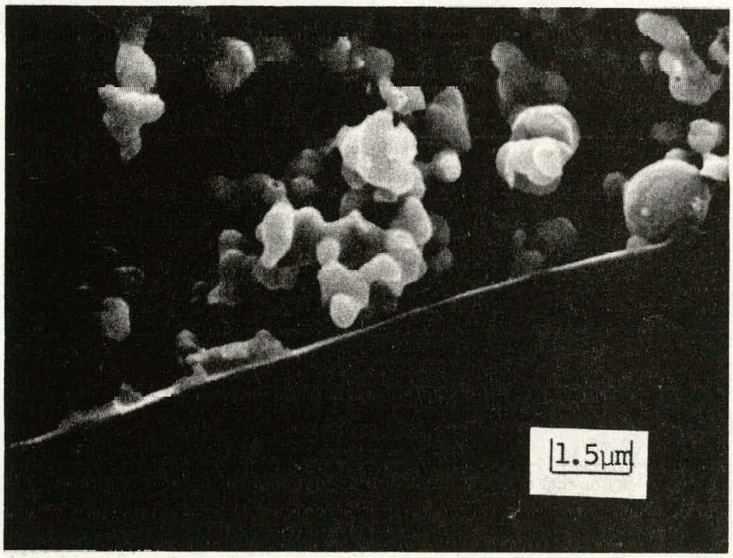

Figure 48. Edge on view of F20 copper electrode sintered at 615°C at 6,750X magnification

surfaces appears to be a property of hydrogen, this is not expected to be true for other gaseous reducing ambients. To this effect carbon monoxide has been proposed as a reducing ambient in the firing process.

9.4 Solar Cell Firing Experiments

A set of five pastes was prepared for solar cell firing experiments. The compositions of the pastes are given tin Table VIII.

TABLE VIII

COPPER PASTE COMPOSITIONS

PASTES	F30	F29	F28	F27	F26
Composition (wt%)					
Vehicle 13	28.0	28.0	28.0	28.0	28.0
Copper	62.0	59.42	62.0	59.42	64.82
Lead	6.2	5.94	6.2	5.94	6.48
Ge-Al Eutectic	3.1	5.94	3.1	5.94	0.00
Silver Fluoride	0.70	0.70	0.70	0.70	0.70
Fineness of Grind (FOG) (μm)	12	9	10	11	13
Viscosity #7 Spindle 10 RPM(MCPs)	42	42	42	42	42

Laser scribed wafers were cleaved with a 95% yield. Front-back identification was made by hot point probing. Back contacts were screened, dried and fired by the modified two step method (Reference Section 3.1 this report) at three temperatures 550°C, 600°C and 650°C. After firing, cells were packed and taken to the JPL Solar Cell. Processing Laboratory for front contact application and AM1 simulator testing.

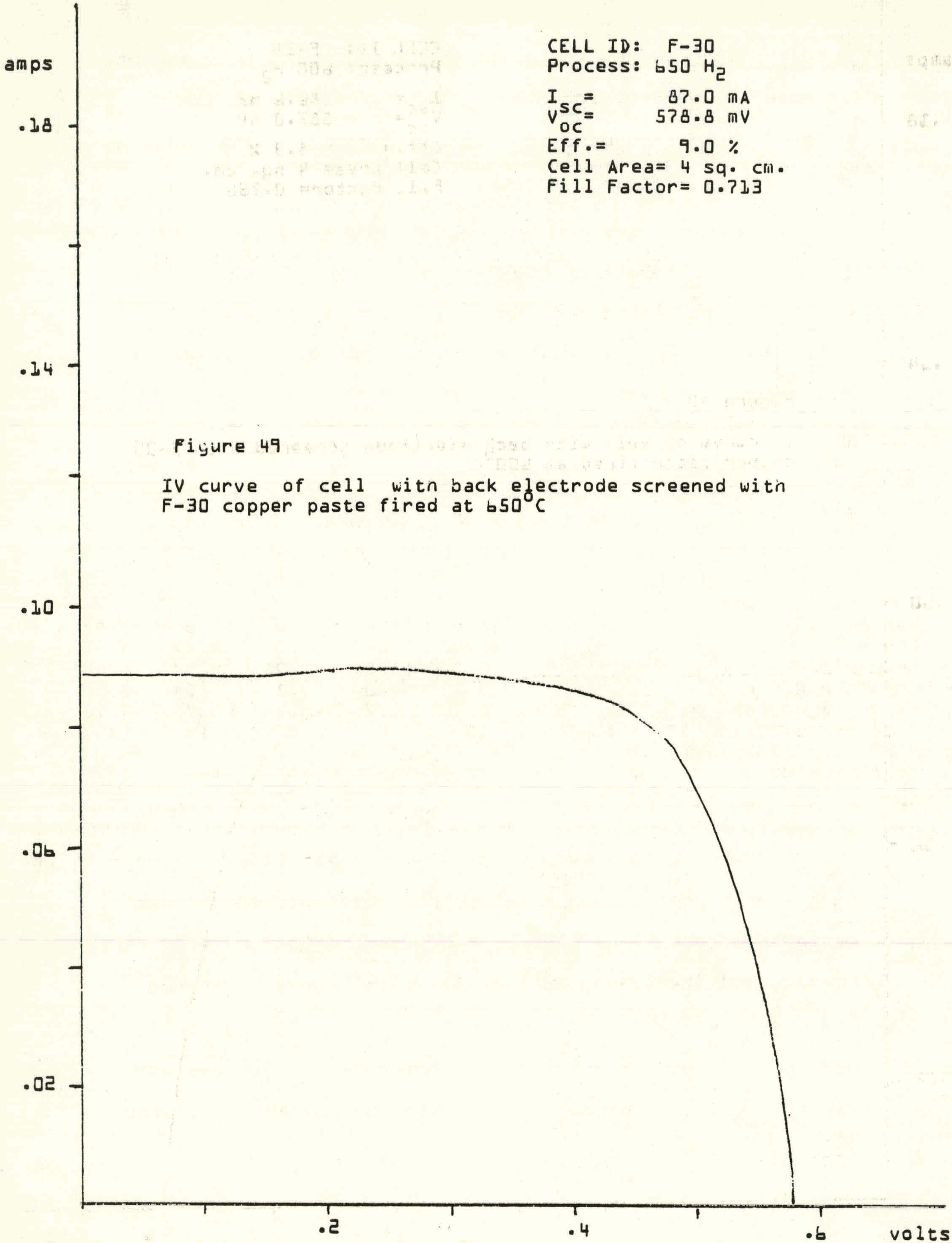

Figure 49

IV curve of cell with back electrode screened with F-30 copper paste fired at 650°C

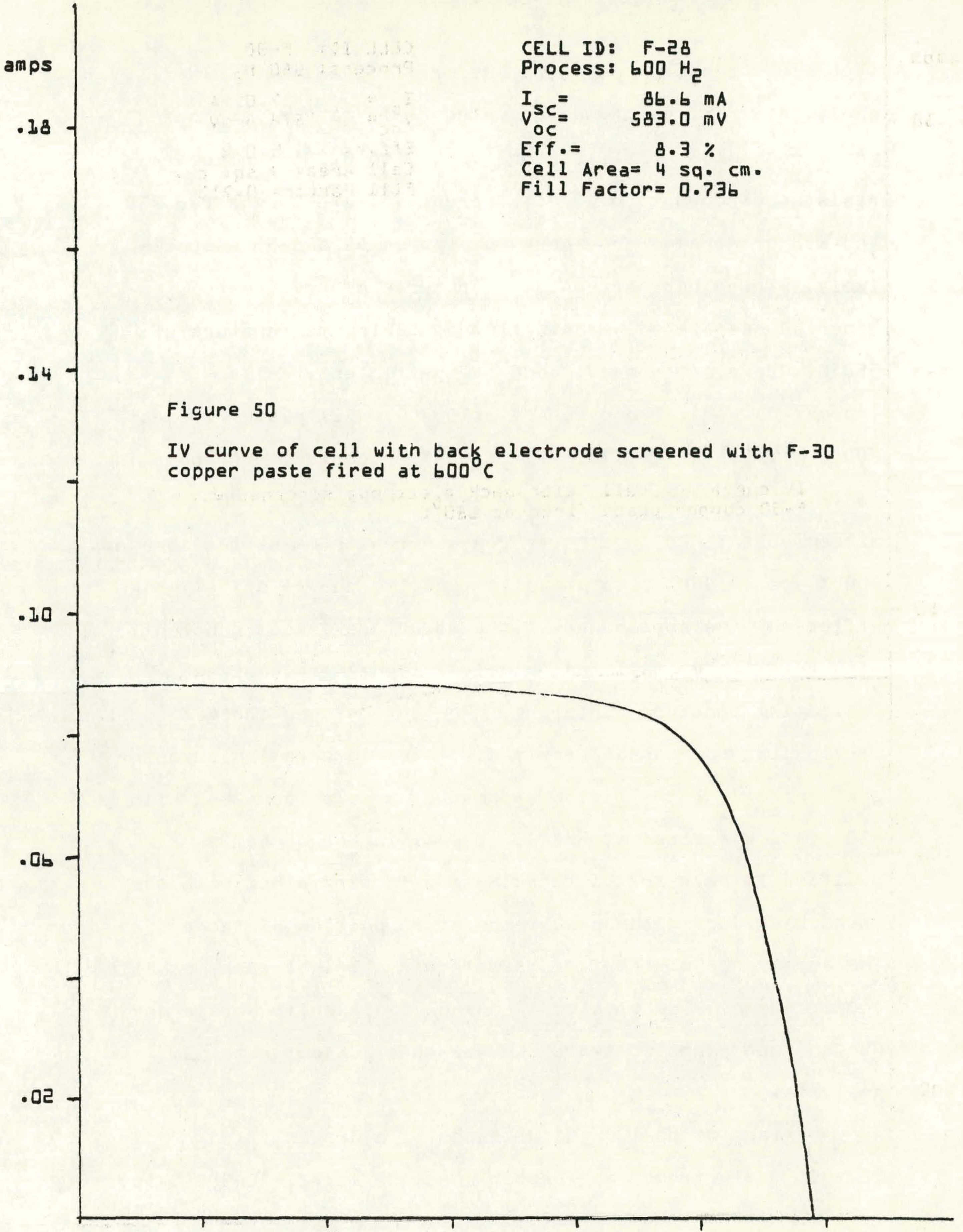

Figure 50

IV curve of cell with back electrode screened with F-30 copper paste fired at 600°C

IV traces of cells done with F26, 27, 28, 29 and F30 were analyzed. Sixteen of the uncoated cells gave efficiencies greater than 8%. Fill factors ranged to 0.733 and series resistances down to 0.22 Ω. Current-Voltage curves for F30 and F28 electrodes are shown in Figures 49 and 50 respectively. Three barrier contacts (reverse S curve) were observed associated with the lowest firing temperature of 550°C. However, some 8.1 and 8.2% efficiency cells (uncoated) were also obtained at 550°C. F27 paste fired at 600°C gave an AM1 efficiency of 8.9% (uncoated) extrapolating to 12.2% Figure 51. This cell was dissected for SEM micrographs shown in Figure 52 A and B with magnifications of 2000X and 10,000X respectively. Despite the relatively high efficiency the appearance of the structure is not coherent, with relatively small (and widely varying) grain sizes, indicating immature sintering. The carbon monoxide gas previously ordered was received. After integration into the gas manifold of the firing apparatus, a wafer screened with F30 paste was fired at 584°C. The firing sequence was modified to have the CO reducing gas flowing along with the N_2 carrier during the peak temperature portion of the cycle. The appearance of the fired sample was a bright pink metallic copper sheen. The electrode passed Exacto knife scrape and Scotch tape adhesion tests and was then subjected to SEM analysis.

A comparison of the SEM micrographs of hydrogen fired F27-650°C electrodes and carbon monoxide fired F30-584°C is

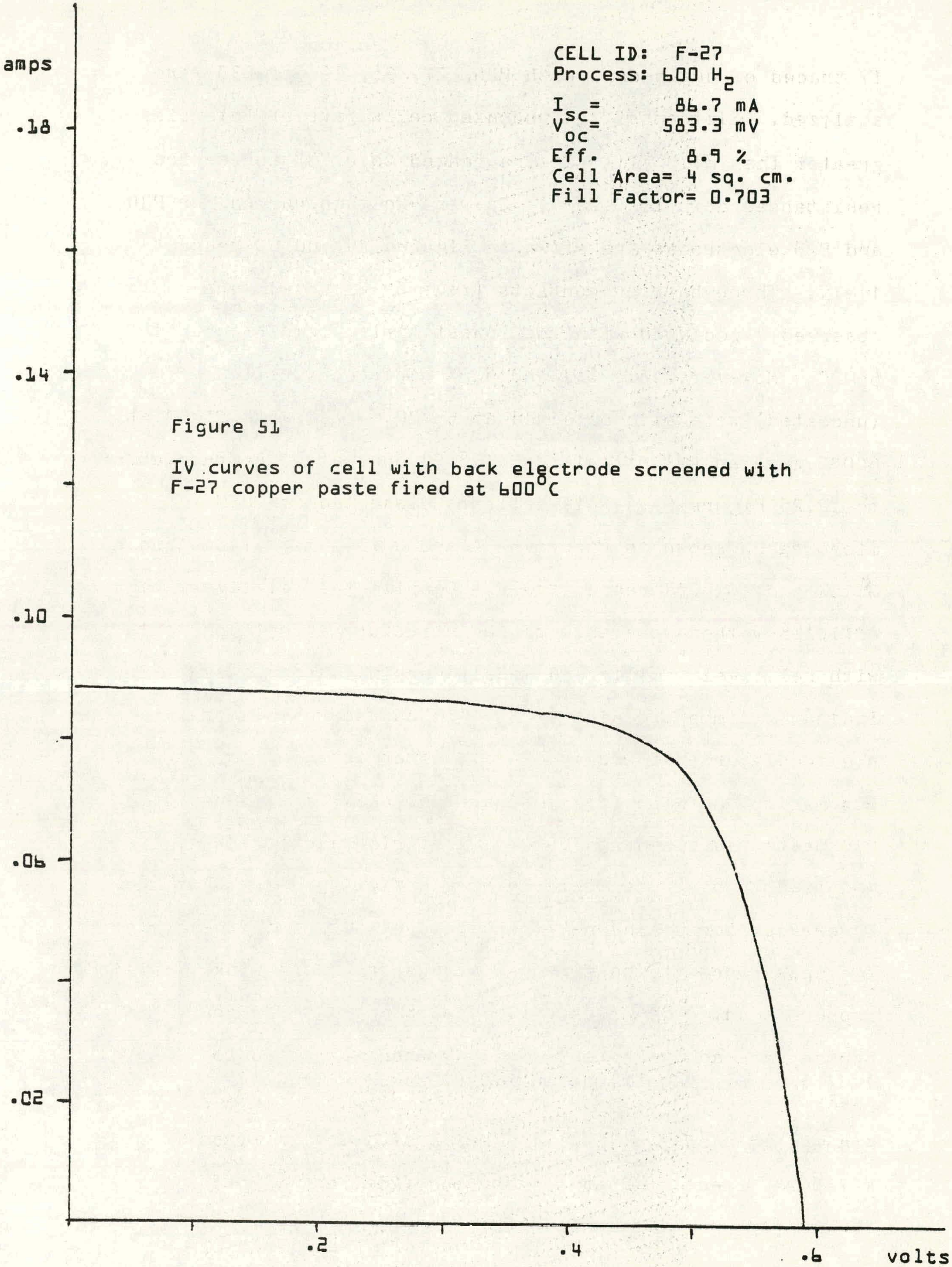

CELL ID: F-27
Process: 600 H_2
I_{sc} = 86.7 mA
V_{oc} = 583.3 mV
Eff. 8.9 %
Cell Area= 4 sq. cm.
Fill Factor= 0.703

Figure 51

IV curves of cell with back electrode screened with F-27 copper paste fired at 600°C

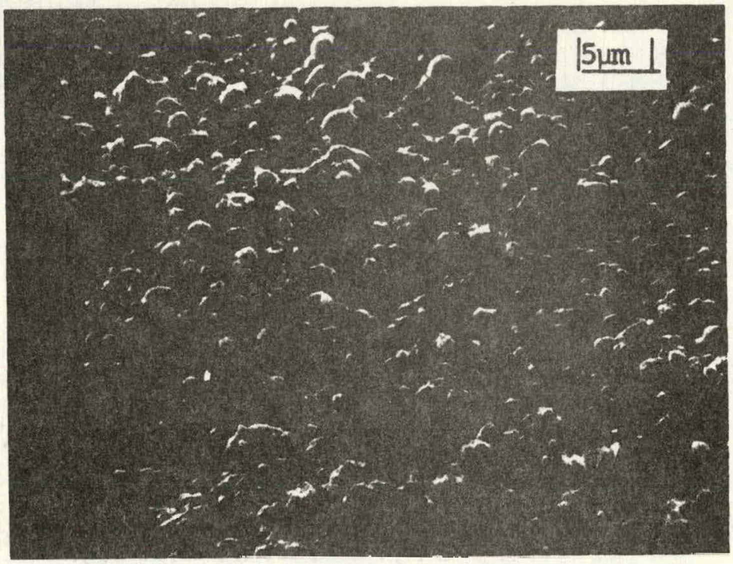

A. Magnification 2,000X

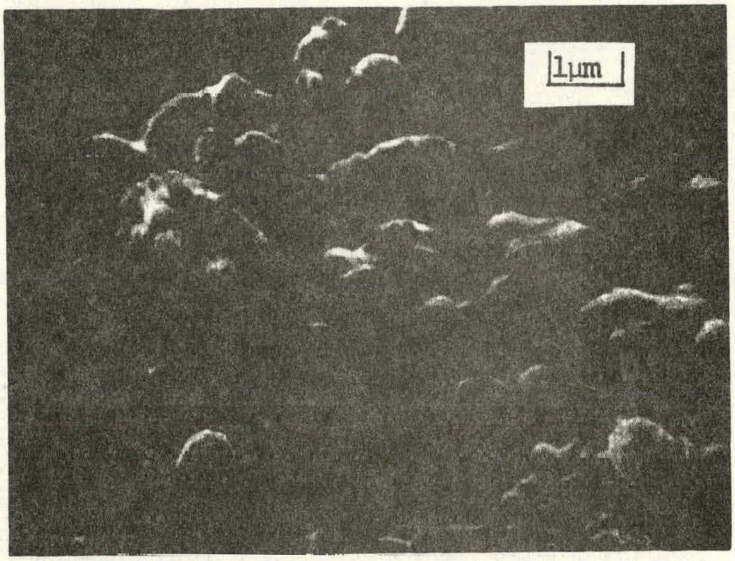

B. Magnification 10,000X

Figure 52. F27 Silver fluoride activated copperpaste fired at 600°C, with modified two step process

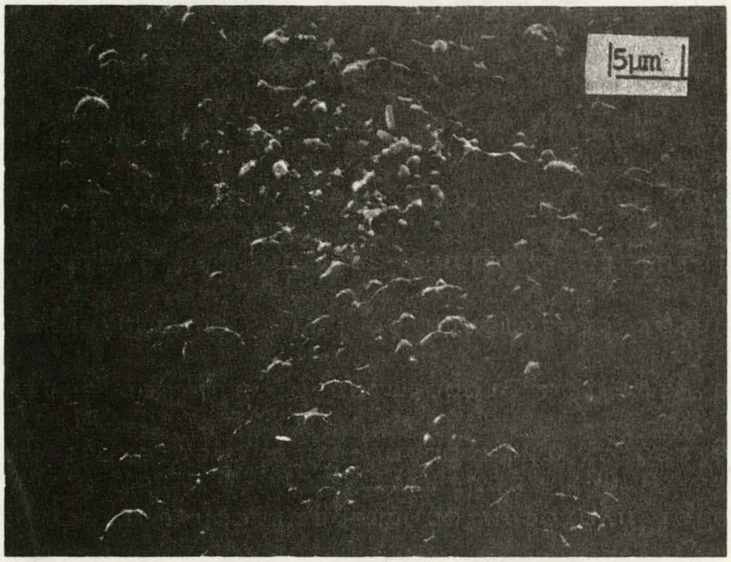

A. F27-650°C, H_2, Magnification 2,000X

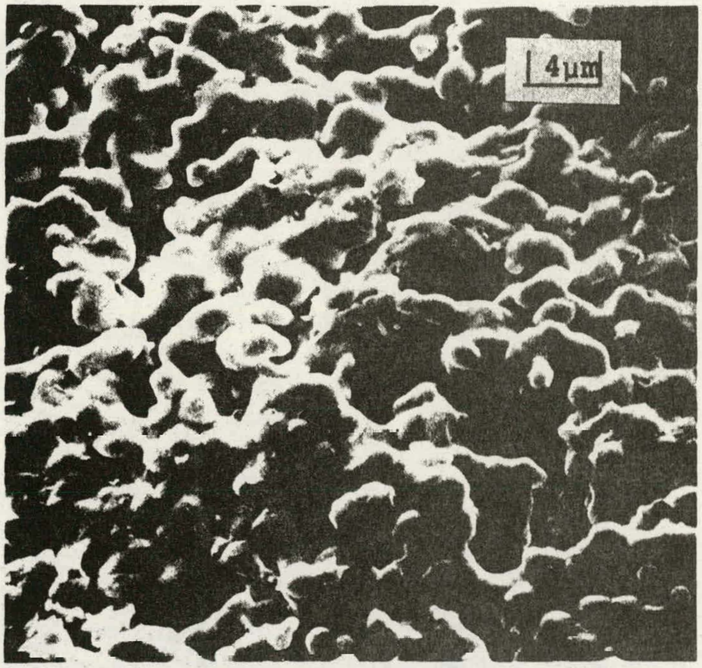

B. F30-584°C, CO, Magnification 2,600X

Figure 53. Comparison of copperpaste hydrogen and carbon monoxide firing cycles

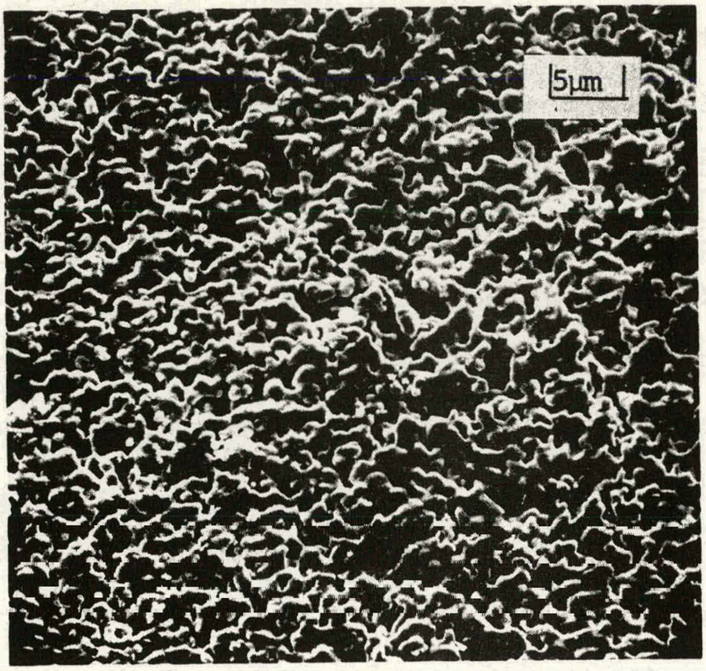

A. Magnification 1000X

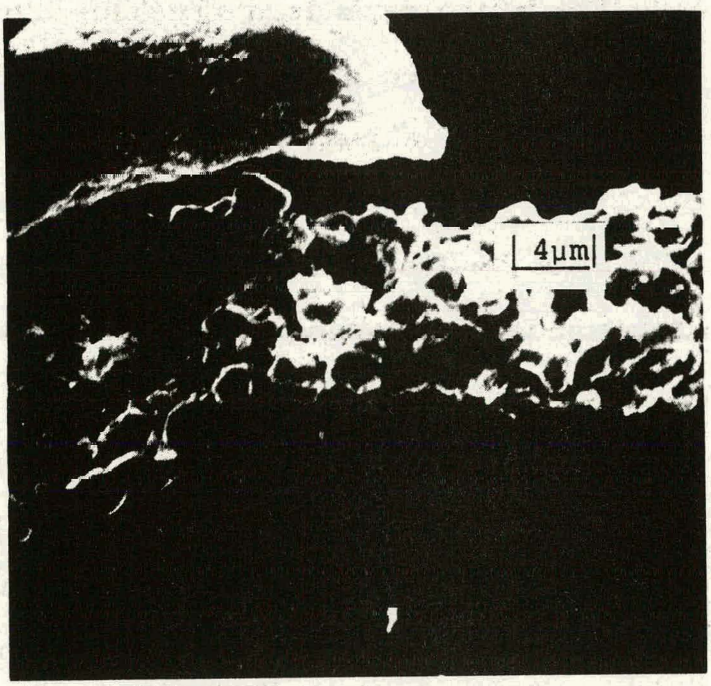

B. Edgeview, magnification 2,300X

Figure 54. F30-584°C Carbon Monoxide Fired

of interest. This can be seen on Figure 53 A and B, respectively. Although the magnifications are roughly comparable and the hydrogen fired sample was at a higher temperature (650°C vs 584°C) the degree of sintering in the carbon monoxide fired specimen is vastly greater. This is believed to be due to the prevention of oxide formation early in the firing cycle with consequently better wetting (as discussed in Section 9.3).

Figure 54 A and B show a more microscopic view and an edge on view, respectively. The 1000X micrograph again demonstrates the dramatically improved sintering. The cleaved portion of B shows the absence of a spiked eutectic phase but appears to show good substrate wetting. The large amorphous-appearing structure above the micrograph is a brushed-on coating of graphite to prevent specimen charging. Figure 55 shows another SEM micrograph of a region of the F30-CO print that was scratched with a diamond scribe. The rounded regions with and without the growth striations were subjected to energy dispersive x-ray analysis. The prominent lines were identified as lead.

The problem of hydrogen firing in conjunction with evidence from the literature provides a reasonable basis for hydrogen saturation of dangling bond electrons. This displaces metal atoms of electrode materials. For this reason hydrogen is an unlikely candidate for a reducing gas firing ambient.

The evidence obtained from the carbon monoxide firing makes it appear well suited to the task. However, preliminary

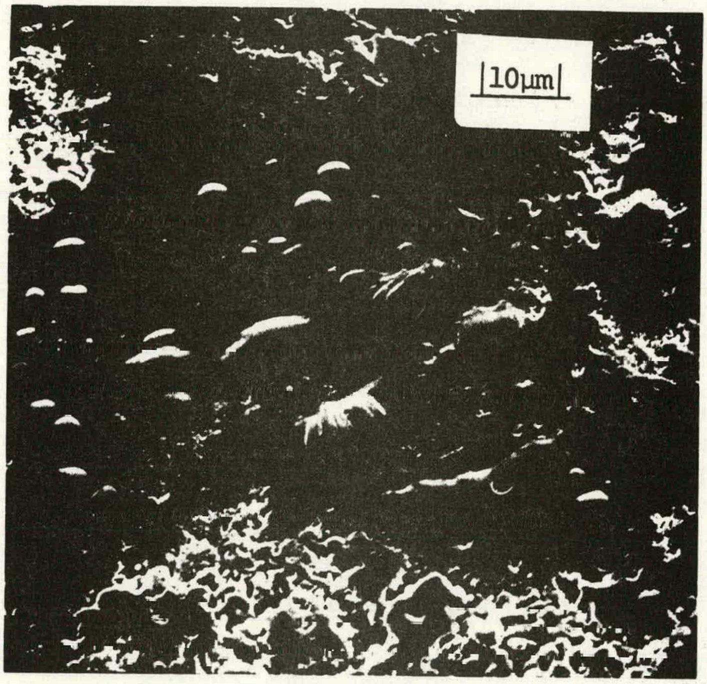

Figure 55. F30-584°C CO with diamond scribed scratch at 1,000X magnification

experiments with fluorocarbon pastes fired in CO still show a lack of consistently good adhesion. This has led us to continued experimentation with silver fluoride activated inks.

Good efficiency and relatively good adhesion have been obtained for hydrogen fired pastes with small (<1wt%) silver fluoride additives.

A solar cell experiment was carried out with copper pastes F19 and F20. Compositions are given in Table IX.

TABLE IX

COPPER PASTES F-19 AND F-20

Material	F19 wt%	F20 wt%
Vehicle	31	30
Copper	59.4	62.4
Lead	5.9	6.2
Al-Si Eutectic	0.6	0.7
Silver Fluoride	-	-
Lead Acetate	2.4	-
Fluorocarbon	0.7	-

Copper pastes were screened onto the backs of phosphorus diffused 2X2 cm solar cell blanks. Screened wafers were dried and subsequently fired at 615°C Peak Temperature. Titanium-palladium-silver contacts were evaporated through a mask onto the front of the devices. Two control cells were made of the same material with Ti-Pd-Ag contacts front and back. Representative IV curves are shown in Figures 56 and

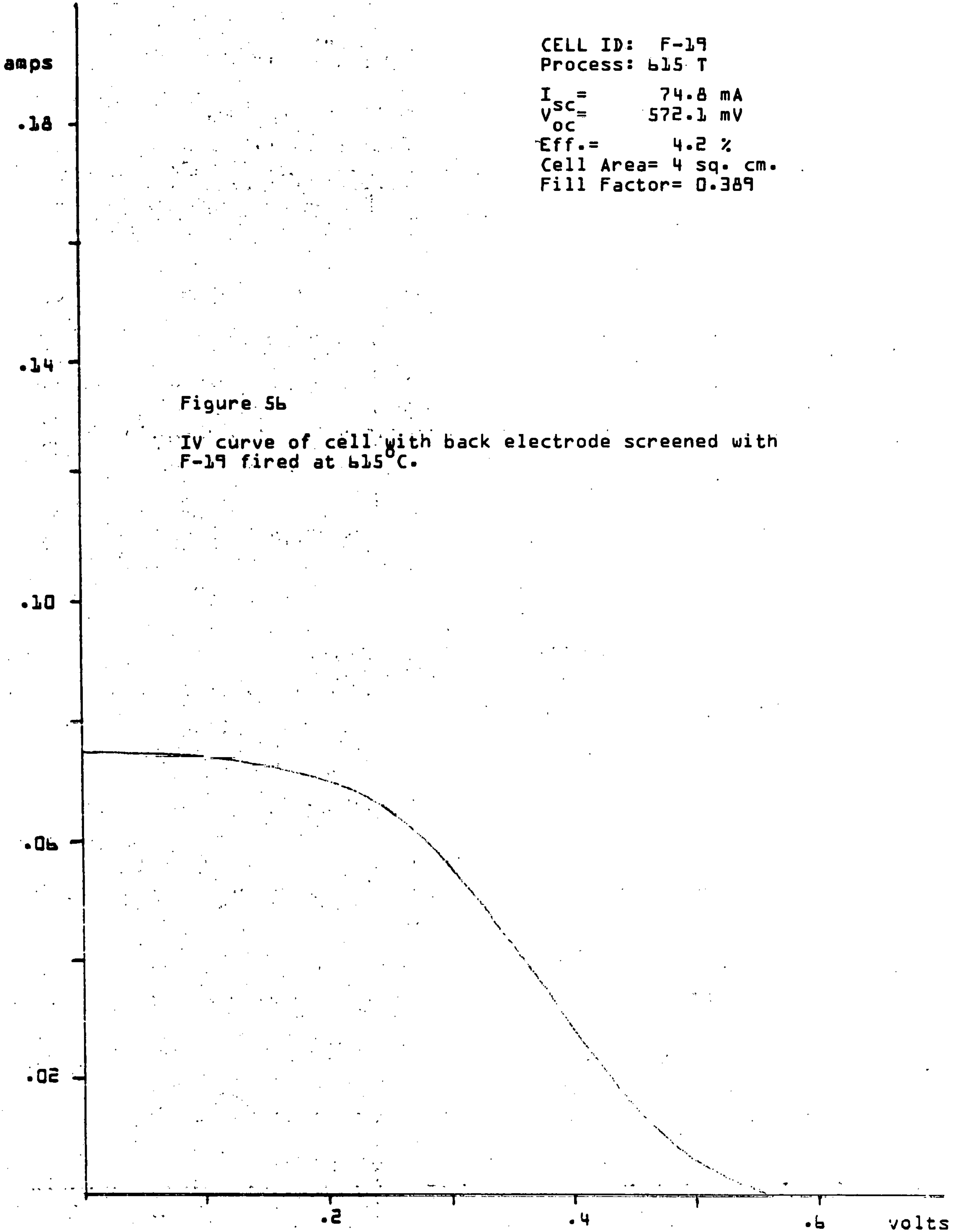

CELL ID: F-19
Process: 615 T

I_{sc} = 74.8 mA
V_{oc} = 572.1 mV
Eff.= 4.2 %
Cell Area= 4 sq. cm.
Fill Factor= 0.389

Figure 56

IV curve of cell with back electrode screened with F-19 fired at 615°C.

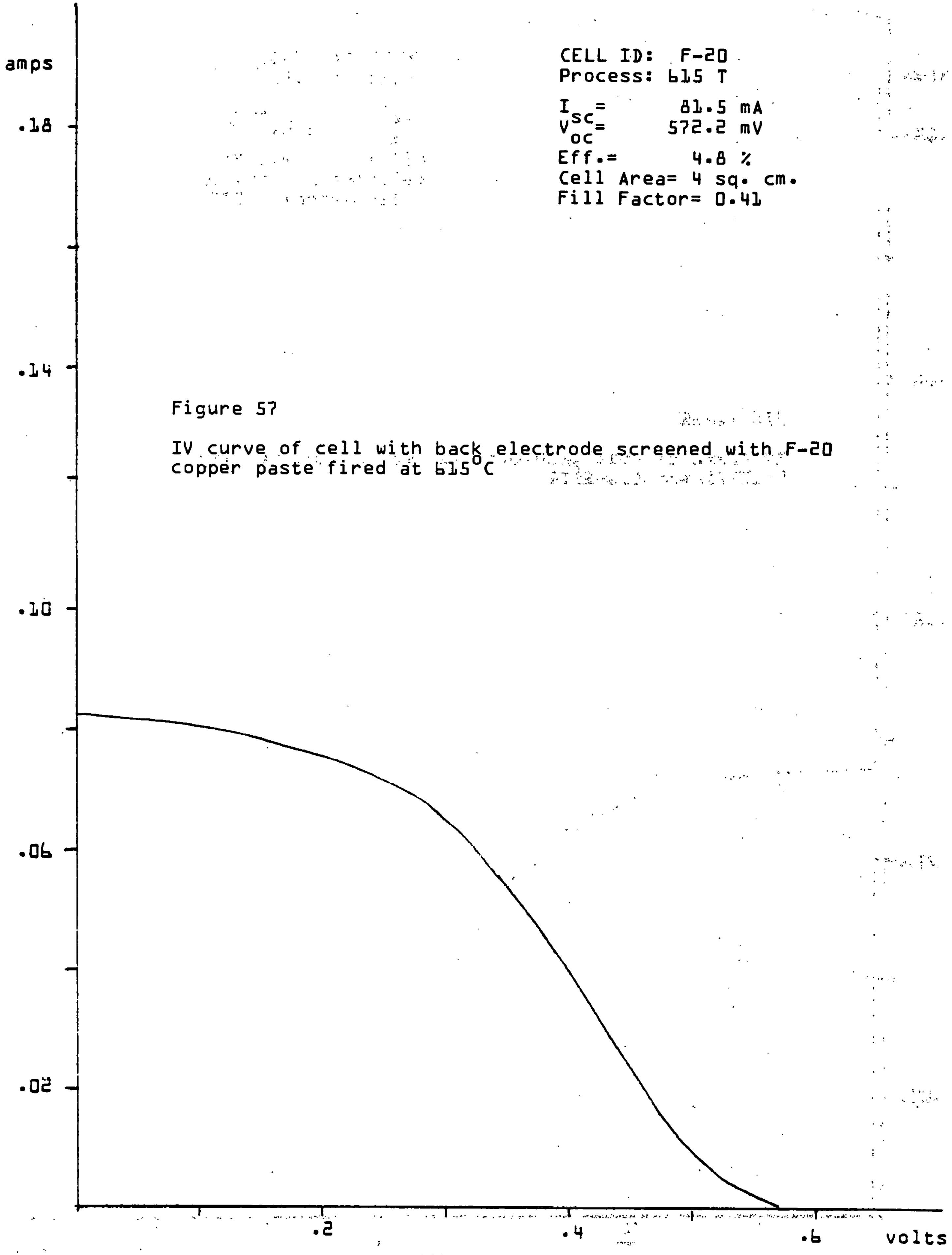

Figure 57

IV curve of cell with back electrode screened with F-20 copper paste fired at 615°C

57. The control cells gave normal IV curves with AM1 efficiencies in the 8% range (without AR coating).

The reverse S shaped curves are likely to be due to an electrical barrier in series with the ohmic contact. This may be a consequence of a relatively low firing temperature (615°C), although good contacts have been made at even lower temperatures (550°C).

It is interesting to note that similar curves were obtained although the pastes are, in one case, fluorocarbon (F19) and in the other, (F20), silver fluoride activated. The application of the evaporated electrodes as well as the AM1 simulator measurement and curve tracing were done by the Solar Cell Processing Laboratory of Jet Propulsion Laboratory.

An experiment was undertaken to explain the reverse S shaped curves obtained from the IV traces of solar cells during this experiment (Figures 56 and 57). An X-Y recorder was utilized with a solar cell as shown in Figure 58. The rough IV traces resulted from the crude load circuit utilizing a single 2 kΩ variable resistor. The illuminated solar cell with the transistor emitter shorted is shown as condition 1. The trace labeled 2 shows the switch open, putting the germanium emitter in series with the solar cell and yielding a facsimile of the reverse S shaped curve.

Figure 58 Circuit-Simulated IV Curves

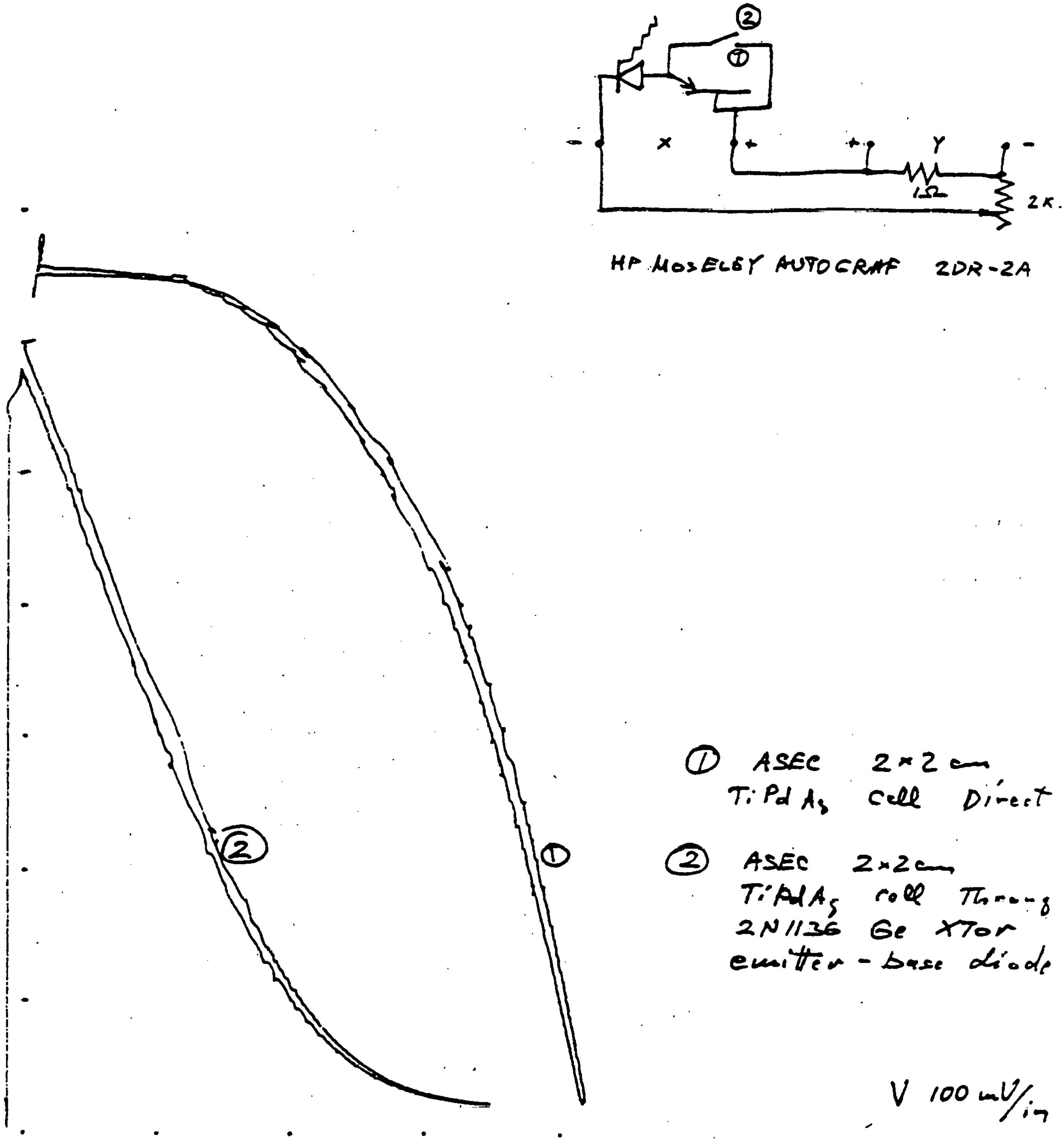

10.0 COST ANALYSIS

While pastes manufactured to date do not satisfy all the requirements with respect to adhesion, electrical properties and resistance to environmental factors, a preliminary cost study was undertaken.

The cost elements provided in this study should be looked upon as constituting the upper limit in most cases. The major constituent, copper metal powder, is presently obtained from a high priced source in order to maintain close limits on a variety of physical parameters. It is expected that further experimentation and insight will allow the utilization of a less expensive material, however, present colculations are based upon the high copper price of $32/lb. This material has not been made in volume production by the manufacturer.

The sample pastes chosen for the cost analysis are F12 (silver fluoride) and F13 (fluorocarbon) compositions. Material costs and component cost percentages are given in Table X. The material costs are given in dollars per troy ounce of paste.

The third and sixth column of numbers give the component cost percentages of the total paste material costs. This number shows the cost drivers which are (in order of importance): copper, solvent, resin and eutectic materials, with silver fluoride being in 5th place.

TABLE X

COST OF MATERIALS OF FLUOROCARBON AND SILVER FLUORIDE ACTIVATED COPPER PASTES

MATERIAL	PASTE F12 AMOUNT(wt%)	PASTE F12 COST $	PASTE F12 COST %	FASTE F13 AMOUNT(wt%)	FASTE F13 COST $	FASTE F13 COST %
Organic Solvent	31.2	0.343	20.5	30.8	0.338	21.0
Resin	4.2	0.093	5.56	2.2	0.0619	3.83
Thixotropic Agent	0.6	0.0089	0.53	0.4	0.0059	0.37
Copper Powder	57.1	1.142	68.29	56.9	1.138	70.44
Lead Powder	4.6	0.014	0.84	4.6	0.014	0.87
Aluminum-Silicon Eutectic	1.2	0.044	2.63	1.1	0.041	2.54
Silver Fluoride	1.1	0.0275	1.64	-	-	-
Lead Acetate	-	-	-	2.3	0.0122	0.76
FluoroCarbon	-	-	-	1.1	0.0043	0.27
TOTAL MATERIAL COST		$1.6724/oz			$1.6156/oz	

Based upon moderately large quantity production, the labor has been calculated at $0.50 per oz.

Labor + Material	$2.1724/oz	$2.1156/oz

Depreciation:

The major apparatus for paste fabrication is the roller mill. New cost for a 5 X 10" mill is $8,000. Assuming an eight year life, milling rate of 12 oz/hour, 24,000 oz/year or 200,000 oz/per mill life. Factoring this into purchase costs gives $0.04/ oz depreciation cost.

F12 = $2.2124/oz F13 = $2.1556/oz

Ancillary Material Costs

Paper wipes: one per oz, 140/box @ $2.00/Box, $0.014/oz

Cleaning solvent (MEK) $209.60/55 gal. drum

= 3.8/ gal

$1.007/liter and 50cc/oz $0.050/oz

Glassware (breakage + packaging)

1 beaker/1000 oz	@ $2.00	$.002	
10 oz jar	@ $0.45	$.045	$0.047/oz
			$0.111/oz

F12 = $2.3234/oz F13 = $2.2666/oz

Postulating a yield of 80%

F12 = $2.904/oz F13 = $2.2666/oz

and stipulating a gross profit and sales cost of 30% we have a final cost of

$3.77/oz (silver fluoride)	$3.68/oz (fluorocarbon)
$0.121/g	$0.118/g

Cost per cell (Assuming 4" OD)

Front 8% coverage	0.025g required
Back 95%	0.297g required
Total	0.322g required
$0.0390/cell	$.0380/cell

Additional cost of hydrogen firing: $60/1000 cu. ft. flow 5 l/min for 30 min./run 28,300 l/tank = 189 runs/tank

50 cells/run 189 runs = 9450 cells/tank @ $60

$$\frac{\$60/\text{tank}}{4450\text{ cells}} = \$0.0063/\text{cell}$$

Contact cost per cell

	F12 (silver fluoride)	F13 (fluorocarbon)
	$0.0390/cell	$0.0380/cell
hydrogen cost	.006	.006
	$0.0450/cell	$0.0440/cell

11.0 CONCLUSIONS AND PROBLEMS

1. Both silver-fluoride and fluorocarbon screened paste electrodes can be produced for approximately $0.04 per watt.
2. Copper pastes using the all metal concept have been shown to provide good back contacts without any tendency to short the junction. Long term reliability has not been shown, and problems have occurred with securing good adhesion reproducibility. Hydrogen reducing atmospheres have been found to destroy existing bonds between silicon and copper, as well as silver. Copper pastes have not provided nonshunting contacts to solar cell front surfaces. Carbon monoxide has worked well as a reducing ambient in copper paste firing, but has not removed the reproducibility question.
3. Good results have been obtained for small firing loads with .7 weight % silver fluoride-activated copper electrodes. Self contaminants appear to cause poor reproducibility of adhesion when larger loads are attempted.
4. A fluorocarbon-activated copper paste (F-16) gave a projected AMI efficiency of 10%, however, fluorocarbon-copper pastes require further modification to achieve reproducibly adherent electrodes.

5. The effect of hydrogen upon adhesion has brought into question the basic nature of the electrode bonding mechanisms. Many observations support the hypothesis that hydrogen, at firing temperatures, disrupts metal-to-silicon bonds, replacing metal and causing separation of electrodes.

12.0 RECOMMENDATIONS

A problem which must be solved is the lack of reproducibility. This may be due in part to the variability in certain raw materials such as silver fluoride, and to the possibility of self contamination, possibly based upon the number of wafers being fired.

A more complete understanding of the chemical processes, outlined in Section 7, would be helpful in achieving better control. This can be facilitated by further experiments with thermogravimetric analysis (TGA) and differential thermal analysis. (DTA)

The role of hydrogen on the silicon surface can only be hypothesized at this point. Further experimentation and analysis with the properties of silicon surfaces exposed to various heat treatments in hydrogen ambients, would be not only helpful to a narrow segment photovoltaic processing technology, but to the whole semiconductor technology and industry.

Another approach to the hydrogen problem is experimentation with alternative reducing ambients, such as carbon monoxide for example.

Finally the question whether copper electrodes can be used in solar cell front surfaces must be further addressed.

13.0 APPENDICIES

13.1 Appendix A

TABLE XI

PASTE COMPOSITIONS (Wt %)

Code	Vehicle	Cu metal	Oxide Scavenger	Lead Frit metal	Lead Acetate	Eutectic Additive
F1	23	69.4	A3.8	3.8	-	-
2	Similar to S071 Different suppliers					
3	23	69.3	A3.9	3.9	-	-
4						
5	23	70	C1.6	5	-	-
6	44	49.8		A3.1	-	-
7	43	52	C1.2	3.5	-	-
8	35.3	60	C1.2	3.5	-	G3.9
9	22.2	66.7	A3.7	3.7	-	G3.7
10	22	66.6	A3.7	3.8	-	-
11	36	53.3	C2.1	4.3	-	S4.3
12	36	57.1	A1.1	4.6	-	S1.2
13	34	56.9	C1.1	4.6	2.3	S1.1
14	33	F57.8	C1.1	4.6	2.3	S1.2
15	43.4	F48.8	C0.9	3.9	2.0	S1.0
16	33	55.8	C1.1	4.5	4.5	S1.1
17	33	58.8	A1.2	5.9	-	S1.1
18	32	57.7	C1.1	5.8	2.3	S1.1
19	31	59.4	C0.7	5.9	2.4	S0.7
20	30	62.4	A0.7	6.2	-	S0.7
21	28	61.2	A3.6	3.6	1.5	-
22	34	55.8	C1.1	Sn 3.6 Pb 1.5	4.5	-

F = Flake C = Fluorocarbon G = Al-Ge

A = Silver Fluoride S = Al-Si

13.2 Appendix B

Paper presented at the 4th E.C. Photovoltaic Energy Conference, Stresa, Italy (May, 1982)

PATHOLOGY OF SOLAR CELL CONTACTS

B. ROSS
Bernd Ross Associates
San Diego, CA 92109 U.S.A.

Summary

Energy level diagrams of metal contacts to silicon solar cells are examined, as well as equations governing the tunneling conductance. Symptoms of some solar cell contact problems are mentioned and potential diagnoses are suggested. These include the "flat spot" phenomenon and "S" shaped curves along with the more common series and shunt resistance problems, which all result in poor fill factor and consequently lower efficiencies. Examination of contacts along with controls, indicate that this contact method does not impose an efficiency limitation.

1. INTRODUCTION

Solar cell contacts provide the electrical interface between the energy conversion element and the load circuit. In order to function efficiently they must provide a low loss path for the generated current. Simultaneously they should be economical in material and fabrication process, and function reliably over long periods.

A portion of this work is the result of one phase of research conducted by the Jet Propulsion Laboratory of the California Institute of Technology for the U.S. Department of Energy through an agreement with the National Aeronautics and Space Administration.

Several techniques are available to apply solar cell contacts, including plating,[1] alloying,[2] vacuum evaporation,[3] and thick film screening.[4,5]. Despite this variety the final electrical configuration is relatively simple, and is illustrated below.

2. FRONT CONTACT

The front contact of modern solar cells is applied to nearly degenerate n type semiconductor surfaces with impurity concentrations from 10^{19} atoms to 10^{21} atoms with phosporus being the donor conventionally in use. The high surface concentration allows better front contacts since the electron tunneling probability is a function of the carrier concentration on both sides of the interface. When a metal coats the surface of a semiconductor, the depletion width within the semiconductor shrinks as a function of carrier concentration, enhancing the tunneling probability. This improves carrier flow through the barrier constituted by the contact potential between contact metal and semiconductor surface.

The depletion width, W, can be calculated from

(1) $W = \sqrt{\frac{2\varepsilon_s}{qN_{D.A}} (V_R + V_D - \frac{kT}{q})}$ cm Ref 6

where ε_s = permittivity of the semiconductor $1.06 \cdot 10^{-12}$ F/cm

q = electronic charge, $1.6 \cdot 10^{-19}$ Coulomb

N_D = donor concentrations, $1 \cdot 10^{20}$ cm^{-3}

N_A = acceptor concentration, $5 \cdot 10^{19}$ cm^{-3}

V_R = applied bias voltage, $V_R = 0$

(2) V_D = $\phi_B - \phi_n$ = contact potential

ϕBN = copper - semiconductor barrier = 0.69eV Ref 7

ϕBP = 0.46eV Ref 7

(3) ϕn = $Ec - E_F$ = 0.0326eV

ϕp = $E_F - E_V$ = 0.0452eV

(4) E_c = Conduction band edge potential, eV

E_F = Fermi energy, eV

k = Boltzmann constant J/ ^oK

T = Absolute Temperature ^oK

The depletion width of the front contact is

$W = 29.5$ Å

in the silicon.
The maximum field ε_m is given by

(5) $\varepsilon_m = \sqrt{\frac{2qN_{D.A}}{\varepsilon_s} (V_R + V_D - \frac{kT}{q})} = 4.38 \cdot 10^6$ V/cm Ref 6

The contact resistance can be calculated from the tunneling conductance

(6) $R_c = G_o^{-1} = \sqrt{\frac{W}{2m^*\phi}} \left(\frac{h^2}{q}\right) \exp \frac{4\pi W}{h} \sqrt{2m^*\phi}$ Ref 8

(7) $= 3.16 \cdot 10^{-11} \frac{W_{\mathring{A}}}{\sqrt{m^*/m}} \exp 1.035 W_{\mathring{A}} \sqrt{m^*/m\phi}$

At very low temperatures ($\hat{\sim}$ 600°C) it is difficult to obtain a sufficient surface concentration of dopant atoms by diffusion and a regrowth layer may be produced from a eutectic alloy of a dopant metal (aluminum) and a semiconductor. If a lower energy gap material (germanium) is chosen the contact potential V is reduced, providing an improved contact. Figure 2 shows an energy level diagram for a copper contact including an aluminum eutectic alloy (Al-Si or Al-Ge) and forming a regrowth layer with N = $5 \cdot 10^{18}$ Al/cm^3.

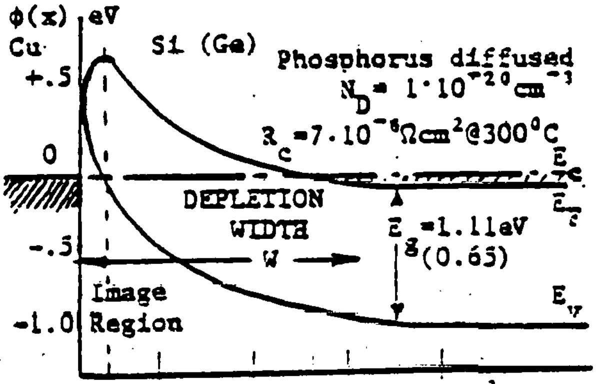

Figure 1. Front Contact

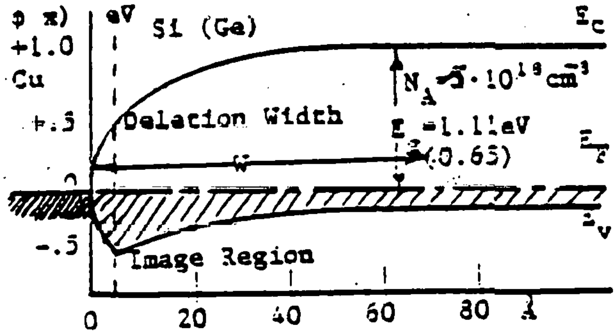

Figure 2. Back Contact

4. FLAT SPOT PHENOMENON

V.G. Weizer et al.[9] have recently published a hypothesis and supporting evidence to explain an IV characteristic anomaly observed on solar cells operated at low temperatures and occasionally at room temperature. The flat spot is a truncation of the maximum power knee of the curve as shown in Figure 3, and is believed[3] to be due to a resistive metal-semiconductor-like junction (MSL) shunting the PN junction. The MSL junction results from the dissolution of silicon by the metalization of the front contact in a low temperature solid state reaction. The authors have shown the phenomenon to be almost independant of the metal system tried for 9 different systems. The silicon surface pitting observed by Weizer et al. is reminiscent of an earlier similar phenomenon observed on germanium surface barrier transistors with indium electrodes[10]. In this case the germanium base dissolved in the indium electrodes, eventually causing device failure. This problem was solved by dimensioning and heat treating the device so that a small germanium-indium alloy region was formed[12] substantially reducing the dissolution rate. Similarly, it can be presumed that a silicon constituent in the solar cell electrodes would suppress the dissolution process.

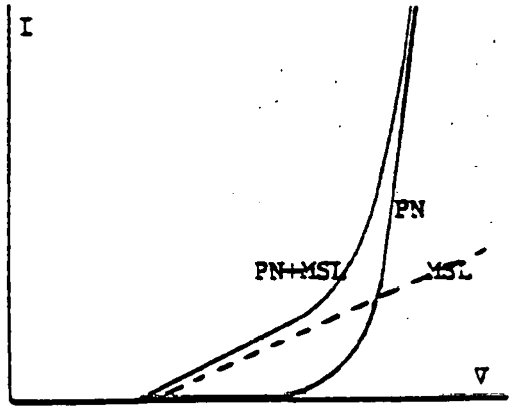

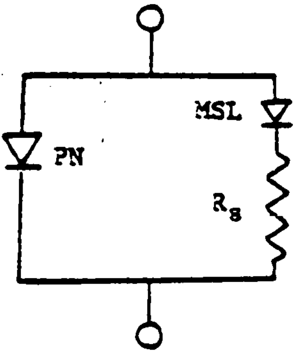

Figure 3. Flat Spot Phenomenon

5. S SHAPED CURVES

During work with screened thick film copper electrodes we have observed S shaped IV curves similar to Figure 4. Such curves were usually seen when contacts were fabricated at relatively low temperatures (near 500°C). the shape of the curve suggested a PN junction of Schottky barrier in series with the current generator of the solar cell. To provide an experimental analog of this situation, a germanium power transistor 2N1136 was connected as shown in the schematic diagram of Figure 5. A normal silicon solar cell was then curve traced by direct connection (curve 1) and through the emitter base diode of the transistor (curve 2). The resulting curve is at least qualitatively similar to Figure 4.

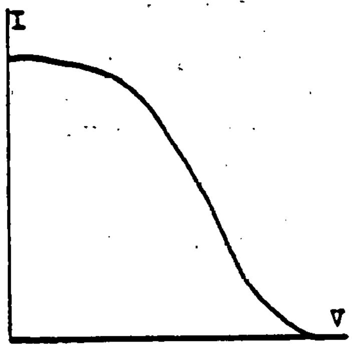

Figure 4. S Shaped Curve

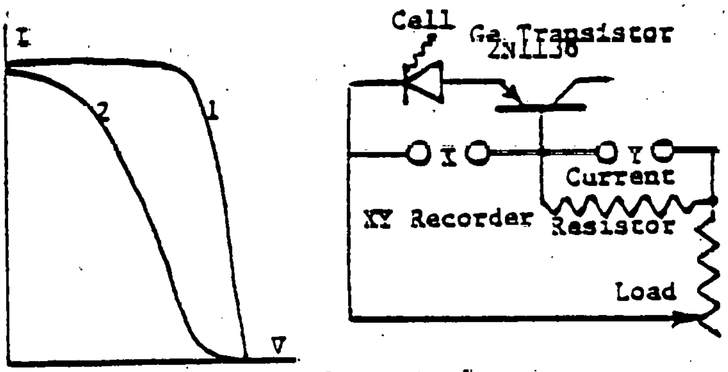

Figure 5. S Shaped Curve Analog

6. PRESENT STATUS OF COPPER THICK FILM CELLS

Figure 6 shows a typical screened copper back contact cell fabricated at 650°C (outer curve) plotted with a typical control cell with titanium-palladium-silver contacts (inside curve). It is apparent that in this system the screened copper contact does not represent an efficiency limitation. Further, the diffusion of copper through the cell has not appeared to either shunt the PN junction or severely degrade the lifetime.

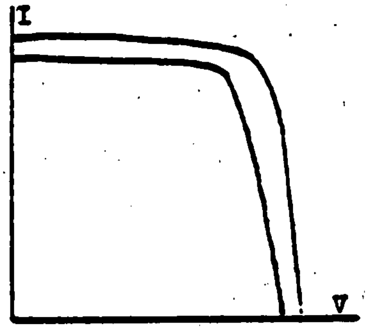

Parameter	Control (Ti-Pd-Ag)	Thick Film Cu Back with Al-Si Eutectic
I_{sc}	84.1 mA	86.6 mA
V_{oc}	572 mV	583 mV
P_{mp}	33.6 mW	37.2 mW
I_{mp}	74.6 mA	77.4 mA
V_{mp}	451 mV	480 mV
η(uncoated)	8.4 %	9.3 %
Cell Area	4 cm^2	4 cm^2
Fill Factor	70 %	74 %
R_s	0.308 Ω	0.220 Ω

Figure 6. IV Curves of Typical Screened Cell and Control

where h = Planck's constant

$(m^*/m)_e$ = 0.1905 the effective electronic mass in the <100> direction

(8) $(m^*/m)_h$ = 0.16 the effective hole mass in the <100> direction

ϕ = $E_g - \phi_B = 0.42$eV

E_g = Energy gap of silicon = 1.11eV

Germanium = 0.65eV

The calculated front contact tunneling resistance is

$$R_o = 1.69 \cdot 10^{-6}\ \Omega\text{cm}^2$$

Since the barrier voltage values vary among workers, and their magnitude affects the argument of the exponent in equation 6 and 7, the calculated contact resistance is subject to wide variation. The energy band relationships for a copper contact on a silicon front surface doped with 1.10^{21} phosphorous atoms are shown in Figure 1.

3. BACK CONTACT

When the semiconductor surface has a higher resistivity, as on the back contact, it is necessary to dope the surface of the semiconductor under the electrode metal. In case of high firing temperatures (~ 800°C) an elemental donor impurity may be included in the metal to diffuse into the semiconductor during the firing step. Since only the surface needs to be doped, the donor atom must become a substitutional impurity in the silicon lattice within a few lattice spaces of the surface. A brief firing period will usually suffice.

7. CONCLUSION

We have presented two cases of severe contact problems seen in solar cells. While this by no means exhausts the catalog of contact maladies, the examples were thought to be of interest. Enegry level diagrams for normal solar cell contacts were also reported.

The author wishes to express his gratitude to Dr. I. Weinberg, NASA Lewis Research Center for permission to reproduce Figure 3.

REFERENCES

1. P. Rappaport, RCA Rev. 20, p.373 (Sept 1959)
2. S. Matlow, US Patent #2, 984, 775 (5-1961)
3. P.A. Iles, Conf. Rec. on IEEE Photovolt. Spec. Conf., p.1 (May 1972)
4. E.L. Ralph, Proc. 11th IEEE Photovolt Spec. Conf., p.315, (1975)
5. B. Ross and D.B. Bickler, Proc. 3rd E.C. Photovolt, Solar Energy Conf. p.674, Cannes, France (Oct. 1980)
6. M.P. Lepselter and J.M. Andrews in "Ohmic Contacts to Semiconductors" Ed.B. Schwartz, Electrochem. Soc p.159, New York (1969)
7. E.H. Rhoderick, "Metal Semiconductor Contacts, Claredon Press, p.59, Oxford (1978)
8. J.G. Simmons, Jour. Appl. Phys. p.34, 1793, (June 1973)
9. V.G. Weizer and J.D. Broder, Proc. 15th IEEE Photovolt. Spec. Conf., p.235, (May 1981)
10. J.W. Tiley and C.G. Thornton, Proc.IRE, 41,1706 (Dec 1953)
11. J. Roschen and C.G. Thornton, Jour.Appl.Phys. 29,923 (June 1958)
12. A.D. Rittmann, G.C. Messenger, R.W.Williams and E.Zimmerman, IRE Trans. on El.Dev 5,49 (Apr 1958)

14.0 REFERENCES

1. B. Ross, Proceedings of the 14th IEEE Photovoltaic Specialists Conference, San Diego, CA p. 787
2. B. Ross, Proceedings of the 14 IEEE Photovoltaic Specialists Conference, San Diego, CA p. 1406
3. B. Ross, Extension Final Report "Production Process and Equipment Development" DOE/JPL 955164 - 79/4 p. 72 (Dec. 1979)
4. B. Ross, Quarterly Report #3 "Development of an All-Metal Thick Film Cost Effective Metalization System for Solar Cells" DOE/JPL 955688 - 80/7, p. 18 (Sept. 1981)
5. Loc cit, Ref. 3, p.10
6. Ibid, p. 72
7. M.P. Lepselter and J.M. Andrews in Ohmic "Contacts to Semiconductors", B. Schwartz, Ed., Electrochem. Soc. p. 159 New York (1969)
8. E.H. Roderick, "Metal Semiconductor Contacts", Clarendon Press, p. 59, Oxford (1978)
9. J.G. Simmons, Jour. Appl. Phys., 34 1793 (Jun 1973)
10. Handbook of Chemistry and Physics, 57th edition, CRC Press, Cleveland, OH, (1976-77)
11. F.T.Wall, "Chemical Thermodynamics", W.H. Freeman, San Francisco, CA, p. 47 et seq. (1958)
12. B. Ross, and D. Mentley Quarterly Report #1 "Development of Economical Improved Thick Film Solar Cell Contacts", DOE/JPL 955-164-78/4 p. 9,10 (Jan. 1979)
13. B.H. Mahan, "Elementary Chemical Thermodynamics", W.A. Benjamin, New York, N.Y., p. 27-36 (1963)
14. N.I. Sax, "Dangerous Properties of Industrial Materials", Van Nostrand-Reinhold, New York, p. 972. (1979)
15. L. Bretherick, "Handbook of Reactive Chemical Hazards", Butterworths, London, p. 197. (1979)
16. A. Stock, "Hydrides of Boron and Silicon", Cornell Univ. Press, Ithica, N.Y., (1933).

17. T. Moeller, "Inorganic Chemistry", John Wiley, New York, (1952)

18. B. Ross, Quarterly Report No. 1 "Development of an All-Metal Thick Film Cost Effective Metalization System for Solar Cells", DOE/JPL 955688-80/4, August 1980

☆U.S. GOVERNMENT PRINTING OFFICE:1984 -746 -081/ 2556 REGION NO. 4